# Electronic and Magnetic properties of Molecular layers on 2D materials

Nianjheng Wu

université
PARIS-SACLAY

# Electronic and Magnetic properties of Molecular layers on 2D materials

*Propriétés électroniques et magnétiques des couches moléculaires sur matériaux 2D*

**Thèse de doctorat de l'université Paris-Saclay**

École doctorale n° 572, Ondes et Matière (EDOM)
Spécialité de doctorat : Physique
Graduate School : Physique
Référent : Faculté des sciences d'Orsay

Thèse préparée à l'**Institut des Sciences Moléculaires d'Orsay** (Université Paris-Saclay, CNRS), sous la direction d'**Andrew J. MAYNE**, Directeur de recherche, et le co-encadrement d'**Hélène BOUCHIAT**, Directrice de recherche

**Thèse soutenue à Paris-Saclay, le 9 décembre 2022, par**

**NianJheng WU**

## Composition du Jury

Membres du jury avec voix délibérative

| | |
|---|---|
| **Odile STEPHAN**<br>Professeure, Université Paris-Saclay | Présidente |
| **Johann CORAUX**<br>Professeur, Université Grenoble Alpes | Rapporteur & Examinateur |
| **Jean-François DAYEN**<br>Maître de conférences (HDR), Université de Strasbourg | Rapporteur & Examinateur |
| **Jérôme LAGOUTE**<br>Directeur de recherche, Université Paris Cité | Examinateur |
| **Philippe LAFARGE**<br>Professeur, Université Paris Cité | Examinateur |

THESE DE DOCTORAT

NNT : 2022UPASP148

université PARIS-SACLAY | ÉCOLE DOCTORALE Ondes et matière (EDOM)

**Titre :** Propriétés électroniques et magnétiques des couches moléculaires sur matériaux 2D

**Mots clés :** Graphène, Spintronique, Molécule magnétique, Magnéto transport, matériaux 2D

**Résumé :** Le graphène est une couche d'atomes de carbone arrangé en un réseau hexagonal (structure en nid d'abeille) en longueur et d'un atome d'épaisseur qui a des propriétés électroniques uniques dues à sa relation de dispersion linéaire. Cependant, aucune manifestation de magnétisme intrinsèque ou d'interaction spin-orbite n'existe dans ce matériau. Ce travail de thèse décrit nos essais pour induire ces interactions spin-orbite ou du magnétisme en couplant le graphène à des dichalcogénures de métaux de transition (TMDs) ou des molécules spécifiques. Dans la première partie nous avons montré la persistance d'un supercourant induit par des contacts supraconducteurs à forts champs magnétiques hors du plan dans des échantillons couplés à des TMD. Nous attribuons la robustesse de ce supercourant à des états de bord quasi-balistiques, stabilisés par la forte interaction spin-orbite induite dans le graphène par le $WS_2$. Dans la seconde partie, on étudie les signatures de transport mésoscopique à travers le graphène sur lequel trois types de molécules différentes ont été greffées pour en déduire le degré de magnétisme induite par ces molécules. Pour le graphène recouvert de molécules de Fe-porphyrins, des expériences de magnétorésistance montrent une croissance importante de la cohérence de phase quand la température est diminuée de 4K à 0.2K. Cette croissance est de l'ordre de la dépendance en $T^{-0.5}$ attendue quand la cohérence de phase est seulement due aux interactions inélastiques entre électrons, nous indiquant donc que le Fe-porphyrin n'amène pas de diffusion renversant le spin aux électrons de conduction du graphène. Cette situation est différente avec les molécules TCNQ déposées sur le graphène. Dans ce cas, une croissance plus petite de la cohérence de phase est observée quand la température diminue ce qui suggère un spin flip scattering venant des moments magnétiques induits. Pour finir, la magnétorésistance à basse température des molécules de $TbPc_2$ greffées sur le graphène montre les fluctuations de conductance universelle (UCF) d'un échantillon cohérent en phase. De façon intéressante, les UCF affichent un bruit dépendant du champ magnétique, qui est le plus élevé à basse température et à champ faible. Un spectre de bruit avec une dépendance en 1/f suggère des systèmes magnétiques à deux niveaux avec une large distribution de temps de relaxation dépendant du champ. Cela indique des moments magnétiques de type Ising, anisotropes et fluctuants, sur le graphène dont la barrière d'énergie caractéristique diminue avec le champ magnétique hors du plan.

université PARIS-SACLAY | ÉCOLE DOCTORALE Ondes et matière (EDOM)

**Title :** Electronic and Magnetic properties of Molecular layers on 2D materials

**Keywords :** Graphene, Spintronic, Magnetic molecule, Magneto transport, 2D materials

**Abstract :** Graphene is single-atom-thick layer of carbon atoms arranged in a honeycomb lattice, which has unique electronic properties caused by a linear energy dispersion. However, graphene display neither intrinsic magnetism nor spin orbit interaction (SOI). This PhD work describes attempting to induce SOI and magnetism by coupling graphene with transition metal dichalcogenides (TMDs) or specific molecules. In the first part, we found the persistence of a supercurrent induced by superconducting contacts even in high out-of-plane magnetic fields in samples coupled to TMD. We attribute this robustness to quasiballistic edge states stabilized by the strong SOIs induced in graphene by $WS_2$. In the second part, we explored signatures of mesoscopic transport through graphene on which three different type molecules were grafted, to deduce the degree of magnetism induced by the molecules. In graphene covered by Fe-porphyrin molecules, magnetoresistance experiments show an important increase of phase coherence when temperature is decreased from 4K to 0.2K. This increase has the order of the $T^{-0.5}$ dependence expected when phase coherence is exclusively limited by inelastic electron-electron interactions, which indicates that Fe-porphyrins do not generate large spin flip scattering on conduction electrons in graphene. The situation is different with TCNQ molecules deposited on graphene. In that case, a smaller increase of phase coherence is observed when temperature is reduced, which may suggests the spin flip scattering from induced magnetic moments. Lastly, the low temperature magnetoresistance of $TbPc_2$ molecules grafted on graphene features universal conductance fluctuations (UCF) of a phase-coherent sample. Interestingly, these UCF display a magnetic field-dependent noise, which is highest at low temperature and low field. A noise spectrum with a 1/f dependence suggests magnetic two-level systems with a wide distribution of field-dependent relaxation times. This points to anisotropic Ising-like fluctuating magnetic moments on graphene whose characteristic energy barrier decreases with out-of-plane magnetic field.

# Synthèse en français

Le graphène est une couche d'atomes de carbone arrangé en un réseau hexagonal (structure en nid d'abeille) en longueur et d'un atome d'épaisseur qui a des propriétés électroniques uniques dues à sa relation de dispersion linéaire. Cependant, aucune manifestation de magnétisme intrinsèque ou d'interaction spin-orbite n'existe dans ce matériau. De nos jours, il est possible de construire des hétérostructures composées de différents matériaux de van der Waals avec des interfaces atomiquement nettes. Le défi technique dans le processus de fabrication est de récupérer les matériaux minces exfoliés ou monocouche après exfoliation mécanique tout en évitant toute dégradation chimique et mécanique. J'ai utilisé les techniques de transfert de film PPC et PC pour fabriquer l'hétérostructure vdw souhaitée. J'ai également développé une exfoliation assistée par l'or pour les monocouches de TMD et plusieurs techniques de transfert à sec pour la fabrication de piles au cours de mon doctorat. Au début de mon doctorat, nous n'utilisions que la technique de transfert à sec du film PPC pour fabriquer l'hétérostructure dans notre groupe, qui fonctionne pour l'hétérostructure du graphène et du hBN, mais pas pour les autres TMD. Au cours de ces années, j'ai trouvé le bon état de la méthode de transfert à sec du film PC pour réaliser différentes hétérostructures. Étant donné que les TMD développés par CVD ou les TMD exfoliés ont une forte adhérence avec le substrat, la technique de transfert à sec du film PPC ne peut pas capter directement la monocouche, mais le film PC est capable de libérer les TMD monocouche du substrat. De plus, j'ai testé la méthode d'exfoliation assistée par couche d'or afin que nous soyons maintenant en mesure de fabriquer de nombreux types de TMD de grandes tailles (> 100 um) dans notre laboratoire, tels que $WS_2$, $WSe_2$, $MoS_2$, $MoTe_2$, $WTe_2$, etc. Au cours de la dernière année, j'ai appris la méthode de transfert à sec à basse température avec un film PCL qui peut être utilisé dans certains matériaux sensibles à la température. Dans mon doctorat. carrière, j'ai aidé de nombreux doctorants. étudiants, post-doctorants et chercheurs pour fabriquer l'hétérostructure et les dispositifs souhaités par toutes ces méthodes. Bien sûr, j'ai aussi développé quelques projets parallèles à travers ces méthodes. Ce travail de thèse décrit nos essais pour induire ces interactions spin-orbite ou du magnétisme en couplant le graphène à des dichalcogénures de métaux de transition (TMDs) ou des molécules spécifiques. Dans la première partie nous avons montré la persistance d'un supercourant induit par des contacts supraconducteurs à forts champs magnétiques hors du plan dans des échantillons couplés à des TMD. Nous attribuons la robustesse de ce supercourant à des états de bord quasi-balistiques, stabilisés par la forte interaction spin-orbite induite dans le graphène par le $WS_2$. Dans la seconde partie, on étudie les signatures de transport mésoscopique à travers le graphène sur lequel trois types de molécules différentes ont été greffées pour en déduire le degré de magnétisme induite par ces molécules. Pour le graphène recouvert de molécules de Fe-porphyrins, des expériences de magnétorésistance montrent une croissance importante de la cohérence de phase quand la température est diminuée de 4K à 0.2K. Cette croissance

est de l'ordre de la dépendance en $T^{-0.5}$ attendue quand la cohérence de phase est seulement due aux interactions inélastiques entre électrons, nous indiquant donc que le Fe-porphyrin n'amène pas de diffusion renversant le spin aux électrons de conduction du graphène. Cette situation est différente avec les molécules TCNQ déposées sur le graphène. Dans ce cas, une croissance plus petite de la cohérence de phase est observée quand la température diminue ce qui suggère un spin flip scattering venant des moments magnétiques induits. Pour finir, la magnétorésistance à basse température des molécules de $TbPc_2$ greffées sur le graphène montre les fluctuations de conductance universelle (UCF) d'un échantillon cohérent en phase. De façon intéressante, les UCF affichent un bruit dépendant du champ magnétique, qui est le plus élevé à basse température et à champ faible. Un spectre de bruit avec une dépendance en 1/f suggère des systèmes magnétiques à deux niveaux avec une large distribution de temps de relaxation dépendant du champ. Cela indique des moments magnétiques de type Ising, anisotropes et fluctuants, sur le graphène dont la barrière d'énergie caractéristique diminue avec le champ magnétique hors du plan.

# Acknowledgements

First of all, my deepest gratitude goes to my supervisors, Andrew J Mayne and Hélène Bouchiat, for choosing me to work on this interesting collaboration project. During these years, they supported me greatly in scientific work and daily life. They never discouraged me from participating in other research projects or developing some techniques irrelevant to my main projects. Therefore, I could experience such an amazing journey and had a lot of fun from daily work. Their doors are always opened for me when I have trouble with experiments, scientific discussions, and daily life. As a foreigner pursuing a Ph.D. in France, their support meant a lot to me and made me feel I was not alone there. Also, I am completely amazed by Hélène's passion for physics and her profound knowledge as a physicist. Normally, when we see special signals from experiments, she can always tell a good method or reasonable explanation to explore these interesting findings. Of course, I'd also be deeply thankful to my unofficially third supervisor, Sophie Guéron. Although I used to ask some fundamental questions, she always patiently explained to me clearly and concisely. When I struggled with sample fabrication, she was very kind to provide direction or suggestions. I have learned numerous valuable things from the discussions and work with three of my supervisors, and they show me what a good researcher should be like, and the way to develop a rigorous attitude in research. It is my honor to have them to be my supervisors.

I want to thank the former MESO group member, Taro Wakamura. He was my tutor when I was a fresh Ph.D. student. He taught me how to fabricate 2D materials and heterostructures with all the necessary skills in sample fabrication. He inspired me to investigate more dry transfer techniques so that we can fabricate many different kinds of 2D materials and heterostructures in the lab now. I also want to thank all the members of the MESO group, especially Richard, for his effective and optimized solutions to all kinds of problems. His serious attitude in research and work shows us a model to follow. Of course, the other group members are all willing to help me when I have problems. I'm very grateful to all the members in the MESO group. I will always miss the time we shared during lunchtime, coffee break, experimental room and on the train. These countless moments will never disappear.

Third, I'd like to deeply thank Jérome and Cyril. They were very kindly helping me to do MBE several times in their lab, even though they also had an intense experimental schedule.

I still remembered the moment that we chatted in the courtyard of their lab while drinking a hot coffee on a rainy and cold morning. It's a great pleasure to work with Jérome and Cyril. Also, many thanks to my molecule source, Stephane from CEA. He synthesized a lot of $TbPc_2$ for me. Therefore, I can have failed several times in making a mixture of $TbPc_2$ solution until I get the best condition. During the past years, I also got a lot of help from Rebeca in C2N. We discussed and exchanged our methods in the fabrication of 2D materials and dry transfer techniques. I improved the dry transfer methods and learned a lot from her. Thanks for her suggestions and help during these years. Mr. Raphaël in LPS also gave me a lot of help during my Ph.D. career; I used to bother him with equipment problems, even during the weekend. I'd like to express my gratitude to him for all the helps in the clean room. I joined and collaborated with researchers from other groups, like the STEM group, NS2 group, and IDMAG group. I had a great time working and discussing with them. Of course, I'd like to thank all my Ph.D. and postdoc friends in LPS and ISMO. It's a great pleasure to chat with them during serious work and have parties after work or on the weekend.
Finally, I'd like to thank my mother and my family, having a video phone call with them is important spiritual support to me once a week. Without their support, I wouldn't give up the precious time to get along with family and friends. Instead, pursue a Ph.D. degree abroad. In the end, this thesis work is dedicated to my dad and grandpa in heaven, who showed me how to be a responsible person for the family, and they never stopped encouraging me to venture beyond the limit.

# Table of contents

# Chapter 1

# Introduction

The natural two-dimensional material graphene has drawn much attention since its discovery in 2004. Currently, graphene is one of the most intensively studied materials. This one-atom-thick sheet of a continuous network of carbon atoms with a honeycomb pattern is thin, strong, and has high stiffness, as well as being an excellent heat and electrical conductor, which makes graphene to be considered a good candidate for many applications. Since the first experimental evidence of the electronic properties of graphene in 2004 [1], the developed methods (exfoliation, CVD) of graphene preparation have helped the observation of many interesting properties of graphene, such as the quantum Hall effect [2, 3], tunable carrier density and extremely high carrier mobility, etc. Graphene also exhibits other excellent electronic, mechanical, optical, and transport properties. Due to these special and superior properties, graphene has been used widely in many potential applications in capacitors, spintronic devices, fuel cells, conductive films, high-frequency devices, and flexible electronics [4–7].

Although there are many potential applications, graphene displays neither intrinsic magnetism nor a spin-orbit interaction (SOI). Therefore, there has been a great increase in the research on graphene's functionalization, including decorating graphene with many different methods. For example, graphene coupled with organic molecules Tetracyanoquinodimethane(TCNQ) has been proven capable of inducing magnetic moment on graphene [8], or a promising hybrid system to realize the spintronics applications by the intercalate of metallic film between graphene and substrate [9]. The graphene/transition metal dichalcogenides (TMDs) heterostructure is also an achievable method to generate a novel property in graphene [10, 11]. Thanks to the development of dry transfer techniques [12–14], it is now feasible to fabricate the desired heterostructure of graphene coupled with TMDs and the decoration of graphene through molecule beam epitaxy or drop-casting techniques. This

Ph.D. work describes attempting to induce SOI and magnetism by coupling graphene with transition metal dichalcogenides (TMDs) or specific organic molecules.

**Outline of the thesis**

This thesis is written in 6 chapters. In the introduction, Chapter 1, we show only the main results from each work. The further experimental details are described in Chapters 4, 5, and 6. Chapter 2 explains the important theoretical concepts and physics in the thesis. Chapter 3 is related to the methods and techniques for fabricating 2D materials, TMDs, and heterostructure. Chapter 4 presents our work on spin-orbit interaction (SOI) enhanced robustness of supercurrent in Graphene/$WS_2$ Josephson Junctions. For Chapters 5 and 6, we explored signatures of mesoscopic transport through graphene on which three different types of molecules were grafted to deduce the degree of magnetism induced by the molecules. Last, in the Appendix, we address the $TbPc_2$ molecules preparation process, and the phase coherence of $TbPc_2$ grafted graphene using the same method as in chapter 5.

## 1.1 SOI Enhanced Robustness of Supercurrent in Graphene/ $WS_2$ Josephson Junctions

In this work, we demonstrate that SOIs can enhance the superconducting proximity effect in high out-of-plane magnetic fields in graphene-on-tungsten disulfide-based Josephson junctions. These junctions consist of graphene encapsulated between hexagonal boron nitride (hBN) and tungsten disulfide ($WS_2$), which induces strong SOIs in graphene via the proximity effect[15, 10, 11, 16, 17]. The structure of the samples is shown in Figure 1.1.1. These junctions are in the diffusive limit. The junction lengths (L) range between 100 and 500nm from the short- to long-junction regimes. Although the junctions are diffusive, surprisingly, we find clear signatures of induced superconductivity with manifestations of a supercurrent even in magnetic fields in the Tesla range for the graphene-on-$WS_2$ junctions. By contrast, this behavior is not observed for graphene-on-hBN junctions outside the short ballistic regime, i.e., for lengths greater than L=200nm. We argue that this robustly induced superconductivity arises from quasi-ballistic trajectories along the sample edges, stabilized by strong SOIs induced in graphene by $WS_2$.

**Characterization in high field**

To investigate the induced superconductivity at high fields, we increased B around 1T (10000G) and similarly measured dV/dI as a function of Idc and B. Figure 1.1.2 compares

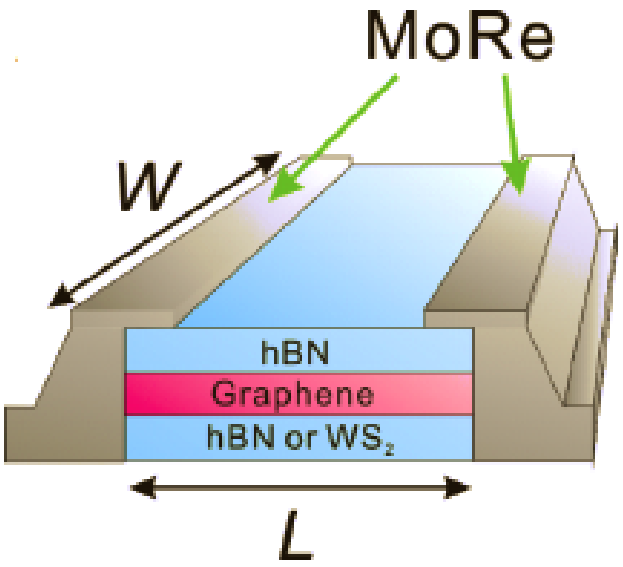


Fig. 1.1.1 Device structure and transport properties around zero magnetic field. Schematic illustration of a graphene-based Josephson junction device of length L and width employed in this study.

Gr/$WS_2$ and Gr/hBN junctions with different L (L = 100, 300, and 500nm). Interestingly, for the shortest, L = 100nm, junctions, a relatively large 100nA wide dip of dV/dI is observed in certain fields, even around 8000G for both Gr/$WS_2$ and Gr/hBN junctions, and oscillates as a function of B. Whereas the field dependence is similar for both types of 100-nm-long junctions, we find a stark difference for the longer junctions, L = 300 and 500nm. While superconducting pockets persist around B = 10000G for Gr/$WS_2$, they are clearly suppressed for Gr/hBN in the Figure 1.1.2 (e)(f).

Beyond these dV/dI maps as a function of Idc and B in limited field regions, a broader picture can be obtained by following dV/dI at zero dc current bias (ZBR) over a wide range of B. ZBR oscillates between the normal state resistance when no superconductivity is induced and has a minimal dV/dI in the middle of the superconducting pocket when the superconducting proximity effect is strongest. Figure 1.1.3 shows the ZBR as a function of B for all junctions. For L=100nm, the ZBR oscillates with a large amplitude both for Gr/$WS_2$ and Gr/hBN, even near B=18000G. On the contrary, for L = 300nm, oscillations are strongly suppressed, especially for B > 5000G for Gr/hBN, while they persist for Gr/$WS_2$ even at higher fields. The difference is even more striking for the L = 500nm junctions. The oscillation amplitudes are considerably different already at a small field, and large oscillations

are visible at B = 18000G for Gr/$WS_2$, while Gr/hBN exhibits almost no oscillations over the entire B range.

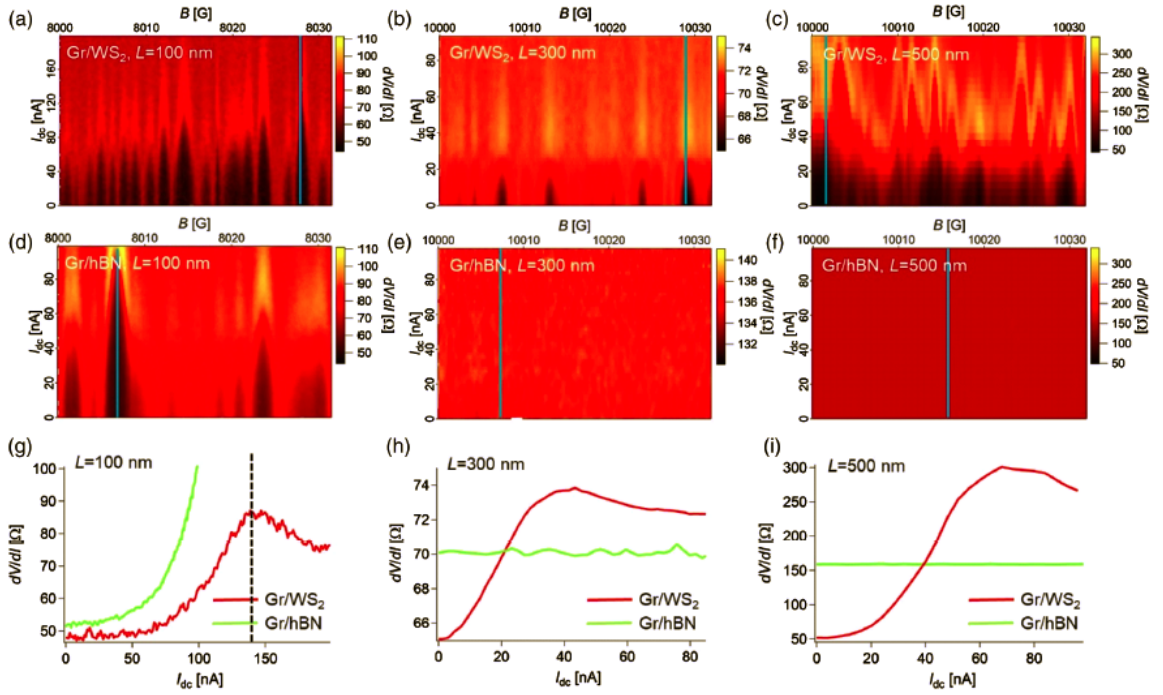


Fig. 1.1.2 Color-coded dV/dI as a function Idc and B around B = 10000G at $V_g$ = 60V for all samples. For L = 100nm [(a),(d)], superconducting pockets are clearly visible, in the form of field regions of low dV/dI at low Idc, for both the Gr/$WS_2$ and Gr/hBN junctions around B = 8000G. For L = 300nm [(b),(e)] and L = 500nm [(c),(f)], superconducting pockets are visible only for the Gr/$WS_2$ junction. (g)–(i) Cross-sectional image along the light blue line shown in (a)–(f) of dV=dI as a function of Idc forGr/$WS_2$ and Gr/hBN junctions with different L. Red and light green curves are from Gr/$WS_2$ and Gr/hBN junctions, respectively. The suppressed dV/dI at low Idc, signature of an induced superconducting proximity effect, is clearly visible for the Gr/$WS_2$ junctions of every length but only for the shortest Gr/hBN junction. In (g), the peak (or bump) of dV/dI for Gr/hBN is located out of the range of Idc in the measurement, and in (h) [(i)], the dV/dI for Gr/hBN (Gr/$WS_2$) is vertically shifted to compare to that for Gr/$WS_2$ (Gr/hBN). The residual resistance around 50 at Idc = 0 for (a)–(i) arises from the measurement wires. The dashed line in (g) represents the value of Idc, which defines Ic.

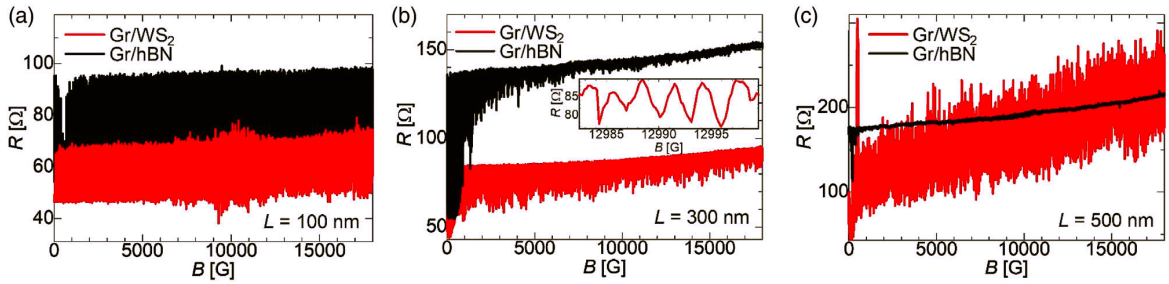


Fig. 1.1.3 Monitoring the superconducting proximity effect over a wide field range, via the zero bias differential resistance variations with B, for the three junction lengths and both Gr/$WS_2$ and Gr/hBN systems, at $V_g$ = 60V. (a) For L = 100nm, both Gr/$WS_2$ and Gr/hBN junctions display comparable oscillation amplitudes up to B $\sim$ 20000G. (b) For L = 300nm, whereas the Gr/hBN junction displays larger amplitude oscillations near B=0, they are rapidly suppressed as B increases. By contrast, the Gr/$WS_2$ junction displays a relatively large amplitude of resistance oscillations that persists even around 20000G. (c) The difference between Gr/$WS_2$ and Gr/hBN is the most striking for L = 500nm junctions. The relative oscillation amplitude of the Gr/$WS_2$ junction's differential resistance is around 50 times greater than that of the Gr/hBN junction over the entire field range. The inset in (b) displays a magnified view of the oscillations for Gr/$WS_2$ around B = 13000G.

## 1.2 The FeTPP and TCNQ molecualr layer deposited on graphene

### Target Molecules

Recently, the utilization of magnetic molecular junctions as spin transport channels is a novel research field for molecular spintronics [18, 19]. A lot of experimental and theoretical research results proposed that organic materials provide great performance in spintronic devices [20, 21]. One of the potential candidates among the organic materials is magnetic porphyrin, such as iron-porphyrin (FeTPP) or platinum-porphyrin (PtTPP). The metal complexes of porphyrins offer a wide range of valuable properties, such as conjugated bond structure, well-ordered geometry, and chemical stability [22]. The relatively high spin filtering behavior has been proven in previous theoretical studies in $FeN_4$ complexes grafted to graphene nanoribbons or carbon nanotubes [23, 24]. The FeTPP was also used in gas sensing devices due to the controllable electronic current by changing the chemical composition of molecular junctions [25].

For the TCNQ/Graphene/Ru(0001) system, a study found that the molecules adsorbed on the lower parts of the ripples are charged, but those adsorbed on the upper part of the ripples are not [26]. In addition, the TCNQ molecules are not magnetic when adsorbed on the lightly p-doped graphene/Ir(111) substrate. The charge transfer process from gr/Ru(0001) substrate has been proven important to form the intermolecular bands in order to achieve long-range magnetic order in these purely organic 2D materials [26]. In a nutshell, TCNQ/Graphene/Ru(0001) system is proven to induce magnetic moments and develop long-range magnetic order on TCNQ molecular layer. Here, we're interested in whether the TCNQ also induces magnetic moments on gated graphene.

### Scheme of devices

The structure of the device is in Figure 1.2.1 (a). We measured the gate dependence for all samples at room temperature before and after the deposition of the molecules. In Figure 1.2.1 (b), the Dirac point is close to gate voltage 7V (black curve) before the deposition of FeTPP molecular layers, and it shifted 4V to 5V gate voltage after the deposition. This implies that charge transfer occurs between graphene and FeTPP, and molecules are the electron donors for graphene. Based on the previous study of Platinum porphyrins [27], we knew porphyrins could behave both as electron donors or acceptors, depending on the initial

doping degree of the graphene sheet. Independently of this initial doping, the Dirac point of graphene is brought towards zero gate voltage: graphene has become neutral. The gate dependence measured in FeTPP grafted graphene at room temperature is similar to what was observed in the case of Pt porphyrins [27].

The TCNQ grafted graphene sample also shows a charge transfer from graphene to TCNQ and reveals that the TCNQ molecules are electron acceptors. before the TCNQ deposition, the Dirac point is located near 4V in gate dependence measurement, which means the graphene is naturally p-type doped. After the deposition of TCNQ layers on graphene, the Dirac point of the graphene has shifted further to the righ (+9V).. See in 1.2.1 (c) red curve. Contrary to FeTPP molecules, TCNQ is the electron acceptor to graphene, and graphene gains more holes as the majority after TCNQ deposition. From the study in scanning tunneling microscopy (STM) [8], TCNQ deposited on the epitaxy-grown graphene indicates TCNQ is the strong electron acceptor. The gate dependence measurement is the other evidence to confirm that the TCNQ molecules are electron acceptors from graphene.

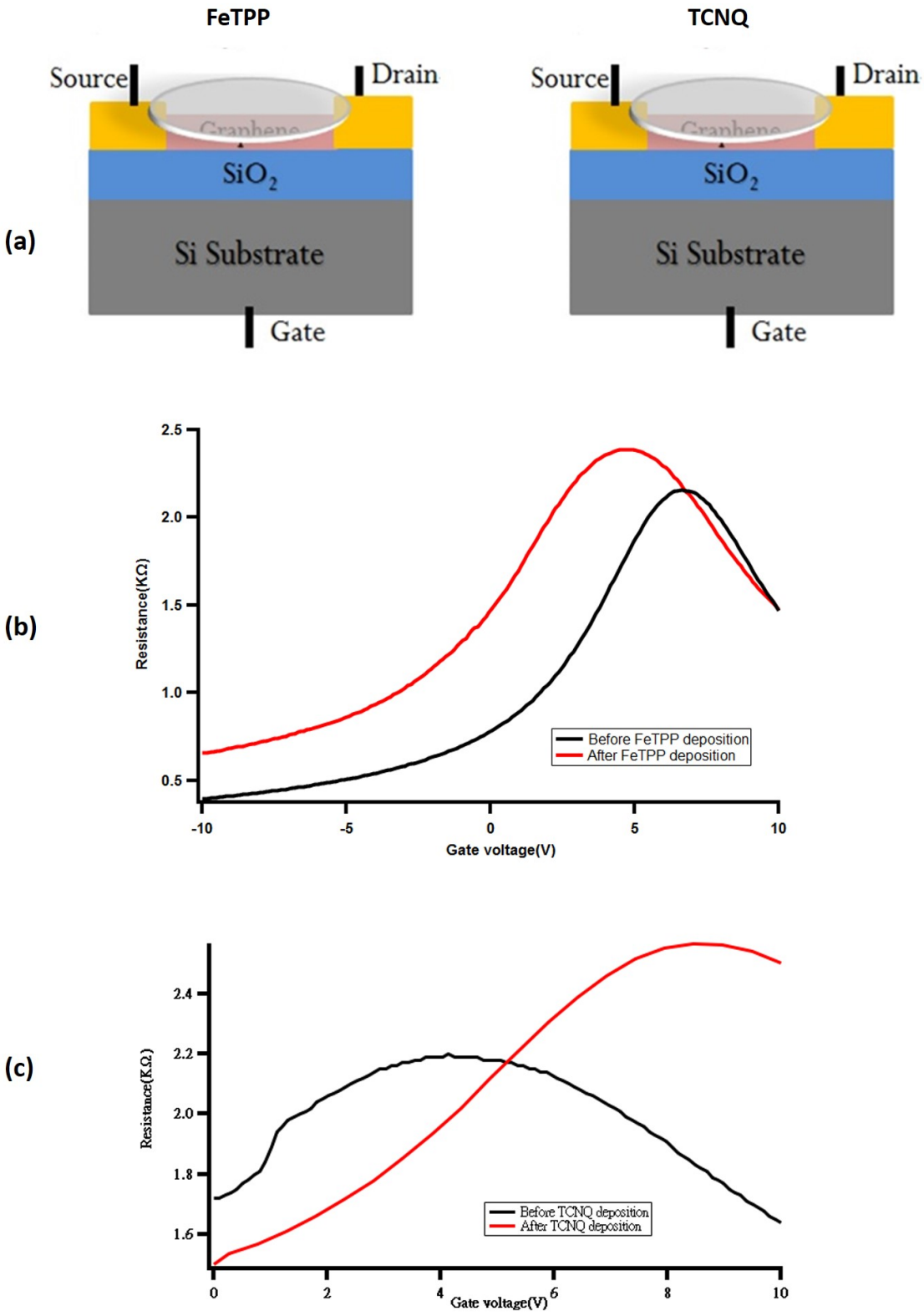


Fig. 1.2.1 (a) Scheme of FeTPP and TCNQ molecular layers grafted on graphene samples by molecular beam epitaxy. (b) Gate dependence at room Temperature before (black curve) and after (red curve) deposition of 1 to 2 layers FeTPP molecule. After the deposition, the charge transfer occurs, and the FeTPP layer is an electron donor to graphene. (c) Same measurement as FeTPP. After the deposition, it also shows the charge transfer, and the TCNQ layer is an electron acceptor to graphene.

**Phase coherence from Magneto-conductance data**

In the applied out-of-plane field, the FeTPP grafted on the graphene sample has a back gate leaking problem. Thus we cannot apply gate voltage on this sample. Figure 1.2.2 (a) is the gate dependence before the leaking problem occurred, just to point out the 0V gate voltage in the hole doping area, still far from the Dirac point. In Figure 1.2.2 (b), the weak localization is clearly seen in 200mK, but it is suppressed when we increase the temperature to 4K. When we increase temperature, the dephasing time $\tau_\phi$ is deceased, which leads to the suppression of weak localization. Meanwhile, the phase coherence length is also decreased when we heat up the temperature. The graphene coated with FeTPP magnetoconductance experiments shows a significant increase in the phase coherence length determined from the analysis of weak localization expected when phase coherence is exclusively limited by inelastic electron-electron interactions, which indicates that FeTPP is not generating an important spin-flip scattering on conduction electrons in graphene. This absence of magnetic scattering is confirmed by the presence of conductance fluctuations of the order of 0.7 $e^2$/h at 200mK.

In the TCNQ sample, we can also compare the weak localization and phase coherence in electron and hole doping regions by applied gate voltage 30V, in which the result shows the weak localization at 200mK is suppressed and the phase coherence length $L_\phi$ just slightly increased when we increase the temperature. The result suggests the induced magnetic moments destroy and suppress the weak localization in the low field. Compared with the applied 30V gate voltage, the weak localization at -30V gate voltage is clearer, and the phase coherence length at 200mK is two times larger than the higher temperature at 4K. The effect of induced magnetic impurity is gate dependent and looks stronger in applied positive gate voltage. This result may indicate the presence of magnetic scattering, which also affects the amplitude of conductance fluctuations.

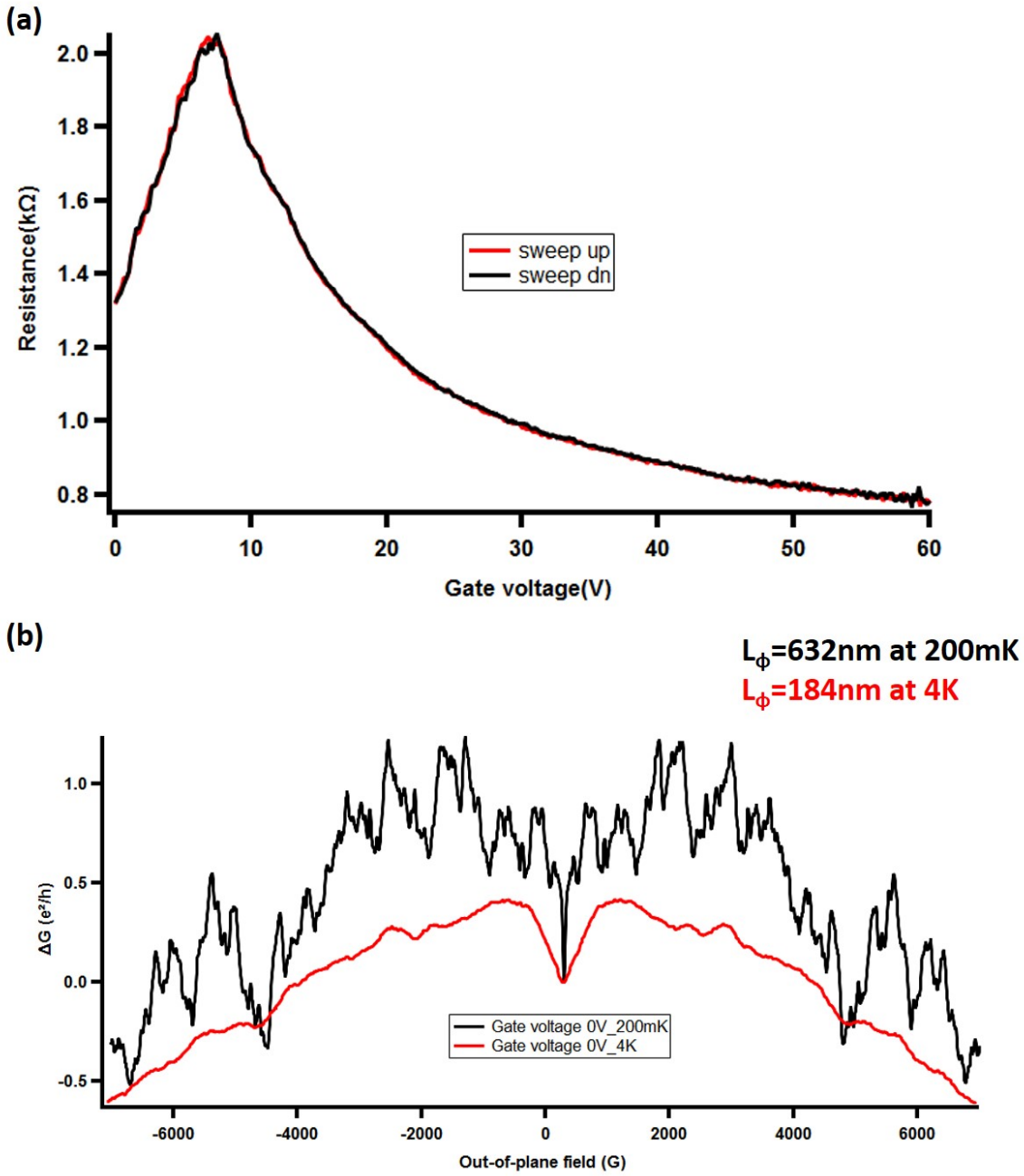


Fig. 1.2.2 (a) Gate dependence of FeTPP molecular layers grafted on graphene sample before the back gate leaking problem occurred. (b) Magneto-conductance result between $\pm$7000G out-of-plane field at 0V gate voltage at 200mK and 4K. In the weak coupling sample (FeTPP/Graphene), the weak localization is clearly suppressed at 200mK, and the phase coherence length $L_\phi$ is decreased with temperature increasing.

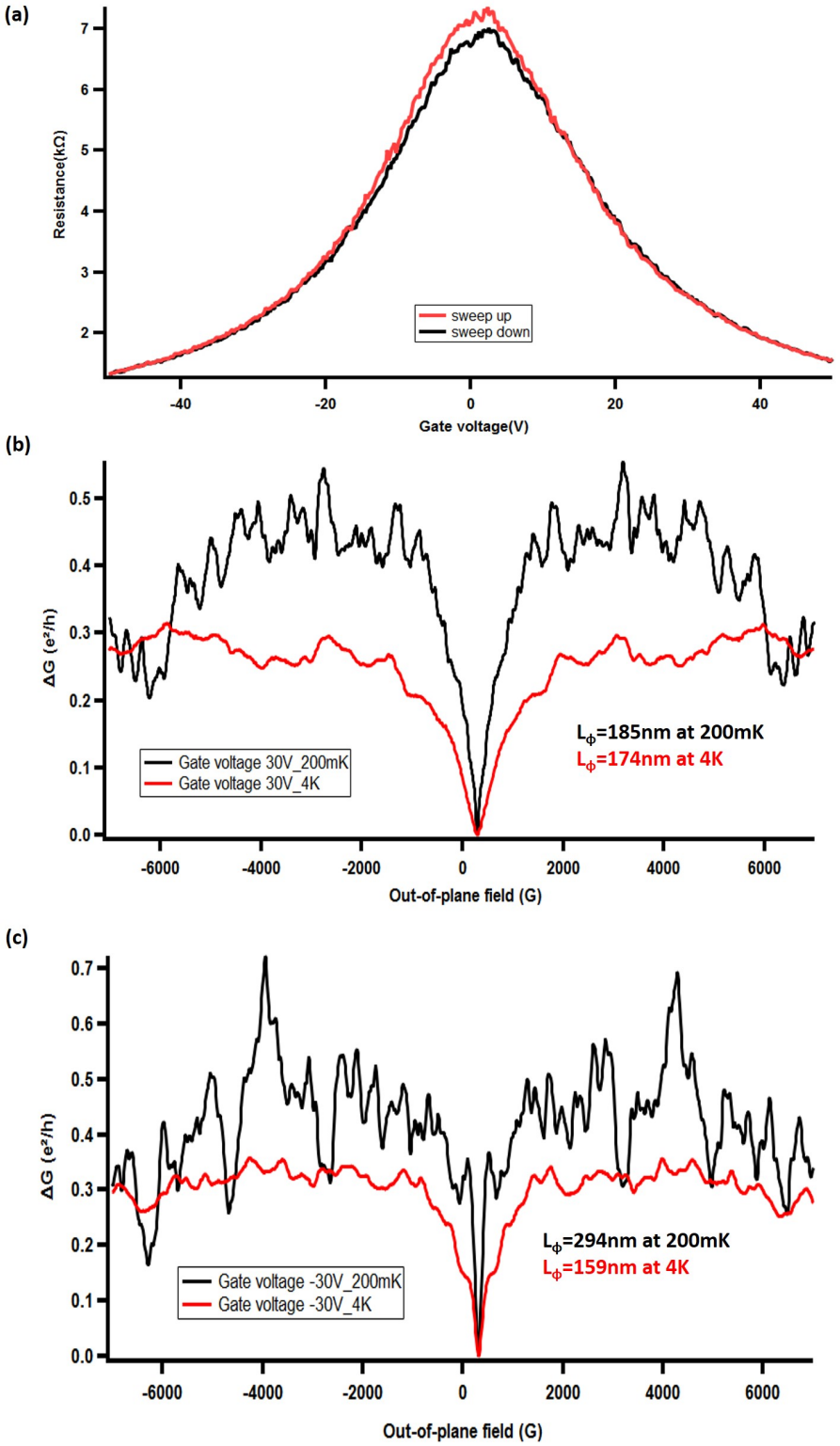


Fig. 1.2.3 (a) Gate dependence of TCNQ molecular layers grafted on graphene sample, the Dirac point is close to zero. (b) Magneto-conductance results in $\pm$7000G out-of-plane field at Dirac point 30V gate voltage at 200mK and 4K. The weak localization is clearly suppressed due to the induced magnetic moment on graphene by TCNQ molecular layer. The phase coherence length $L_\phi$ is decreased with temperature increasing from 200mK to 4K. (c) Same measurement at gate voltage -30V. The weak localization is clearly suppressed due to the induced magnetic moment on graphene by TCNQ molecular layer. The phase coherence length $L_\phi$ is decreased with temperature increasing from 200mK to 4K.

## 1.3 Single-molecule magnet $TbPC_2$ grafted on graphene

The lanthanide single-molecule magnet (SMM) bis-phthalocyanine terbium(III) ($TbPc_2$) has been studied in the graphene nanoconstriction [28] and carbon nanotube [29] as a spin valve device. These devices showed strongly anisotropic hysteresis loops of the magneto-conductance when the easy axis of molecules is aligned along with the applying magnetic field. Anisotropic magnetoconductance signals have been found in other $TbPc_2$ molecular spin valve devices. [30, 31]. The sign and magnitude exchange interaction between terbium ion and delocalized conduction electrons over the phthalocyanine ligands of the molecule has been proven and probed in spintronic configuration [32].

Here, we prepare two different kinds of samples for measurement. The first sample is a pure graphene sample, and the second sample is replaced on a monolayer $WS_2$ flake as a substrate for the graphene ($WS_2$/Graphene) in order to induce strong SOI on graphene for comparison. On each sample, we deposited Ti/Au (5/100nm) metal as contacts on graphene sheets and patterned the device with the several desired two wires geometry. Then, we deposited $TbPc_2$ SMMs on the prepared graphene samples by drop-casting.

In Figure 1.3.1 (a), the Dirac point of the Graphene/TbPc2 sample is clearly located near 8V in gate dependence of resistance measurement, which means the graphene is naturally p-type doped before grated /$TbPc_2$ in the ambient environment. At the Dirac point, the majority of graphene can be turned to be electrons or holes, which means the majority of the carrier are electrons on the right side of the Dirac point, and the majority of carriers are holes on the left side of the Dirac point. After grafting graphene with $TbPc_2$ by drop casting, the Dirac point of the gate dependence of resistance has shifted further to the right, as seen in Figure 1.3.1 (b). This result shows that $TbPc_2$ is a strong electron acceptor for graphene, and graphene gains more holes as the majority after grafting. Second, the clear hysteresis in Figure 1.3.1 (b) shows up after $TbPc_2$ deposition at room temperature. This result can probably be related to the slow relaxation of the hopping processes between neighboring molecules [33, 34].

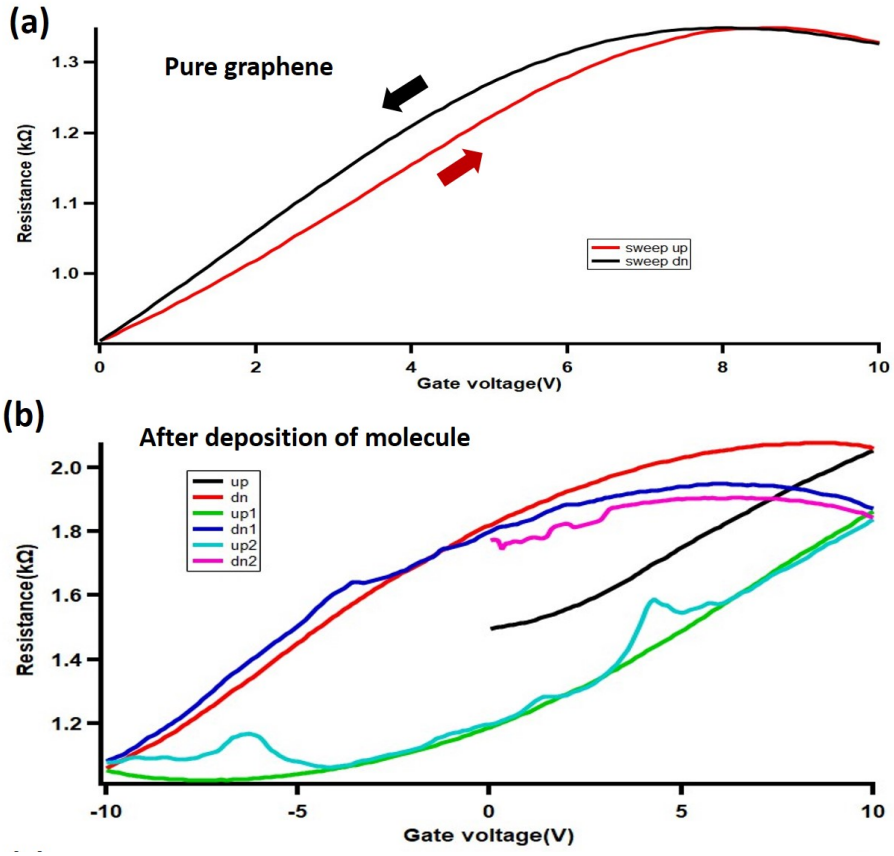


Fig. 1.3.1 Gate dependence measurement, applying the back-gate voltage between $\pm$10V. The gate dependence in Grapehene/$TbPc_2$ and $WS_2$/Grapehene/$TbPc_2$ samples have a similar behavior before and after the drop-casting of molecular layers. Here, we use Grapehene/$TbPc_2$ sample as an example to illustrate the effect after the deposition of $TbPc_2$ molecules. (a) Before $TbPc_2$ molecules drop-casting. (b) After $TbPc_2$ molecules drop casting at room temperature, the back-gate voltage is swept forward/backward several times, and the result shows hysteresis due to the charge transfer process between graphene and $TbPc_2$.

**Magnetoresistance in out-of-plane field**

Both samples were measured at the same time between $\pm$3000 Gauss(G) at 12mK at applying gate voltage 20V, the magneto-resistance in the out-of-plane field for both samples exhibit irreproducible magneto-resistance in forward sweep and backward sweep because the $TbPc_2$ induced magnetic moments on graphene that changed the interferences between the coherent trajectories across the samples, as seen in the Figure 1.3.2. And also, all curves are asymmetric functions of a magnetic field, as expected in the two probes' measurements in the presence of the time-reversal symmetry breaking due to the induced magnetic moment on graphene [27]. The most intriguing feature is that the higher degree of noise shows up when the applied field is close to zero for both samples. We related this higher degree of noise close to the zero field due to the spin-flip of long spin relaxation time with events at the time scale of the experiment. There are due to $TbPc_2$-induced magnetic moment on graphene. However, we find that the excess noise observed at the low field is absent at 3000G.

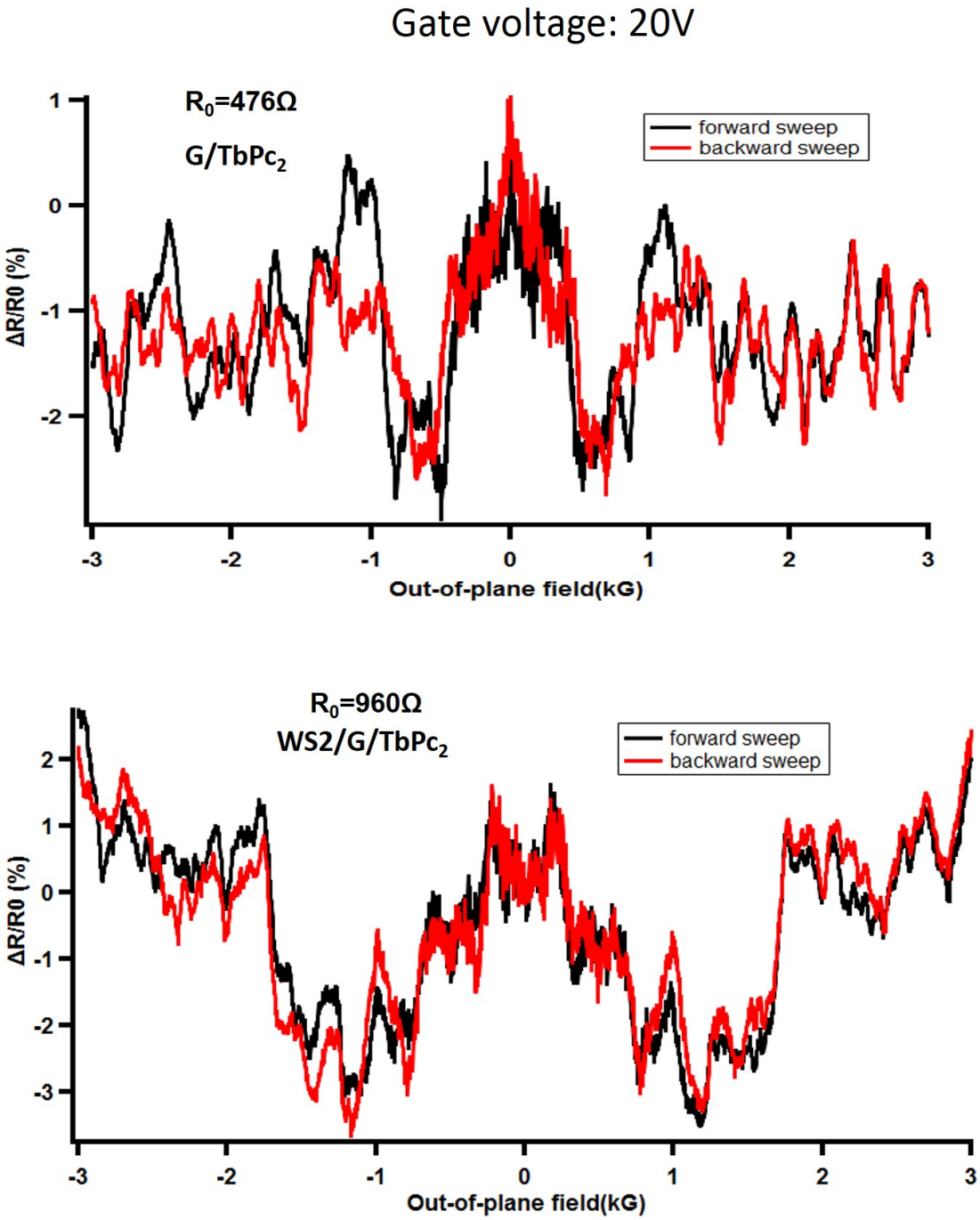


Fig. 1.3.2 Graphene/$TbPc_2$ and $WS_2$/Graphene/$TbPc_2$ samples in out-of-plane field between $\pm$3000G with applying a 20V gate voltage at 12mK. A higher degree of noise shows up when the applied field is close to zero in both samples.

### Low frequency 1/f noise

The magneto-resistance results display a magnetic field-dependent noise, which is highest at low temperatures and low fields. In order to quantize the magnitude of noise, we acquire the output signal fluctuations from Lock-In Amplifiers in time and compute the noise spectrum by Fourier transform [35]. A noise spectrum with a 1/f dependence suggests the existence of a broad distribution of two-level systems with a wide distribution of field-dependent relaxation times, as seen in Figure 1.3.3. In $TbPc_2$ grafting graphene sample, the two-level system represents the spin-flip state in $TbPc_2$ induced magnetic moment on graphene.

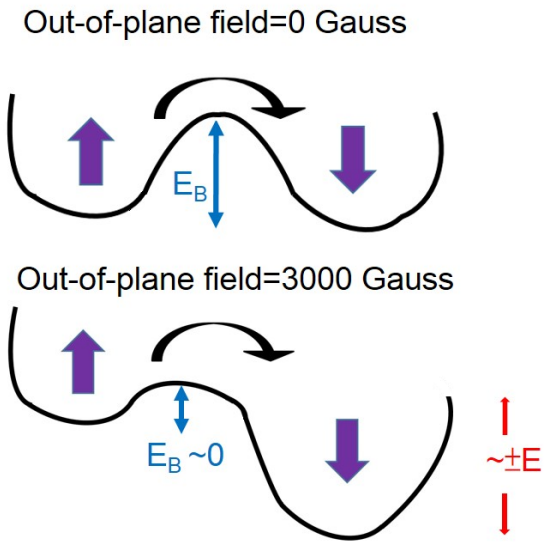


Fig. 1.3.3 Magnetic two-level system at zero fields and 3000 Gauss. $E_B$ is the anisotropy magnetic barrier energy, and the barrier decreases with an applied magnetic field.

We measured the noise spectrum in both samples at the applied 55V gate voltage, which is the Dirac point for the sample $WS_2$/Graphene/$TbPc_2$. This sample exhibits the largest resistance variance of fluctuation, as shown in Figure 6.3.6 (b). In the beginning, we performed the 1/f fitting of the experimental results of the noise spectral density at different temperatures from 10 mK to 300 mK; see Figure 1.3.4 (a) and (b). First and foremost, almost all data can be fitted with a 1/f curve. We attribute this 1/f noise to the presence of a large distribution of magnetic molecular clusters behaving as a two-level system with a magnetic anisotropy barrier due to the anisotropy field aligning with the molecular Tb spin perpendicular to the graphene layer. However, when the temperature reaches 300mK in the Graphene/$TbPc_2$ sample, the noise spectral density starts to deviate from the 1/f behavior. Besides, the noise magnitude increases at low temperatures, which is due to the increase of universal conductance fluctuations at low temperatures.

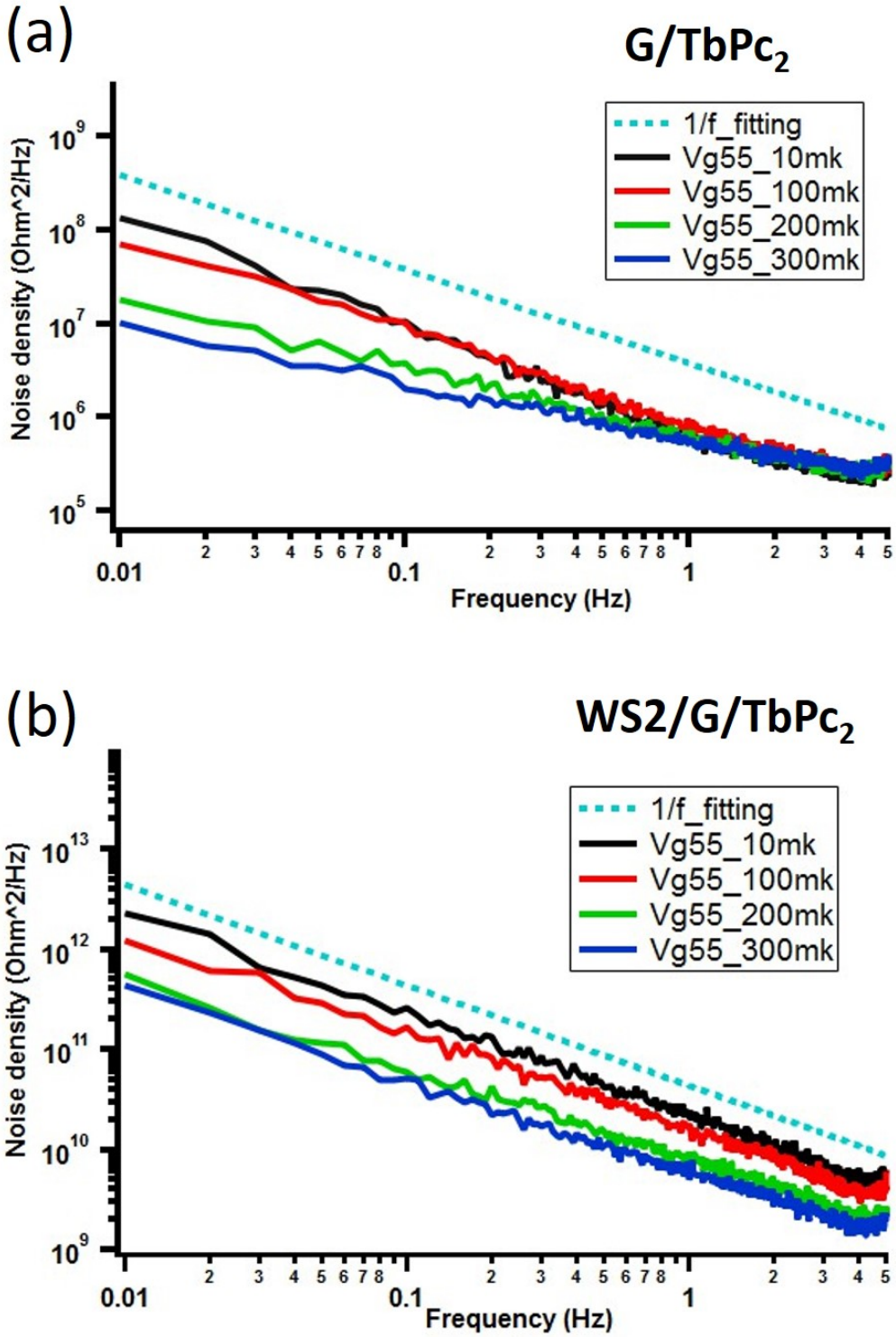


Fig. 1.3.4 (a) 1/f fitting of experimental results of Noise spectral density at different temperatures. The noise magnitude increases at low temperatures. (b) Same measurements with (a). The noise magnitude increases at low T due to the increase of UCF, which rise at low T.

# Chapter 2

# THEORETICAL CONCEPTS

In this chapter, the main idea is to introduce the quantum transport in graphene, such as the superconducting Proximity effect or how it behaves when a magnetic field is applied. The other important part will be to present a comprehensive understanding of the magneto-resistance of monolayer graphene and also the most studied phenomenon of 1/f noise.

## 2.1 Graphene

In 1947, P. R. Wallace first wrote and published the band structure of graphene using the "tight binding" calculation, and revealed the unusual semi-metallic behavior [36], bbut It was initially assumed that two-dimensional material structure could not naturally exist because it would be unstable to exist thermodynamically. Until A. Geim and K. Novoselov reported the first isolated graphene using mechanical exfoliation in 2004 [37]. Unexpectedly, it generated high-quality graphene simply with 3M scotch tape, and the result was reproduced by many researchers. Such breakthrough in graphene has excited a huge amount of research on graphene materials due to the outstanding features of the graphene monolayer. Because of their achievement in graphene, they have awarded the Nobel Prize in Physics in 2010. They also first experimentally illustrated many superb physical properties of graphene, like massless Dirac fermions and high mobility [1]. Due to the special band structure of graphene, the density of carriers can be adjusted through electrostatic gating and vary the sign of charge when the applied gate voltage approaches the Dirac point (electron-hole symmetry point).

**Band structure of graphene**

Monolayer graphene consists of a planar honeycomb lattice of carbon atoms, see Figure 2.1.1. The in-plane bonds in the graphene structure comprised $2_{px}$ and $2_{py}$ orbitals hybridized in a $sp^2$ configuration. In the meantime, the $2_{pz}$ orbital perpendicular to the layer formed covalent bonds. The $\sigma$ bonds offer rigidity to the structure, and the $\pi$ bonds bring about the valence and conduction bands, see Figure 2.1.1. These highly mobile electrons are called $\pi$ electrons. These $\pi$ orbitals overlap and can enhance the carbon bonds in graphene. Basically, the electronic properties of graphene are affected by these $\pi$ orbitals.

The structure of graphene is a basis of two atoms per unit cell and can be seen as a triangular lattice, shown in Figure 2.1.2 (a). The lattice vectors are

$$a_1 = \frac{a}{2}(3, \sqrt{3}), \quad a_2 = \frac{a}{2}(3, -\sqrt{3}) \tag{2.1.1}$$

Where the carbon A and carbon B distance a = 1.42Å. The reciprocal-lattice can now be written as

$$b_1 = \frac{2\pi}{3a}(1, \sqrt{3}), \quad b_2 = \frac{2\pi}{3a}(1, -\sqrt{3}) \tag{2.1.2}$$

Brillouin zone of the graphene with the high-symmetry points K, $\Gamma$ and M , as seen in Figure 2.1.2 (b). The two points K and K' at the corners of the graphene Brillouin zone are

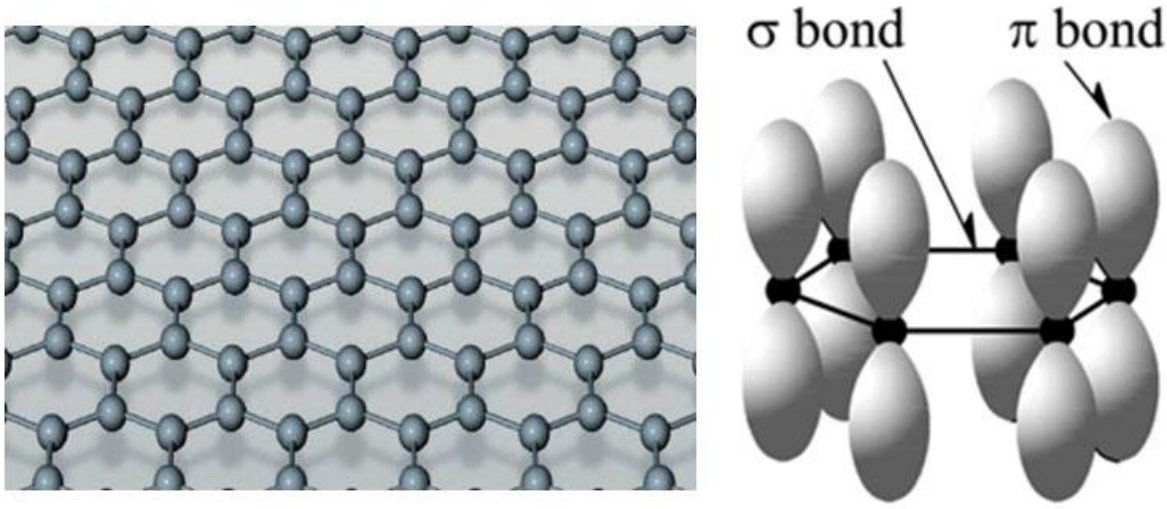


Fig. 2.1.1 Graphene honeycomb lattice structure and $\sigma$, $\pi$ bonds

especially important in the physics of graphene, which is named the Dirac point. And the positions K and K' in momentum space are given by

$$K = (\frac{2\pi}{3a}, \frac{2\pi}{3\sqrt{3}a}), \quad K' = (\frac{2\pi}{3a}, -\frac{2\pi}{3\sqrt{3}a}) \tag{2.1.3}$$

Then, the three nearest-neighbor vectors in real space are given by

$$\delta_1 = \frac{a}{2}(1, \sqrt{3}), \quad \delta_2 = \frac{a}{2}(1, -\sqrt{3}), \delta_3 = -a(1,0) \tag{2.1.4}$$

Considering the interaction of $\pi$ electrons in nearest-neighbor hopping, the eigenvalue E($k_x$,$k_y$) of graphene through tight-binding approximation can be written

$$E(kx, ky) = \pm\gamma_0 \sqrt{1 + 4\cos\frac{\sqrt{3}k_x a}{2} cos\frac{k_y a}{2} + 4cos^2\frac{k_y a}{2}} \tag{2.1.5}$$

In the equation (2.1.5), $\gamma_0$ represents the hopping energy between $\pi$ electron in the nearest-neighbor. E+ and E- are the $\pi$ electron in higher energy state ($\pi^*$) and the lower energy ($\pi$), respectively.

The graphene $\pi$ band has been calculated from the original tight-binding approximation [36] as a three-dimensional representation in Figure 2.1.3. The lower $\pi$ (valence) band is fully occupied in intrinsic graphene; the upper (conduction) $\pi^*$ band is empty. Near these, in the low energy range (ka«1), the equation (2.1.5) can be simplified by the tailor expansion

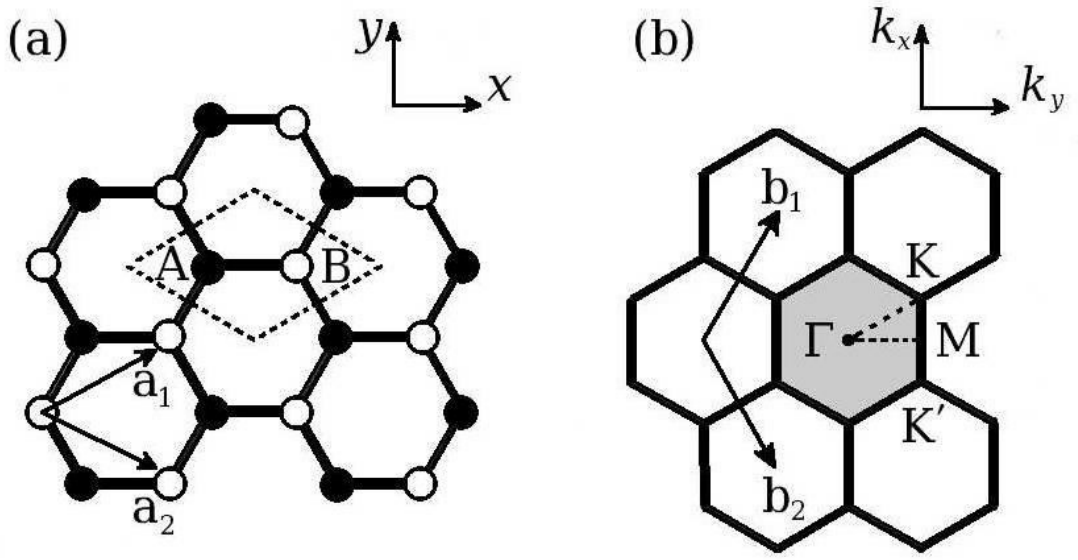


Fig. 2.1.2 Dashed line is a unit cell of graphene with two atoms. (b) The grey color corresponds Brillouin zone in the reciprocal-lattice structure. The Dirac cones are located at the K and K' points[38]

$$E(K) = \pm\frac{\sqrt{3}}{2}\gamma_0 ak = \pm \mathrm{v}_F\ \hbar\ |k| \tag{2.1.6}$$

Where the wave vector k is measured from the Dirac points, and E is the energy relative to the Dirac point. The Fermi velocity $v_F \approx 10^8$ cm/s is a material parameter. The linear dispersion is different from the normal parabolic dispersion relation with a mass dependence (E=$\frac{\hbar^2 k^2}{2m}$) that demonstrates the charge carriers moving with a velocity is independent of the energy, therefore acting as massless particles with velocity $v_F$.

This property is the most intriguing feature of graphene, making it the object of large scientific research globally. The carrier density n as $E_F = \hbar \mathrm{v}_f \sqrt{\pi n}$ represents the Fermi energy and implies that it is possible to tune the Fermi energy by changing the carrier density, electrons or holes through the graphene field effect transistor bias gate. The density of state $D(E)$ of graphene can be written as $D(E) = \frac{2E}{\pi\hbar^2 v_F^2}$. The density of states of usual two dimensional electron gases with parabolic energy dispersion are energy independent. But the density of the state $D(E)$ of graphene vanishes linearly at the Dirac point. Graphene has electrons and holes as a carrier, and intrinsic carrier concentration $n_i$ are

$$n_i = n = p = \frac{\pi}{6}\frac{kT^2}{\hbar^2 v_F^2} \tag{2.1.7}$$

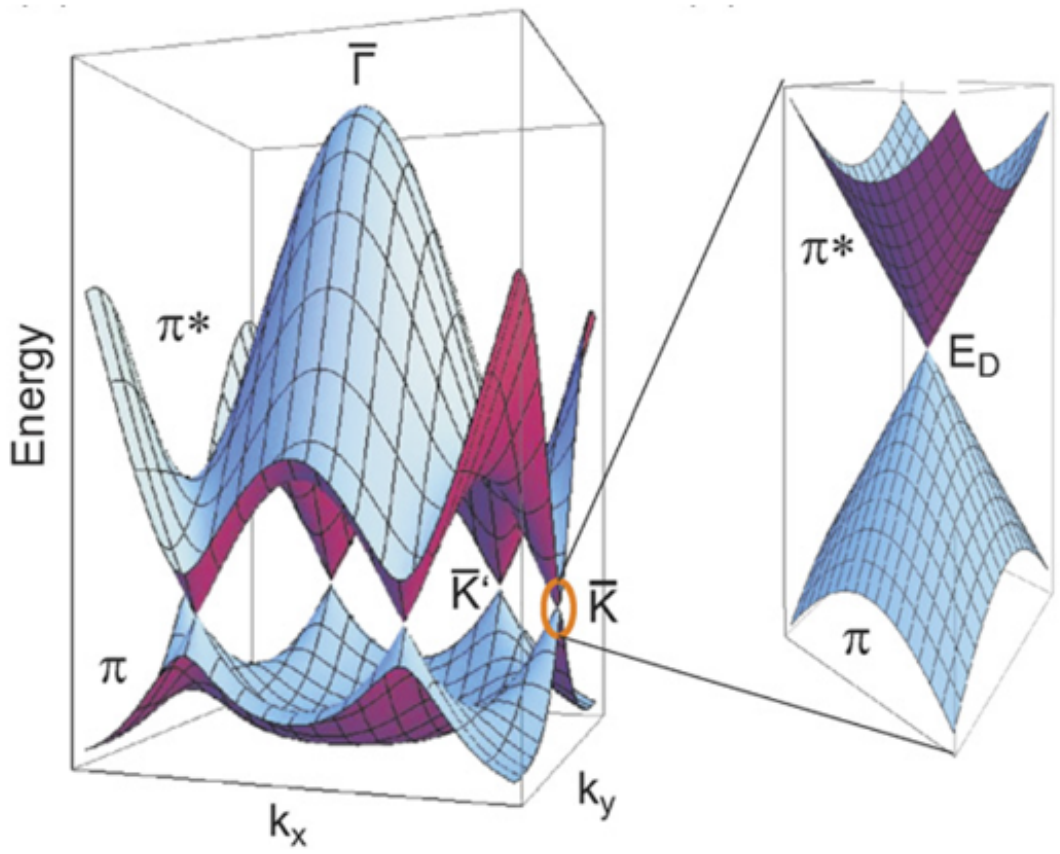


Fig. 2.1.3 The left part is the graphene $\pi$ and $\pi^*$ band dispersion calculated within tight-binding approximation. The right part shows the zooming of the Dirac cone at K point of the hexagonal Brillouin zone of graphene [39]

At room temperature with $v_F \approx 10^8$ cm/s, $n_i \simeq 8.2{*}10^{10}\ cm^{-2}$, and the The electron (hole) concentration in graphene can be obtained

$$n = \int_0^{\infty} \frac{2|E|}{\pi\hbar^2 v_F^2} f(E))dE \qquad p = \int_{-\infty}^{0} \frac{2|E|}{\pi\hbar^2 v_F^2} (1 - f(E))dE \tag{2.1.8}$$

Where $f(E) = (1 + e^{\frac{E-E_F}{kT}})^{-1}$. Based on the level of Fermi energy with regard to the Dirac point, the majority of graphene can be turned to be electrons or holes, see in 2.1.4.

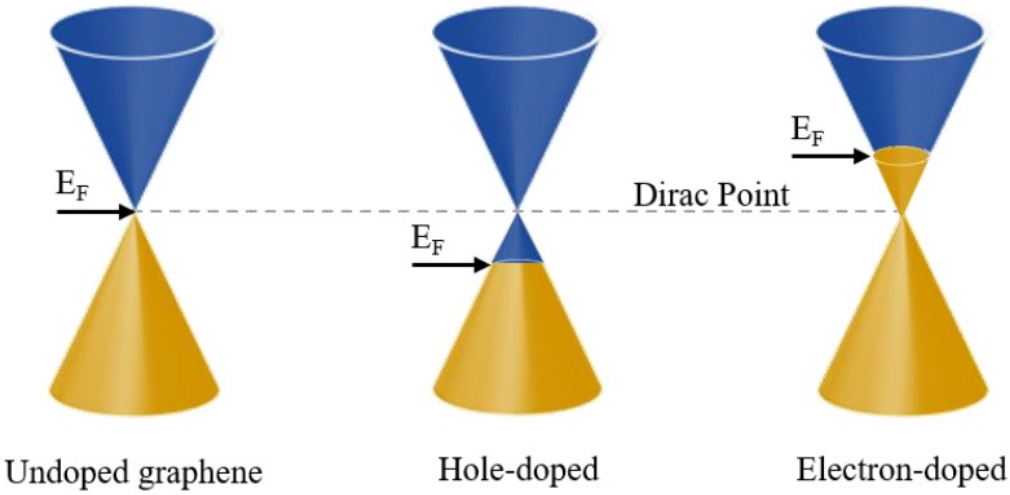


Fig. 2.1.4 The linear dispersion of Dirac cone in conduction and valence bands contact at the K point, as Dirac point. The majority carrier can be tuned via a bias gate in a graphene field effect transistor.

The control of the Fermi level is able to change the doping from n-dominated transport to p-dominated transport (and vice versa). In this case, the carrier density is zero at T=0K. On the other hand, for the T > 0K, there is always a non-zero carrier density. The low-energy physics of graphene near the Dirac point has been well investigated with respect to two-component wavefunctions according to the particle density of the two sublattices A and B:

$$\psi_{\pm,k}(\vec{k}) = \frac{1}{\sqrt{2}} \begin{pmatrix} e^{-i\theta_{\vec{k}/2}} \\ \pm e^{i\theta_{\vec{k}/2}} \end{pmatrix} \tag{2.1.9}$$

Here $\theta_{\vec{k}} = arctan\frac{k_x}{k_y}$ and the signs corresponding to the $\pi^*(+)$ and $\pi$ bands. This wavefunction play an crucial role in completing rotation of $2\pi$ of the momentum when constant energy close to Dirac point. In fact, in place of expected 0 or $2\pi$ phase, the wavefunction goes through a phase change of Berry's phase $\pi$ [40]. The relevance of Berry's phase has been known as highly related to magneto-transport phenomena, such as the unusual quantum Hall effect with applying an external magnetic field [41], leading to the formation of a Landau Level at zero energy. The two-component wavefunction can also illustrate the sublattice A or B of graphene has a pseudospin instead of the real spin of the electrons. The pseudospin implies that backscattering in graphene is forbidden, which leads to some fascinating phenomena like Klein tunneling [15]. The pseudospin of graphene enables the introduction of a chirality [42]. Here $\theta_{\vec{k}} = arctan\frac{k_x}{k_y}$ and the signs corresponding to the $\pi^*(+)$ and $\pi$ bands. This wavefunction play an crucial role in completing rotation of $2\pi$ of the momentum when constant energy close to Dirac point. In fact, in place of expected 0 or $2\pi$ phase, the wavefunction goes through a phase change of Berry's phase $\pi$ [40]. The relevance of Berry's phase has been known as highly related to magneto-transport phenomena, such as the unusual quantum Hall effect with applying an external magnetic field [41], leading to the formation of a Landau Level at zero energy. The two-component wavefunction can also illustrate the sublattice A or B of graphene has a pseudospin instead of the real spin of the electrons. The pseudospin implies that backscattering in graphene is forbidden, which leads to some fascinating phenomena like Klein tunneling [15]. The pseudospin of graphene enables the introduction of a chirality [42] as the projection of pseudospin on the direction of movement. The chirality of the electrons in graphene within one valley has important implications on the electronic transport property. In particular, a non-trivial Berry phase is related with the rotation of the 1/2-pseudo spinor, that plays a important role to comprehend the unique charge transport. And many of the fascinating physical phenomena revealing in graphene are controlled by the unique chiral nature of the charge carriers in graphene due to their quasi relativistic quasiparticle dynamics described by the effective massless Dirac equation.

## 2.2 Spin-orbit interaction in graphene

It has been known for a long time that graphene exhibits many exciting and novel properties. Nevertheless, graphene has rather weak spin-orbit interaction(SOI) in condensed matter physics due to the small atomic number of carbon. The density functional theory(DFT) calculation shows the intrinsic SOI of graphene is only $24\mu$eV [43]. SOIs play an important role either in the electrical manipulation of spins in the field of spintronics [44] or in driving novel topological phenomena [45]. The electronic transport of graphene is easily influenced because of the interaction of the exposed 2D electrons with the substrate. The electronic transport of graphene is easily influenced because of the interaction of the exposed 2D electrons with the substrate. Since the magnetism of graphene has been proven successfully induced by a yttrium iron garnet (YIG, Y3Fe5O12) substrate [46], it may be a promising way to induce strong SOIs in graphene by choosing a proper substrate.

Transition-metal dichalcogenides (TMDs) are a highly promising class of materials within high spin-orbit materials. TMDs are composed of three atomic planes and often two atomic species with $MX_2$ composition: a transition metal M and two chalcogens X. Some common 2D TMDs are composed with M, either Mo or W, and X, either S or Se, where the heavy element (Mo or W) is sitting on the hexagonal lattice in the trigonal-prismatic (2H-) structure. In the monolayer TMDs framework, it's similar to graphene in that the bottom of the conduction bands and the top of the valence bands are located at inequivalent $K$ and $K'$ valleys. Yet a larger band gap between 1 and 2 eV between bands results in the semiconductors property of TMDs and higher resistance than graphene. In the TMDs, thanks to the heavy elements, the intrinsic SOI is up to 1 to a few meV for the conduction bands and 100 - 400 meV for the valence bands [47].

Depending on the theoretical prediction from first-principles calculations, there are three different types of SOIs that can be induced in graphene by TMDs, Kane–Mele (KM, or intrinsic), Rashba, and Valley–Zeeman (VZ) SOI, shown in equation (2.2.1). The Kane-Mele is an intrinsic SOI that is present in the pristine graphene. In the 2D materials, the linear dependence of the Rashba SOC with the electronic wave vector k results in the splitting into an inner and outer branches, thus Rashba SOI in the system is broken the $z \to -z$ symmetry.

$$\begin{aligned} &Intrinsic\ type\ SOI : H_I = \lambda_I k \sigma_2 s_2 \quad (z \to -z\ symmetric) \\ &Rashaba\ SOI : H_R = \lambda_R (k\sigma_x s_y - \sigma_y s_x) \quad (z \to -z\ asymmetric) \\ &Valley - Zeeman(VZ)\ SOI : H_{VZ} = \lambda_{VZ} k s_z \quad (z \to -z\ symmetric) \end{aligned} \tag{2.2.1}$$

Where $k$ is the valley component, and $\lambda$ is the sublattice component. In the Valley–Zeeman (VZ) SOI, the sublattices A, and B of graphene generally have different spin-orbit potential from TMDs caused by the lattice mismatch between graphene and TMD. The VZ SOI turns out to be significant when heavy elements break the sublattice symmetry [48].

$$\begin{aligned} H^I_{A/B} &= \frac{1}{2}\left[\lambda^A_I(\lambda_z+\lambda_0+\lambda^B_I(\lambda_z+\lambda_0\right] kS_z \\ \lambda_I &= (\lambda^A_I+\lambda^B_I)/2,\ \lambda_{VZ} = (\lambda^A_I+\lambda^B_I)/2 \end{aligned} \tag{2.2.2}$$

The $\lambda^A_I(\lambda^B_I)$ is the induced spin-orbit potential at the sublattice A(B). However, the first principle calculations predict the existence of the induced SOI is 'valley-Zeeman' type SOC in graphene by TMD [49].

## 2.3 Superconducting proximity effect in graphene

Many metals can become superconductors when the temperature is below a critical temperature $T_c$ [50]. Below this temperature, the Cooper pairs have been formed when electrons close to $E_F$, which comprises two electrons with opposite wave vectors and opposite spins. The Cooper pairs form a collective state $\psi(r) = |\psi(r)|\, e^{i\phi r}$ at $E_F$, where $\phi(r)$ is the phase of the superconducting state. The normal density of states disappears in the range, giving rise to a gap at $E_F$ whose amplitude is $\propto T_c$ of the N/S interface that generates an energy gap at $E_F$. The electric current carried by the Cooper pairs remarkably turns to be dissipationless, leading to the zero resistance of a superconductor when the temperature is below its critical temperature.

### Andreev Reflection

At the Fermi level, metal has a continuous density of states, and the superconductor has an energy gap. An electron passes through a metal at the $E_F+\varepsilon$ interface, if $\varepsilon < \triangle$, see Figure 2.3.1. In that case, the electron has to form a Cooper pair with another electron in order to enter the superconductor, which results in the extraction of a second electron with opposite momentum and spin from the metal. The process leaves a hole in the metal due to the charge conservation. The process in which the incident electron forms a Cooper pair in the superconductor with the reflection of a hole with opposite spin in the metal is called Andreev reflection [51]. The first electron wavevector $K^1_e$ and the second electron with opposite wavevector $K^2_e = -K^1_e$ form a Cooper pair. The wavevector of the hole left in the metal $K_h = -K^2_e = K^1_e$. The velocities of the initial electron and the reflected hole are opposite

but equal in momentum because the velocity and wavevector are parallel (antiparallel) for electrons (holes). Then, the reflected hole retraces the path of the incident electron , which is called retro-reflection.

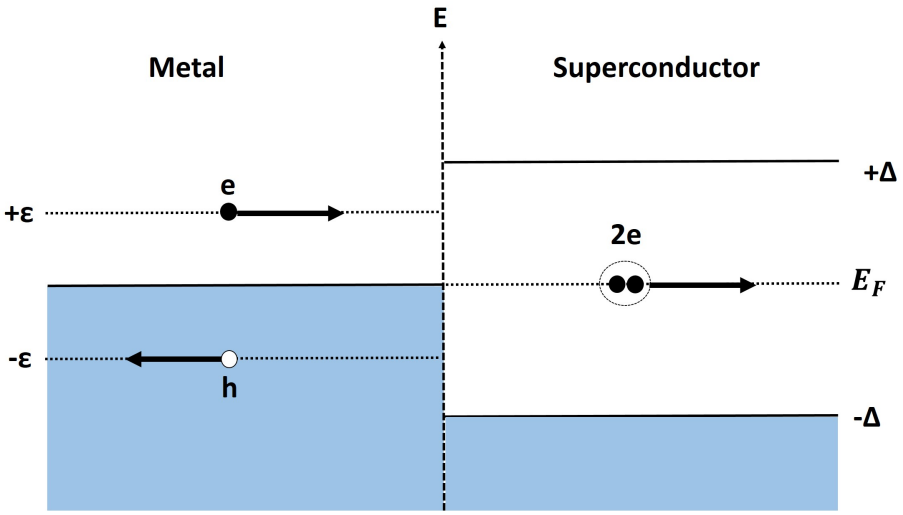


Fig. 2.3.1 Illustration of Andreev reflection process in the metal-superconductor interface. After the Cooper pair formed in the superconductor, the incident electron reflected as a hole.

**Andreev Bound state (ABS)**

The Andreev reflection appears at the interface of two NS boundaries in the SNS junction, and these reflections generate phase-dependent boundary conditions in the N area, which are the coherent superposition of electron and hole wavefunctions. Meanwhile, the formation of standing waves leads to the quantization of excitation energy levels. These standing waves are known as the Andreev bound state (ABS). To start with a simple case of a ballistic junction, we presume a ballistic region of length $L_N$ [52]:

$$\Delta(r) = \begin{cases} \Delta_0 e^{i\phi_1}, & if \quad z < 0 \\ 0, & if \quad 0 < z < L_N \\ \Delta_0 e^{i\phi_2}, & if \quad z > L_N \end{cases} \tag{2.3.1}$$

Through the equation of the phase shift acquired from a round trip to an integer multiple of $2\pi$, the bound states of $\varepsilon < \Delta_0$ can be found. The condition is:

$$\frac{2\varepsilon L_N}{\hbar v_F \cos\theta} - 2\arccos\frac{\varepsilon}{\Delta_0} \pm \Delta_\varphi = 2\pi m, \quad m = 1,2,..... \tag{2.3.2}$$

The $\Delta_\varphi = \varphi_1 - \varphi_2 \in (-\pi,)$, $\theta$is the angle with the normal to the N/S interface. The two-direction motion of the electron or hole is presented by the $\pm$. Due to the $\varepsilon = [(2m+1)\pi \mp \Delta\varphi]\hbar v_F \cos\theta/(2L_N)$, the spectrum is based on $\delta\varphi$ linearly for the $\varepsilon \ll \Delta_0$, see in the Figure 2.3.2. The first term represents the phase accumulation during the propagation in the normal part. The second term results from the Andreev reflection at the interface.

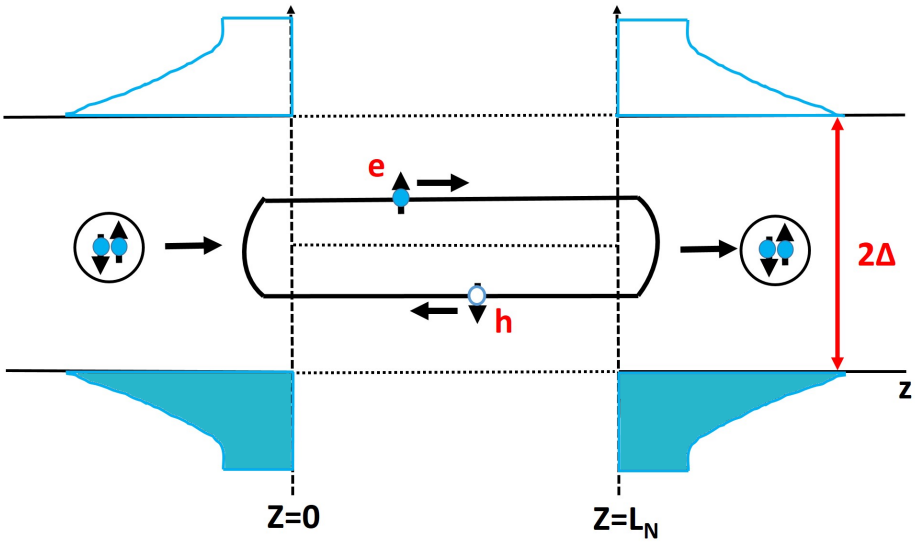


Fig. 2.3.2 Andreev bound state, taken from [53]. An Andreev pair is formed by an electron and a hole, which requires constructive interference between the electron and the hole and confined between the energy $\pm\Delta$.

**In the long junction limit:** For $L_N \gg \xi_0$, the energy spectrum of the SNS junction is based on $L_N$. The Josephson current is a linear function of $\Delta\varphi$. The critical current can be written as:

$$I_c = aG\hbar v_F / eL_N \tag{2.3.3}$$

where $a$ is a numerical coefficient of order unity based on the dimension of the system, and G is the conductance of the normal state in the SNS junction. In the long junction limit, if the SNS junction carries a constriction of the normal region, the $I_c$ on the $L_N$ junction geometry is persisted [54].

**In the short junction limit:** On the contrary, for the $L_N \ll \xi_0$, there is only a single

bound state remains for each of the N transverse modes when the energy $\varepsilon = \Delta_0 \cos(\Delta_\varphi/2)$ is independent of $L_N$. The supercurrent can be written by the sum of the contribution of the energy levels:

$$I(\delta_\varphi) = N\frac{e}{\hbar}\Delta_0 \sin(\delta_\varphi/2), \quad -\pi < \delta_\varphi < \pi \tag{2.3.4}$$

And critical current is given by:

$$I_c = N\frac{e\Delta_0}{\hbar} \tag{2.3.5}$$

Both equations are independent of $L_N$.

**Supercurrent and Andreev Reflection in Graphene**

In normal metals, Andreev reflection is intraband proceeded, which means the electron and the Andreev reflected hole both are in the conduction band. Meanwhile, Interband Andreev reflection cannot take place in normal metals. However, both intraband and interband Andreev reflections happen in graphene, that depends on the position of the Fermi level. Two different regimes in graphene can be distinguished [55].

Suppose an electron with wave vector $k$ traveling in a graphene monolayer toward a superconductor. When an electron reaches the interface, it forms a Cooper pair with a second electron with wave vector $-k$. Both electrons have opposite wave vectors and originated from two different graphene valleys $\pm k$. Therefore, Andreev reflection proceeds the connection of both graphene valleys, as in Figure 2.3.3.

When the initial electron with energy $E_F + \varepsilon$ and $\varepsilon < E_F$ is in the conduction band, the Andreev reflected hole with energy $E_F - \varepsilon$ also stays in the conduction band, see Figure 2.3.4(a). In this circumstance, the initial electron travels toward the interface. Meanwhile, the hole moves in the opposite direction, away from the interface. Thus, the value of velocity in X direction $v_x$ has to change the sign to $-v_x$. In addition, the wave vector $k_y$ should be conserved after reflection. The Figure 2.3.4(a) shows the $v_x$ and $v_y$ change signs, $v_x^h = -v_x^e$ and $v_y^h = -v_y^e$. In consequence, the reflected hole can retrace the path of the initial electron, which shows that intraband Andreev reflection in graphene leads to retro-reflection in normal metals. On the other hand, if the original electron has an energy $E_F + \varepsilon$ and $E_F < \varepsilon$ with both $E_F$ and $\varepsilon$ smaller than the superconducting gap $\triangle$, the reflected hole with energy $E_F - \varepsilon$ will move to the valence band, see in Figure 2.3.4(b). The Andreev reflection will occur when the

$v_x$ change sign and $k_y$ have been conserved. As the velocity of the electron in the valence band is parallel to its wave vector, the velocity won't change the sign. Therefore, interband Andreev reflection results in the specular reflection that is a unique property of graphene [55].

In addition to the Andreev reflection, Josephson supercurrent also shows the difference when it's close to the Dirac point. In short ballistic graphene Josephson junctions $L > \xi$, if the the Fermi wave length $\lambda_F < L$, the critical current is $I_c = \frac{e\triangle}{\hbar}\frac{W}{\lambda_F}$, where is the high doping regime $E_F > \frac{\hbar v_F}{L}$. On the other hand, if $\lambda_F > L$, the critical current is $I_c = \frac{e\triangle}{\hbar}\frac{W}{L}$, which is in the vicinity of the Dirac point $E_F < \frac{\hbar v_F}{L}$ [55, 56]. This result indicates that the critical current is length independent at a high-density regime. Yet its length is dependent close to the Dirac point.

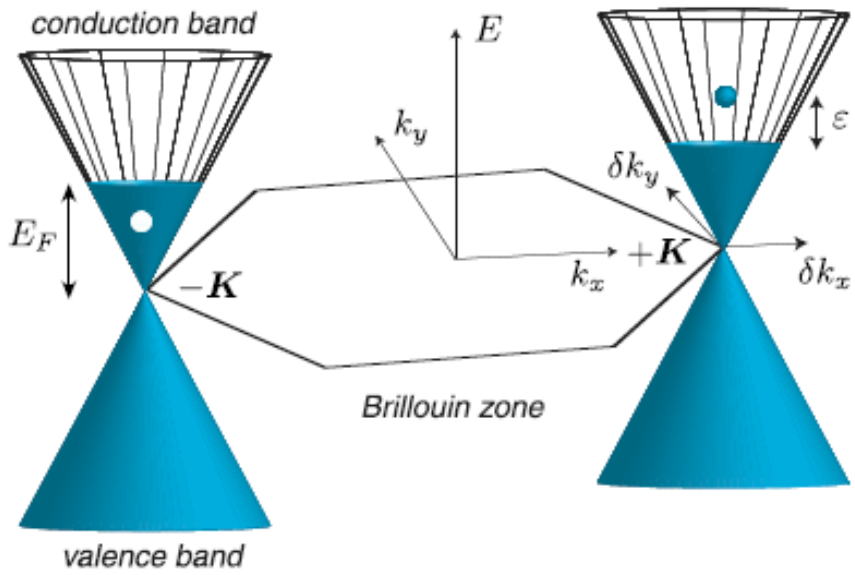


Fig. 2.3.3 Electron and hole in the band structure of graphene. Andreev reflection results in the coupling of both valleys in graphene [55].

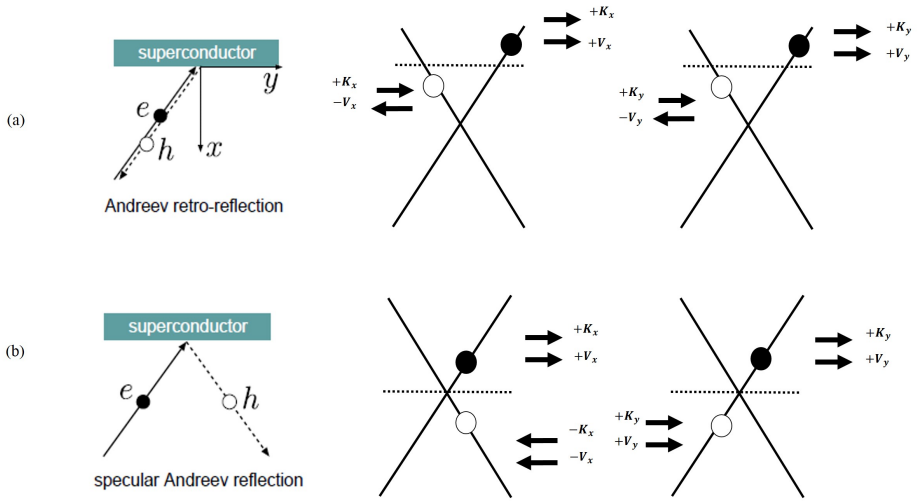


Fig. 2.3.4 Andreev retro-reflection and specular Andreev reflection in graphene [55]. An extra illustration of $k_x$ and $k_y$ of the incident electron with the reflected hole is displayed in both processes.

## 2.4 Phase coherent electron transport

In mesoscopic systems, electron transport can be described by two important characteristic length scales at low temperatures, as the Figure 2.4.2. First, the mean free path ($l_m$) illustrates the average distance of electron crossing through the conductor that experience no scattering processes. When the dimensions of a conductor are smaller than the mean free path, no scattering process happens during the electron propagation, and motion is considered to be ballistic transport. On the contrary, when the ($l_m$) is much lower than the dimensions of the conductor, electrons scatter several times during the propagation process, the direction of motion varying each time. In this regime, the electron motion change to be diffusive. The other crucial length scale is the phase coherence ($L_\phi$) that illustrates the electron propagation without losing the phase information within a certain length. When $L_\phi$ is long enough, quantum phenomena because of the wave character of electrons turn visible in the experiment. The weak localization correction and universal conductance fluctuations can be good examples.

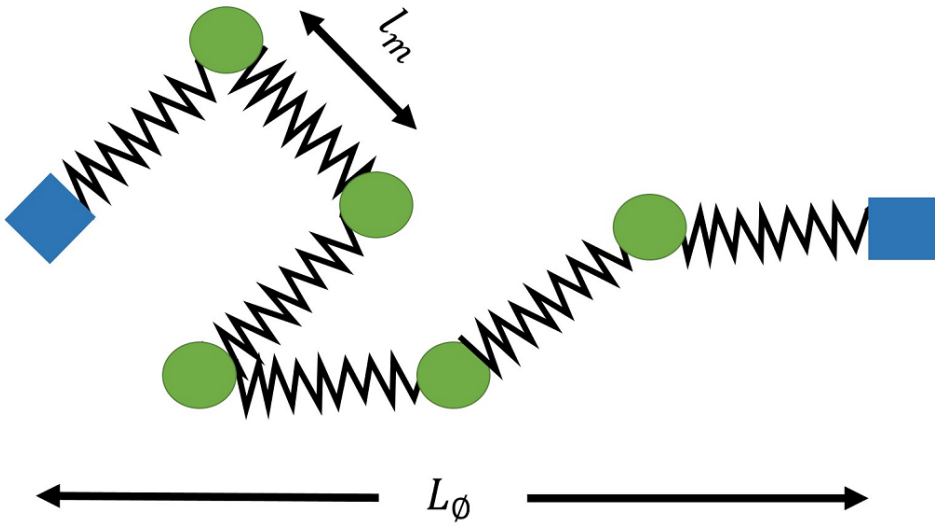


Fig. 2.4.1 Graphic illustration of electron propagation in a conductor. In this case, the mean-free path $l_m$ is much shorter than the phase coherence length $L_\phi$. Wiggled lines behave in electron motion, green circles elastic collisions, and blue squares inelastic collisions [57].

The coherence length relies upon the nature of the impurity scattering. The Elastic scattering does not vary the electron energy, and the phase coherence is preserved normally. On the other hand, inelastic scattering processes ruin phase coherence. The main reasons why the inelastic processes that result in the shortening of $L_\phi$ are electron-electron interaction

and electron-phonon interactions. By decreasing the temperature below 1K, the rate of the inelastic processes is lowered. Therefore $L_\phi$ increases and the quantum interference effects become more pronounced [58, 59].

In order to explain the physics related to the effects of electronic interference on transport, a semi-classical approach describes the electron motion in terms of partial waves or trajectories related to the quantum amplitude of probability. In a diffusive conductor system, there are various possible trajectories that connect two different points. For the purpose of calculating the probability of an electron propagating from $r_1$ to $r_2$ during a given time t, P($r_1$; $r_2$; $t$), it needs to take all trajectories into account. The propagation probability is given by the absolute value of the amplitude squared of the sum of all individual probability amplitudes $A_i$ associated with the different trajectories [60, 61].

$$P(r_1, r_2, t) = \left| \sum_i A_i \right|^2 \tag{2.4.1}$$

This equation can be rewritten as

$$P(r_1, r_2, t) = \left| \sum_j A_j \right|^2 + \sum_{j, j' \neq k} A_j A_k e^{i(\phi_j - \phi_k)} \tag{2.4.2}$$

The phases corresponding to trajectories j and k aree $\phi_j$ and $\phi_k$. The first term is the classical diffusion probability, which means the sum of the modulus square of the probability amplitudes in individual trajectories. The second term is caused by quantum interference in the different trajectories. If the effect of interference can be neglected, then the second term is omitted. The equation can be written as a classical result (i.e., sum over probabilities)

$$P(r_1, r_2, t) = \left| \sum_j A_j \right|^2 \tag{2.4.3}$$

### 2.4.1 Weak localization

Weak localization has been primarily observed in electronic systems and reported as quantum interference between electronic waves that constructively scatter through the impurities in conductors. Weak localization has brought a lot of interest as a particular case where the quantum mechanical behavior of electrons is an observable consequence in the macroscopic systems.

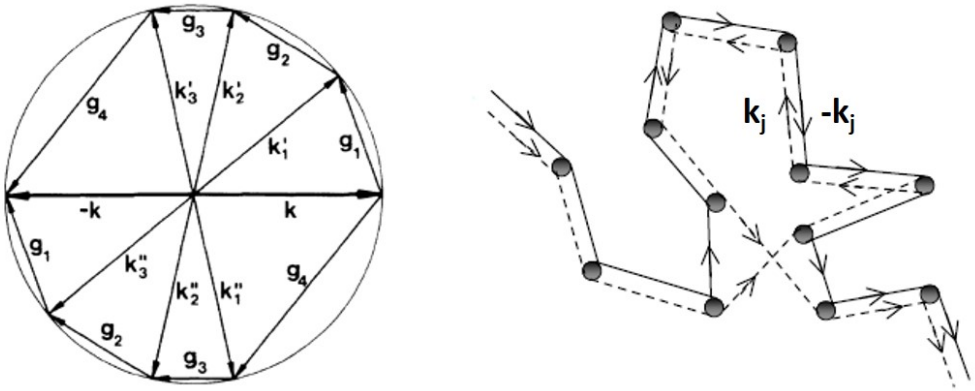


Fig. 2.4.2 (left) Graphic illustration of the mechanism of weak localization. (right) The time-reversed trajectories $k_j$ and -$k_j$ have identical probability amplitudes and interfere constructively at the point of departure, giving rise to a weak localization effect.

The scattering result from the defects in the bulk in the transport systems. The multiple scattered waves form the statistical distribution of the impurities in a random pattern. The weak localization(WL) correction of the conductivity is caused by the interference of time-reversed paths. For instance, the corresponding scattering process in k-space for a pair of paths has shown in Fig. 2.4.2. The scenario of the general reflection path of an electron: After the time $\tau_0$, the electron ($\vec{k}$) has scattered in a state $\vec{k'}_1$, then $2\tau_0$ into the state $\vec{k'}_2$. After n times scattering, the electron has scattered into the state $\vec{k}$. The scattering sequence can be written as follows:

$$\vec{k} \Rightarrow \vec{k'}_1 \Rightarrow \vec{k'}_2 \ldots \vec{k'}_n = -\vec{k} \tag{2.4.1.1}$$

The scattering sequence is drawn in Fig 2.4.2, where $\vec{g}_1, \vec{g}_2, \cdots \vec{g}_n$ represent the momentum transfer, and the probability of the electron k is equally scattered after n steps from the state $\vec{k}$ into $\vec{k}$ through another sequence

$$\vec{k} \Rightarrow \vec{k''}_1 \Rightarrow \vec{k''}_2 \ldots \vec{k''}_n = -\vec{k} \tag{2.4.1.2}$$

where the momentum transfer is $\vec{g}_n, \vec{g}_{n-1}, \cdots \vec{g}_1$. The complementary scattering series has the same variation of momentum in the opposite sequence. The intermediate states stay symmetrical to the origin for both scattering paths. The most crucial point is that the amplitude of the final state $\vec{k}$ is the same for both scattering paths, along with the same energy of the corresponding intermediate states. The probability amplitudes $A'$ and $A''$ are phase coherent, and they will be equal. $A_1 = A_1 = \mathrm{A}$, so that the total intensity given by

$$\left|A' + A''\right|^2 = \left|A'\right|^2 + \left|A''\right|^2 + A'A''^* + A'^*A'' = 4\left|A\right| \tag{2.4.1.3}$$

Eq. (2.4.1.5) shows an increased resistance can be observed due to the quantum interference effects, as the probability of an electron to be found in its original state and thus no propagation through the conductors. This increased resistance occurs due to a quantum interference phenomenon called weak localization. However, in the presence of time-reversal symmetry 2.4.2 (right panel), trajectories in which an electron goes back to the beginning point offer a non disappeared contribution to interference. The trajectories can be opposed in a clockwise and counterclockwise direction, with exactly the same amplitude due to the time-reversal symmetry in Fig. 2.4.2. To briefly sum up, when there is no applied magnetic field, interference leads to an enhanced probability for electrons to go back to the original position where they started from.

When we remove time-reversal symmetry, the weak localization can be suppressed between counter-propagating trajectories around the loop. This can be done by applying a magnetic field. The probability amplitudes of clockwise ($A_j$) and counterclockwise ($A_{j'}$) propagation gain different phase shifts through the following equations

$$\begin{aligned} \triangle\phi_j &= k_F L - \frac{e}{\hbar}\int_{r_1}^{r_2} A dr_j \\ \triangle\phi_{j'} &= k_F L - \frac{e}{\hbar}\int_{r_1}^{r_2} A dr_j \end{aligned} \tag{2.4.1.4}$$

where $\phi_j$ is the phases corresponding to trajectories j as in equation (2.4.2). $dr_{j'}$ is expressed -$dr_j$. The first terms in the equations indicate a standard dynamical phase, and the second terms correspond to Aharonov-Bohm phases resulting from the vector potential A, which is related to the applied magnetic field. When the magnetic field is non-zero, the phase difference develops between two trajectories, which means breaking of time-reversal symmetry. The total phase difference between the two interfered paths becomes

$$\triangle\phi_{j'} - \triangle\phi_j = \frac{2e}{\hbar}\int_{r_1}^{r_2} A dr_j = \frac{2e}{\hbar}\int_S \bigtriangledown \times A dS = \frac{2e}{\hbar}\Phi \tag{2.4.1.5}$$

where $\Phi$ is the magnetic flux closed by the trajectory. The different counter-propagating trajectories enclose different areas, and the phases accumulated in a magnetic field are random. Thus the interference term giving rise to weak localization averages out. At magnetic fields higher then $\sim \hbar/2eL_\phi^2$, weak localization is completely suppressed [61]. The development of weak localization in applying a magnetic field is a useful method to determine the average coherence length of electrons, scattering of charge carriers, and affecting transport properties of samples.

### Weak anti-localization

In normal metals, the probability of electrons moving in closed loops can be increased by constructive electron interference along time-reversal trajectories. As a consequence, the conductance will be smaller compared to the classical Drude case, which is called weak localization (WL), as we mentioned before. On the other hand, in the case of the presence of strong SOI, the spin precession of electrons results in a phase shift, which causes destructive interference and a positive correction to the Drude conductance. This phenomenon is weak anti-localization (WAL) [62]. WAL in the two-dimensional system with SOI has been theoretically studied [62], which states the WAL correction to the Drude conductivity.

The band structure of the Dirac materials, such as graphene and TMDs, are characterized by a non-trivial Berry phase that develops a phase shift to the electron interference $\phi_B = \pi(1 - E_g/u)$, where $E_g$ is the band gap or Dirac mass, and $u$ is the chemical potential. In the massless limit case, such as graphene, the phase shift $\phi_B = \pi$ result in the WAL [63]. On the contrary, in the large mass limit case, no phase shift has been introduced that results in the WL.

When strong SOC is introduced into graphene by TMDs, the spin degree of freedom generates an extra $\pi$ phase to the quantum interference and displays the WAL [64]. In the case of the WAL resulting from chirality, the WAL only reveals when the temperature is above 50K [65], in which the dephasing rate exceeds the intervallery scattering rate and excludes the intervalley associated interference. But in the strong SOC-induced WAL, the WAL can be observed only at low temperatures when the dephasing rate is below the spin relaxation rate, which leads to SOC-associated interference.

In a nutshell, WAL (WL) can be observed experimentally in applied a perpendicular magnetic field, which breaks the time-reversal symmetry to suppress the electron interference [62]. By fitting the magneto-conductance data with the theoretical model, one can extract the dephasing rate and the spin relaxation rates from the fitting result, then estimate the amplitude and mechanism of SOIs by the Elliott-Yafet [66] or Dyakonov-Perelspin [67] relaxation mechanisms.

### 2.4.2 Universal conductance fluctuations

Universal conductance fluctuations (UCF) have been investigated originally in disordered metal systems at low temperatures. In this case, the mean free path is smaller than the sample length L, and the phase coherence length is $L_\phi \geq L$. The fluctuations have been found as the magnitude $e^2/h$, which is independent of the sample shape or degree of disorder in the system [68–70]. This is an unexpected and surprising result as it has been considered self-average in non-microscopic samples. In addition, although UCF looks random, they are actually reproducible. The typical correlation field scale is $B_c = \frac{\phi_0}{S}$, where S is the surface of the sample perpendicular to the B field. In this chapter, we will introduce universal conductance fluctuations (UCF).

In a diffusive mesoscopic system, if sample length L > mean free path, the electrons will be scattered by impurities several times. Therefore, there have several electron trajectories that can interfere with each other when the conductance is larger than $e^2/h$, in which the electrons will travel through the entire system and keep their phase $L_\phi > L$. The interference lead to weak (anti) localization at low field, yielding changes of conductance of the order of the quantum conductance $e^2/h$. They also depend on the impurity configuration [68–70]. According to theory read s[68–70], if the temperature is low enough, the phase coherence is long, and the thermal average can be neglected. Thus, the expression of conductance fluctuation is defined as

$$\delta G = \sqrt{Var(G)} = \frac{g_s g_v}{2} \beta^{-1/2} C \frac{e^2}{h} \tag{2.4.2.1}$$

Where C is defined as a constant by the geometry of the sample. In the case of long and narrow sample $C \simeq 0.73$; in the case of short and wide sample $C = \sqrt{W/L}$, and $g_s$ $g_v$ are spin and valley degeneracy. When the absence of a magnetic field, $\beta = 1$. When the time-reversal symmetry is broken by the magnetic field, $\beta = 2$. Quantum interference also depends on the chemical potential $\varepsilon_F$, which can be tuned by the gate voltage. The correlation energy scale is the Thouless energy given by [71].

$$E_c \approx \frac{\hbar}{\tau_F} \approx \frac{\hbar D}{L^2} \tag{2.4.2.2}$$

$E_c$ is "Thouless energy". $\tau_F$ is the time to pass through the sample of length L. And D is the diffusion constant that is equal to $v_F^2 \tau_F$. For the discussion of the graphene system, when the temperature goes from low to high, the UCF of graphene of starts to be decreased. An

experimental measurement is shown in 2.4.3. Increasing of temperature from 20mk to 2K significantly reduces the fluctuations. A new length scale, the thermal length $L_T = \sqrt{\hbar D/k_B T}$, becomes important, and it is expected without rapid change in conductance G, but the decay of $G \propto T^{1/2}$ in the two-dimensional system [70]. However, disordered single-layer graphene is quite different from a diffusive metal due to its chiral charge carriers and the presence of the valley pseudospin. Some simulation studies have shown that the UCF is strongly related to the actual impurity concentration [72, 73].

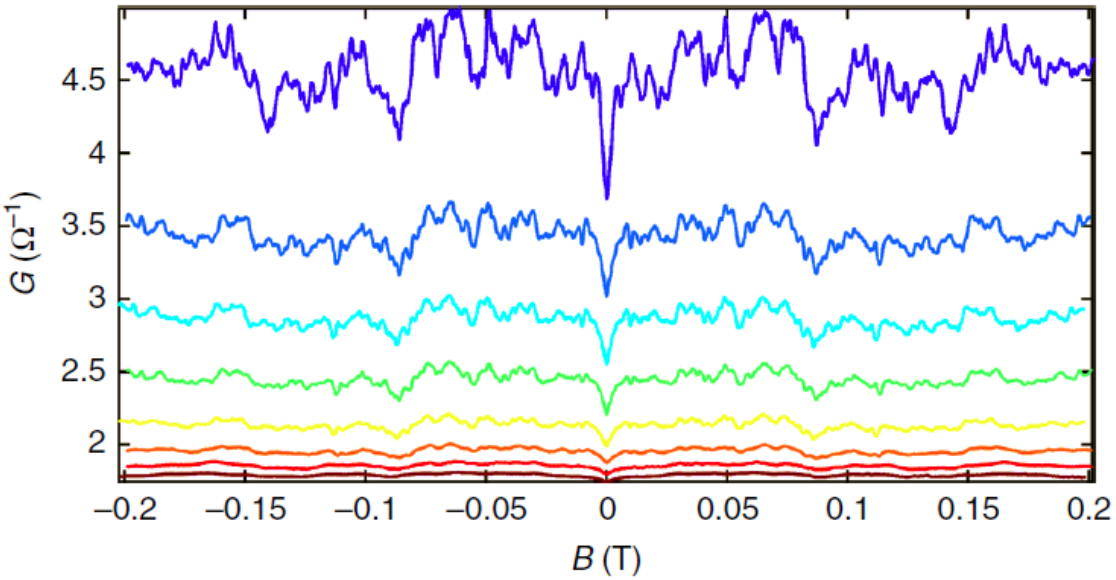


Fig. 2.4.3 Adapted from Ref [74]. UCF in graphene as illustration. The plots of the magnetoconductance G versus the magnetic field B measured at 20mK, 50mK, 75mK, 100mK, 200mK, 500mK, and 1K until 2K from top to bottom curves in different temperatures.

## 2.5 1/f noise

The universal 1/f noise power spectral density of fluctuations in the electrical parameters generally refers to the slow relaxation of the disorder from the background [75], which is a superposition of fluctuations of the characteristic time $\tau$ with a distribution $D(\tau) \propto \tau^{-1}$. The single relaxation process possesses a power spectrum:

$$S(f) \propto \frac{\tau}{1+\omega^2\tau^2} \tag{2.5.1}$$

Then, the total power spectral density of the noise is a measured sum of all relaxations over a bandwidth $(\tau_1, \tau_2)$.

$$S(f) \propto \int_{\tau_1}^{\tau_2} \frac{\tau}{1+\omega^2\tau^2} D(t)dt \tag{2.5.2}$$

which gives rise $S(f) \propto 1/f$ for $\tau_2^{-1} \ll f \ll \tau_1^{-1}$. Therefore, any random process that has a wide distribution of time scales shall exhibit a 1/f spectrum. The Figure 2.5.1 is schematic explanation of the process.

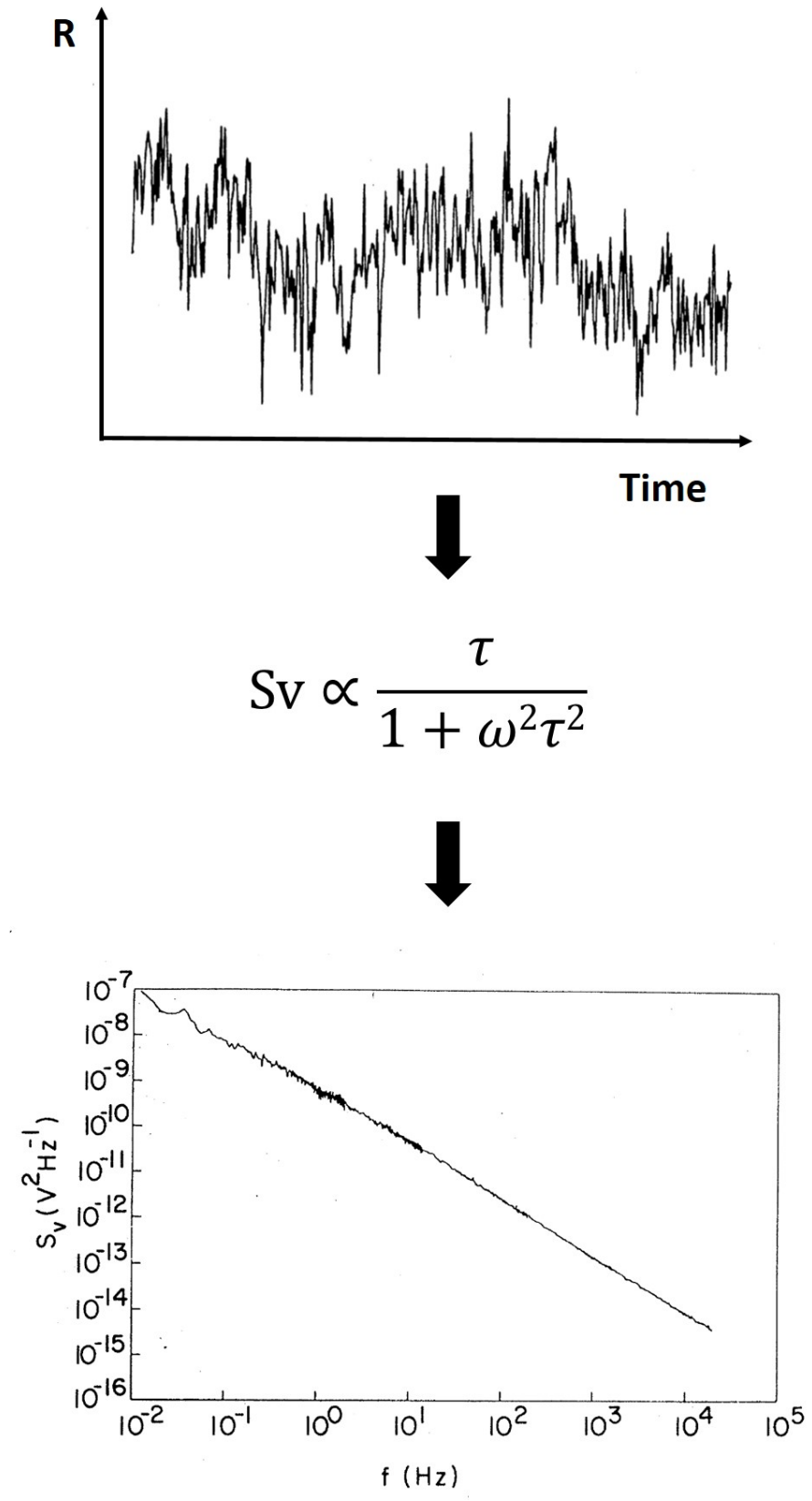


Fig. 2.5.1 Graphic illustration of the example of the 1/f spectrum from several fluctuators with a wide distribution of time scales.

The spectrum is nearly constant when the frequency is close to zero, and after a transition region, it becomes nearly proportional to $1/f^2$ with a narrow transition region where the power spectrum resembles that of the flicker noise found by Johnson. The form of Schottky's expression for the power spectrum is called a "Lorentzian." But later, Bernamont pointed out that a single relaxation process was not enough in 1937, and it had to be a superposition of such processes with a distribution of relaxation rates $\lambda$ [76]. When the relaxation rate is uniformly distributed between $\lambda_1$ and $\lambda_2$, each pulse amplitude keeps constant, and the power spectral density is

$$S(\omega) = \begin{cases} N_0^2 n & if\ 0 < \omega \ll \lambda_1 \ll \lambda_2 \\ \frac{N_0^2 n \pi}{2\omega(\lambda_2 - \lambda_1)} & if\ \lambda_1 \ll \omega \ll \lambda_2 \\ \frac{N_0^2 n}{\omega^2} & if\ \lambda_1 \ll \lambda_2 \ll \omega \end{cases} \tag{2.5.3}$$

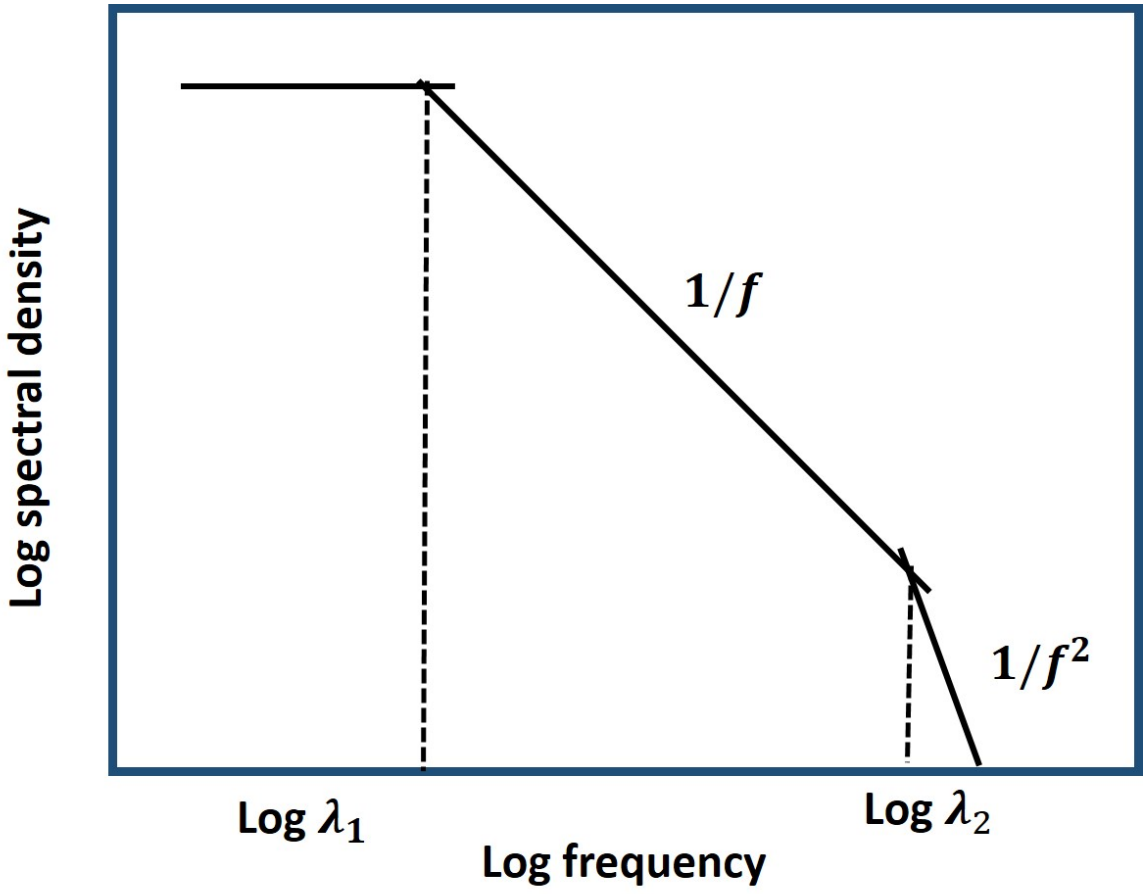


Fig. 2.5.2 Graphic illustration of respective power spectra of noises in three regions in equation (2.5.3).

Figure 2.5.1 displays some time series-associated power spectra. Such time series arise in many natural systems, like physics, biology, neuroscience, and psychology. In the figure 2.5.1, power spectra is drawn in log-log coordinates, because $log(S(f)) = log(constant/f^{\alpha}) = -\alpha log(f) + log(constant)$. On the other hand, the logarithmic transform presents the $1/f^{\alpha}$ power spectrum as a straight line with slope $-\alpha$ can be easily estimated.

### Hooge model

Hooge investigated one of the most important frameworks of 1/f noise [77], in which he presented an empirical model:

$$S(\omega) = \left\{ \frac{S_V(f)}{V^2} = \frac{\gamma_H}{Nf^{\alpha}} \right. \tag{2.5.4}$$

where §$_V$ depends on a constant current and also the power spectral density of voltage fluctuations over an electrical resistor, V and N is the average voltage drop across the sample and the total number of carriers. Here, $\gamma_H$ called the Hooge parameter, which is a dimensionless parameter and offers a normalized evaluation of the noise level in a system. Then, the 1/f noise is characterized by the frequency exponent $\alpha \approx 1 \pm 0.2$. In the Hooge model, a characteristic feature of systems is the 1/N decrease in the noise magnitude, and the Hooge parameter changes from one system to another. This model assumes the origination of the conductance noise stems from the mobility fluctuation, which is originated by the scattering of carriers. This model is able to describe clean metals and semiconductors based on the limited impact of disorder or impurities on mobility fluctuation.

In a nutshell, the $1/f$ noise has been discovered in many semiconductor devices ever since [78]. Up to now, there are plenty of noise spectra have been measured with various materials, such as metal, semimetals, semiconductors, superconductors, tunnel junctions, disordered conductors, and so on. In practically all cases, the results have shown a shape of an increasing noise power spectrum as decreasing the frequency $f$. An important feature of 1/f noise is the scale invariance for any frequency or time range, i.e., it looks the same for any chosen frequency or time unit. Due to this reason, it has been considered a wide manifestation of the fractal character of several natural phenomena from physics, biology, neuroscience, and psychology. Moreover, the nonlinear processes can also be considered sources of 1/f noise [35].

1/f noise can be a useful tool in many systems, like graphene, for example. Graphene is a special system in the case of i/f noise because of its linear energy dispersion for electrons and

holes, two-dimensional material nature, and zero-energy bandgap. The conduction electrons have been exposed to charged impurities in a substrate or on its top surface, which lead to strong carrier fluctuations. In the meantime, graphene is similar to a zero-band gap metal, where the mobility fluctuations are due to the charged scattering centers from the surface or the substrate. It also makes a strong contribution to 1/f noise. From the application point of view, due to the symmetry of the electron band structure and wide variation of the carrier density, graphene is used to increase the functionality of amplifiers and phase detectors in communications and signal processing. For this kind of application, 1/f noise is a crucial indication of device performance.

# Chapter 3

# Sample fabrication and techniques

Nowadays, it is feasible to construct heterostructures comprised of different van der Waals materials with atomically sharp interfaces. The technical challenge in the fabrication process is picking up the exfoliated thin materials or monolayer after mechanical exfoliation while avoiding any chemical and mechanical degradation. Here, I review some of the state-of-the-art, deterministic transfer methods of two-dimensional materials. I have used the PPC and PC film transfer techniques to fabricate desired vdw heterostructure. I have also developed gold-assisted exfoliation for TMDs monolayer and several dry-release transfer techniques for stack fabrication during my Ph.D.

At the beginning of my Ph.D., we used only the PPC film dry release transfer technique to fabricate the heterostructure in our group, which works for graphene and hBN heterostructure, but not the other TMDs. During these years, I found the proper condition of the PC film dry transfer method to make different heterostructures. Because the CVD-grown TMDs or exfoliated TMDs have strong adhesion with the substrate, the PPC film dry release transfer technique can not directly pick up the monolayer, but PC film is capable of releasing the monolayer TMDs from the substrate. In addition, I tested the gold layer-assisted exfoliation method so that we are now able to make many different kinds of TMDs with large sizes (>100um) in our lab, such as $WS_2$, $WSe_2$, $MoS_2$, $MoTe_2$, $WTe_2$, etc. In the last year, I've learned the low-temperature dry transfer method with PCL film that can be used in some temperature-sensitive materials. In my Ph.D. career, I helped many Ph.D. students, postdocs, and researchers to fabricate their desired heterostructure and devices by all these methods. Of course, I also developed a few side projects through these methods.

## 3.1 Mechanical exfoliation of Graphene

The first monolayer graphene flake in the real world was exfoliated simply by applying the 3M scotch tape to the surface of HOPG (Highly Ordered Pyrolytic Graphite) in 2004 [1]. The main idea of mechanical exfoliation is the separation of graphene layers from the bulk HOPG. For the separation process, the ideal case is that graphene has been peeled from the bulk graphite layer by layer. The van der Waals attraction is the force that needs to be overcome between two adjoining graphene layers. How to overcome the van der Waals attraction force to separate the monolayer is more or less a mechanical question. The procedure is presented in Figure 3.1.1.

First, the Scotch tape is applied to the HOPG surface and thus exerts a force on the surface. Then, by repeating this step numerous times, the bulk graphite layer will become thinner and eventually down to a single layer of graphene. This method produces high-quality and large-sized graphene flakes. Using the graphene samples prepared by this method, many outstanding properties of graphene have been discovered.

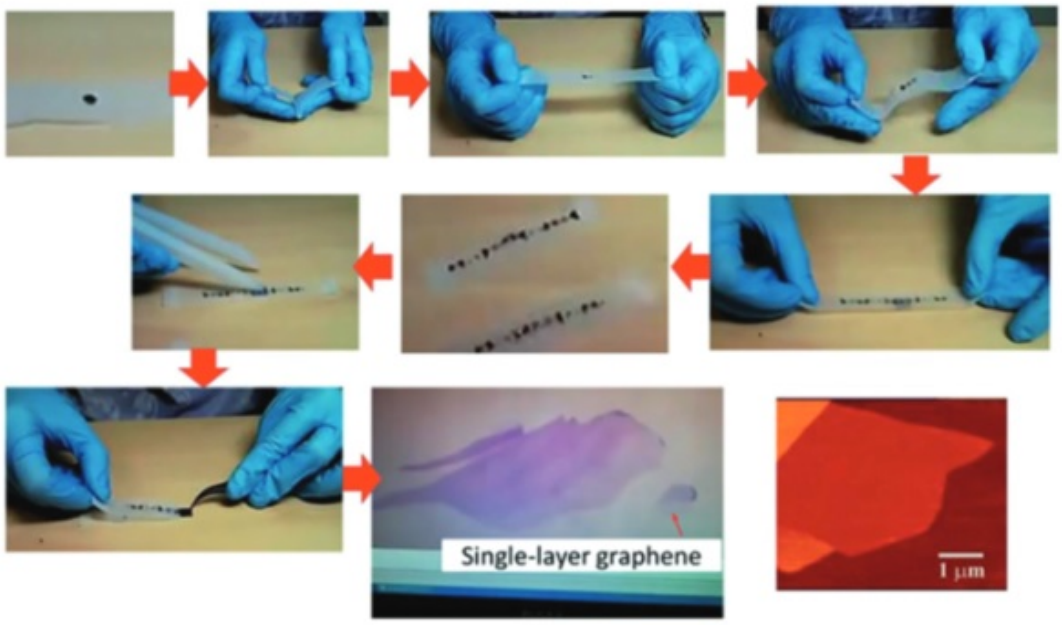


Fig. 3.1.1 An illustration procedure of the Scotch-tape-based micromechanical cleavage of HOPG [79].

## 3.2 Gold-assisted exfoliation of Transition-metal dichalcogenides

Transition-metal dichalcogenides (TMDCs) are a class of layered materials similar to graphene, which also show unique electrical, mechanical, and optical properties as a potential platform for future applications. The layers of these materials are kept together by weak van der Waals (vdW) forces, leading to the possibility of cleaving down to a monolayer using the mechanical exfoliation process.

While mechanical exfoliation used to suffer from low yields and rather small sizes of the exfoliated flakes, many-layered materials can't be exfoliated into monolayers by present exfoliation ways. Simple improvements like exfoliating the materials on a hot plate give a slight increase in the flake size [80]. The Universal Au-assisted mechanical exfoliation method has proven its effectiveness on almost 40 types of single-crystalline monolayers [81]. These results show that exfoliation assisted through an Au adhesion layer with covalent-like quasi-bonding to a layered crystal can generate large-area monolayers of TMDCs. This method is quite useful, especially when layered crystals are difficult to exfoliate using conventional methods. The entire Au-assisted exfoliation process is illustrated in Figure 3.2.1.

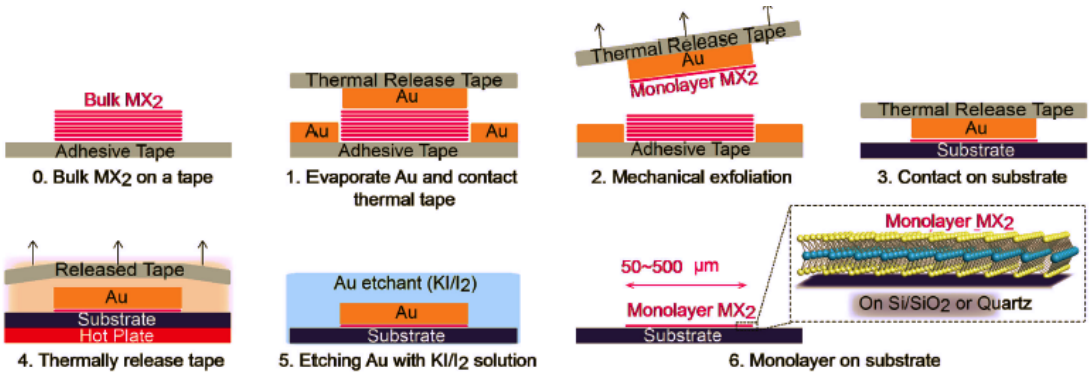


Fig. 3.2.1 Schematic illustration of the Au exfoliation process [82].

In the beginning, a 100nm gold layer is evaporated by physical vapor deposition onto bulk $MX_2$ (M = Mo or W; X = S or Se) crystals attached to the scotch tape. The main idea is that the interaction of the topmost $MX_2$ layer with the gold layer is stronger than the van der Waals force of that same layer with the bottom layers of $MX_2$. The topmost layer attached by the thermal release tape makes it the possibility to only peel off the topmost layer. The thermal release then transfers the Au and single $MX_2$ layers to the target silicon substrate ($SiO_2$ /Si), and the substrate is then treated with an oxygen plasma cleaning method to clean

the surface of the substrate. Afterward, the thermal tape can be released by keeping it on a hot plate. (130 °C), gold layer and $MX_2$ remaining on the substrate. The gold film is etched using a gold etchant (potassium iodide and iodine, 1:4:40 $I_2$/KI/DI water) for 5 mins, which selectively etches the Au while not etching the TMDCs flakes. The final step is soaking the substrate in acetone and isopropyl alcohol (IPA) for 10mins to remove any residues and acquire the large-area monolayers.

The result shows that it is a reliable way to obtain monolayer TMDCs in Figure 3.2.2. In this work, tungsten disulfide monolayer($WS_2$) was made by Au-assisted exfoliation. I have found that other TMDCs, such as $MoS_2$, $WSe_2$, $MoTe_2$, and $WTe_2$, can also be obtained in the form of monolayers with large sizes. Note that the monolayers remain on a clean surface and without residue after removing the gold layer by the gold etchant.

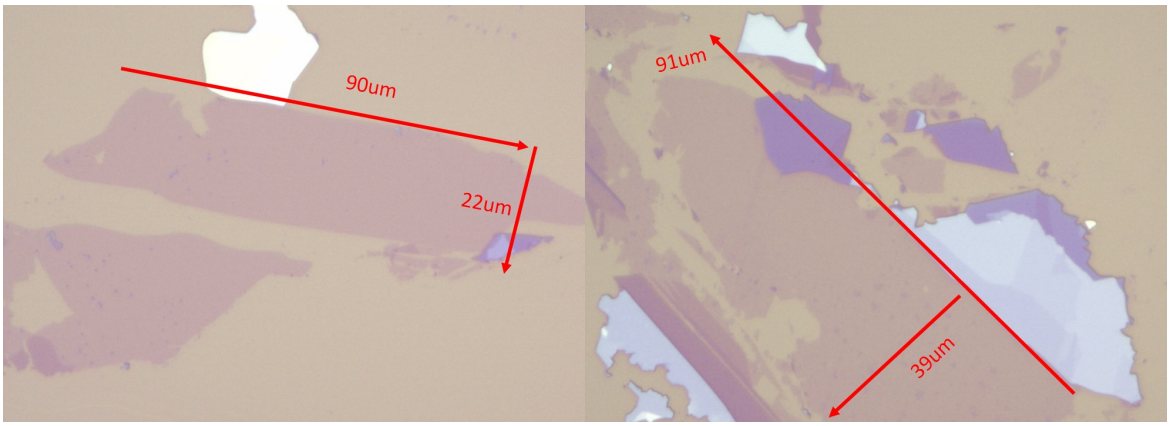


Fig. 3.2.2 Au-assisted exfoliation result of the two different tungsten disulfide ($WS_2$) monolayers with large size.

## 3.3 Dry release transfer: Polydimethylsiloxane (PDMS)

Once we have obtained the two-dimensional target material on the silicon substrate by exfoliation, the simplest way to make heterostructures or stacking of two-dimensional materials is by polydimethylsiloxane (PDMS) stamping. The transfer process of two-dimensional material plays a crucial step in the fabrication of heterostructures based on the artificial stacking of two-dimensional materials. In addition, precisely positioning the landing of the flake helps the integration of the material into devices, which facilitates the investigation of innovative applications and the discovery of new phenomena in the target material. For example, we can first prepare the device, such as a transistor, Josephson junction, or a SQUID device, then land the target material on the devices.

In order to make heterostructures or coupled two-dimensional materials with different devices, polydimethylsiloxane (PDMS) stamping, the all-dry transfer method through viscoelastic stamps, can be a reliable way. There are no capillary forces involved in the process [83]. And also, the fabrication process is fast and efficient, and it can be achieved with successful high reproducibility.

The transfer process, shown in Figure 3.3.1, relies on the viscoelastic properties of PDMS. In the beginning, a flake exfoliated onto a commercially available viscoelastic PDMS stamp with scotch tape. The PDMS stamp is attached to a glass slide that is connected to a manipulator. Then, the flake on the PDMS can be aligned precisely with the target substrate through the optical microscope, bringing the two in contact after aligning the material with the substrate. In order to release the flake from the PDMS stamp, the glass slide has to be lifted slowly, making sure that the PDMS can detach very gently. The flake then lies on the target location on the substrate.

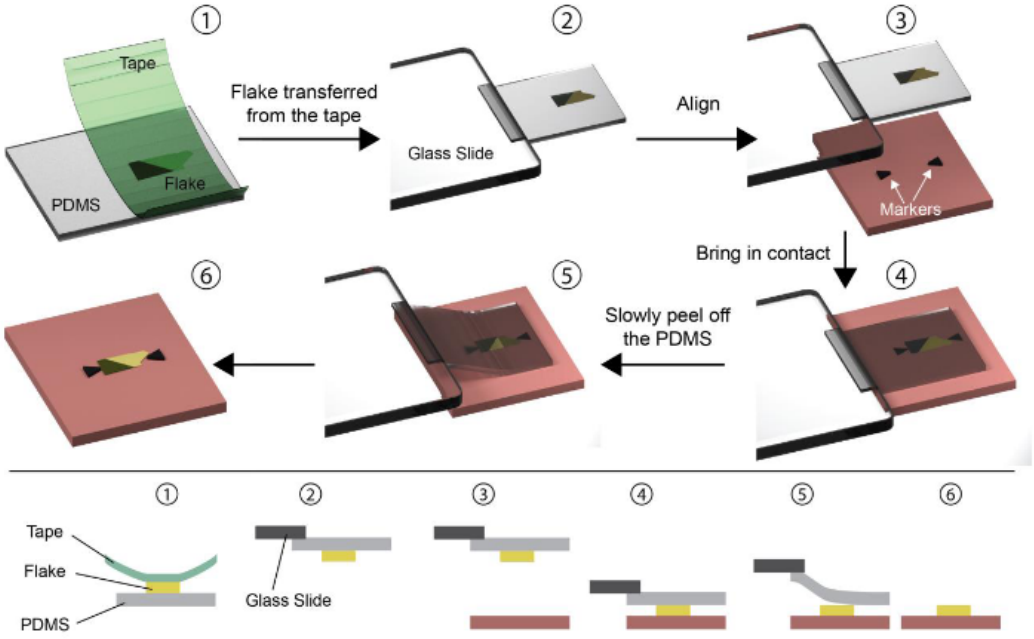


Fig. 3.3.1 The PDMS dry transfer method. (1) The flake to be transferred is exfoliated onto a PDMS stamp (2), and the stamp is then attached to a glass slide connected to a micromanipulator (3). The flake can be aligned with the final substrate by a microscope (4), and brought in contact (5). By slowly peeling off the PDMS stamp (6), the flake can be deposited on the substrate [12]

Figure 3.3.2 (a) shows the thin flake stamp on the prepared device. One can even first drop the target material onto the prepared device, then stamp hBN on top of the target material as the protection layer. The 3.3.2 (b) displays the flake before and after stamping on the silicon substrate. Sometimes during the stamping process, the thin layer or monolayer of material breaks into several pieces due to the strain from the PDMS block.

(a)

(b)

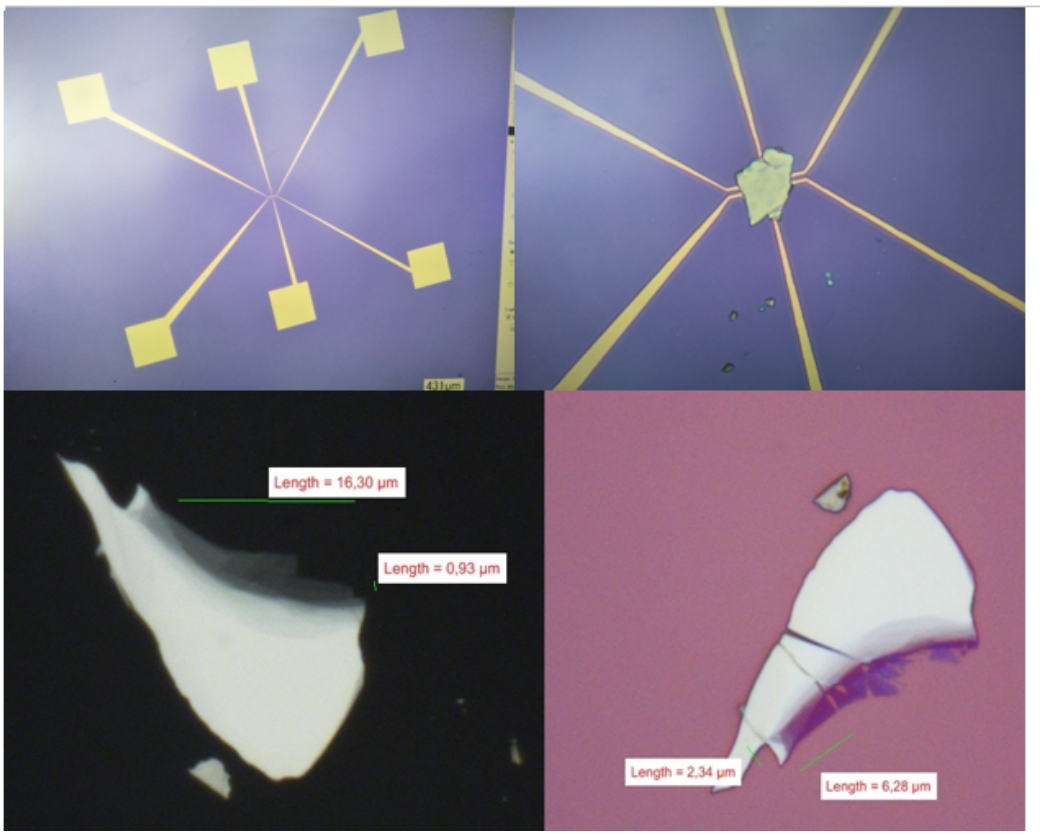


Fig. 3.3.2 (a) The prepared device before and after dropping the thin-film flake on the device. (b) The exfoliated flake with different thicknesses before and after dropping on the silicon substrate.

## 3.4 Dry release transfer: polypropylene carbonate(PPC) film

The stacking of a few single two-dimensional materials to form the heterostructures is required to construct the layered stack with the desired properties. But the main problem of the fabrication process is the cleanliness of the interfaces between the different two-dimensional materials, which will have an impact on device performance. Clean interfaces between two-dimensional materials lead to a better performance of the device [13] [84]. The contaminants that exist between layers tend to gather together into 'blisters,' resulting in the deterioration of the transport properties [85].

The PPC dry transfer technique has been demonstrated to be a rapid and clean fabrication procedure for van der Waals heterostructures in an ambient atmosphere [86]. The blisters of trapped contamination between the layers are observed in several samples [86], but it can be totally eliminated by stacking individual monolayers into van der Waals heterostructures at temperatures of 110°C.

The flakes can be repeatedly picked up or dropped down at the desired positions when the temperature is above the glass transition temperature of the PPC polymer. By using the oxygen plasma treatment of the PDMS before attaching the PPC film to the PDMS, the adhesion force can be increased between the PPC and the PDMS, and so avoid the delamination at higher temperatures.

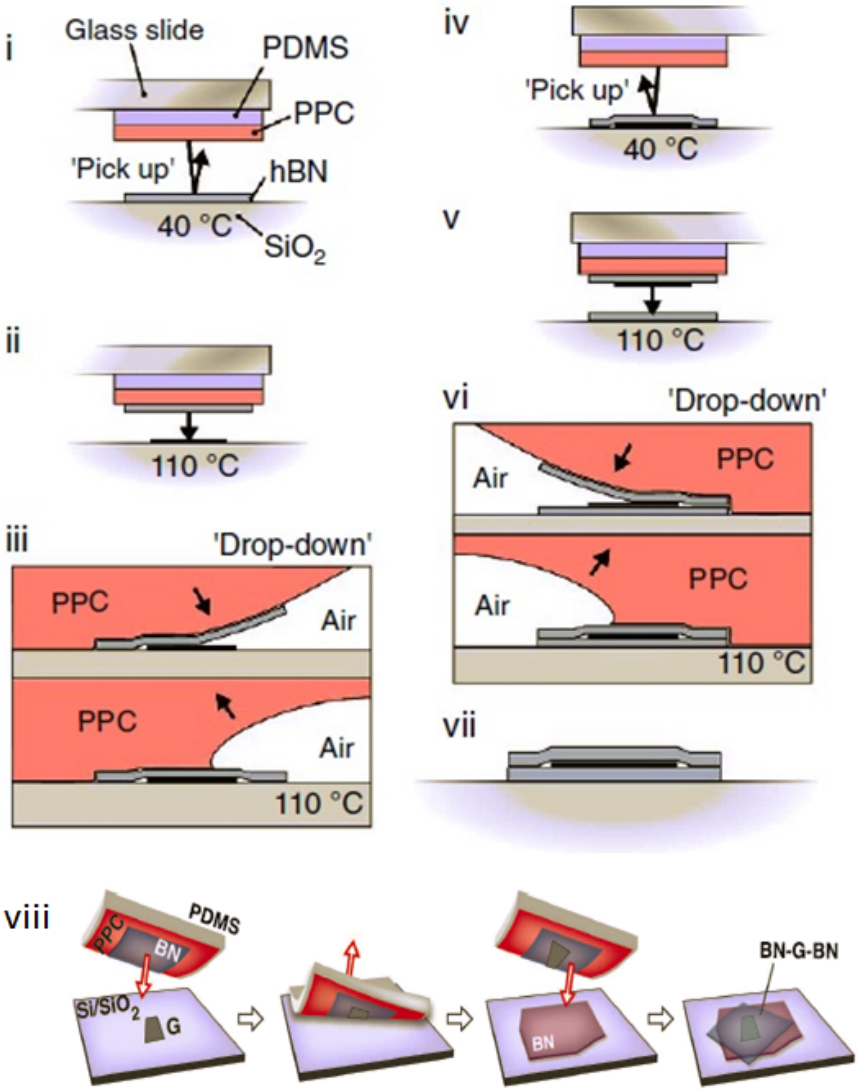


Fig. 3.4.1 Schematic process flow for assembly of 2D heterostructures by pick-up and drop-down [13][86].

Figure 3.4.1 shows the flow process of making heterostructures with the PPC film. Before the transfer process, we need to prepare the PPC film by spin coating. In this case, first, we put one drop of PPC solution on the silicon substrate at 2000rpm for 1 min. After that, keep it on the hot plate at 90∘C for 1 min, then the PPC film is ready. The way to transfer the PPC film on top of PDMS is by making a hole in the scotch tape. Afterward, by attaching the scotch tape to the PPC film, we can recapture the PPC film after separating the PPC from the silicon substrate and transfer it to PDMS, shown in Figure 3.4.1 (i).

Figure 3.4.2 is an example of the transfer process. Figure 3.4.2 (a)(b)(c) are the top-BN, bottom-BN, and graphene before the transfer process onto the silicon substrate. The first step to make the heterostructure is picking up the top hexagonal boron nitride (hBN) at 40°C. In the beginning, we attach the PPC film to the substrate to form a small touching point, then heat up the temperature to 40 °C. The PPC touching point will expand during the heating process, and the film will entirely cover the BN flake in the end. The BN flake can be lifted from the substrate to the PPC film during the cooling process until cooling to room temperature 25 °C. A temperature of 40°C is sufficient to separate hBN from $SiO_2$ substrates by using the PPC/PDMS block. It is important to mention that a plasma pretreatment on hBN favors the PPC film lifting the hBN. Figure 3.4.2 (e) shows how the top-hBN succeeds to pick up the graphene at 40°C. Afterward, we continually repeat the heating and cooling steps to pick up the bottom hBN.

shows how to drop the top BN/Graphene/BN sandwich on the prepared device when the temperature is above 110°C. Is it possible to control the landing location of the stack on the substrate or on the prepared device? The top hBN stays on the substrate when we detach the PPC film/PDMS/glass slide from the substrate. In this device, we first prepared a graphite flake that connected electrodes as the back gate, the red circle in Figure 3.4.2 (h). Figure 3.4.2 (h) also demonstrates the stack can be precisely located at the position we want. Using the reactive ion etching, we can etch through the top BN and then make the electrodes connect with the resonator after lithography.

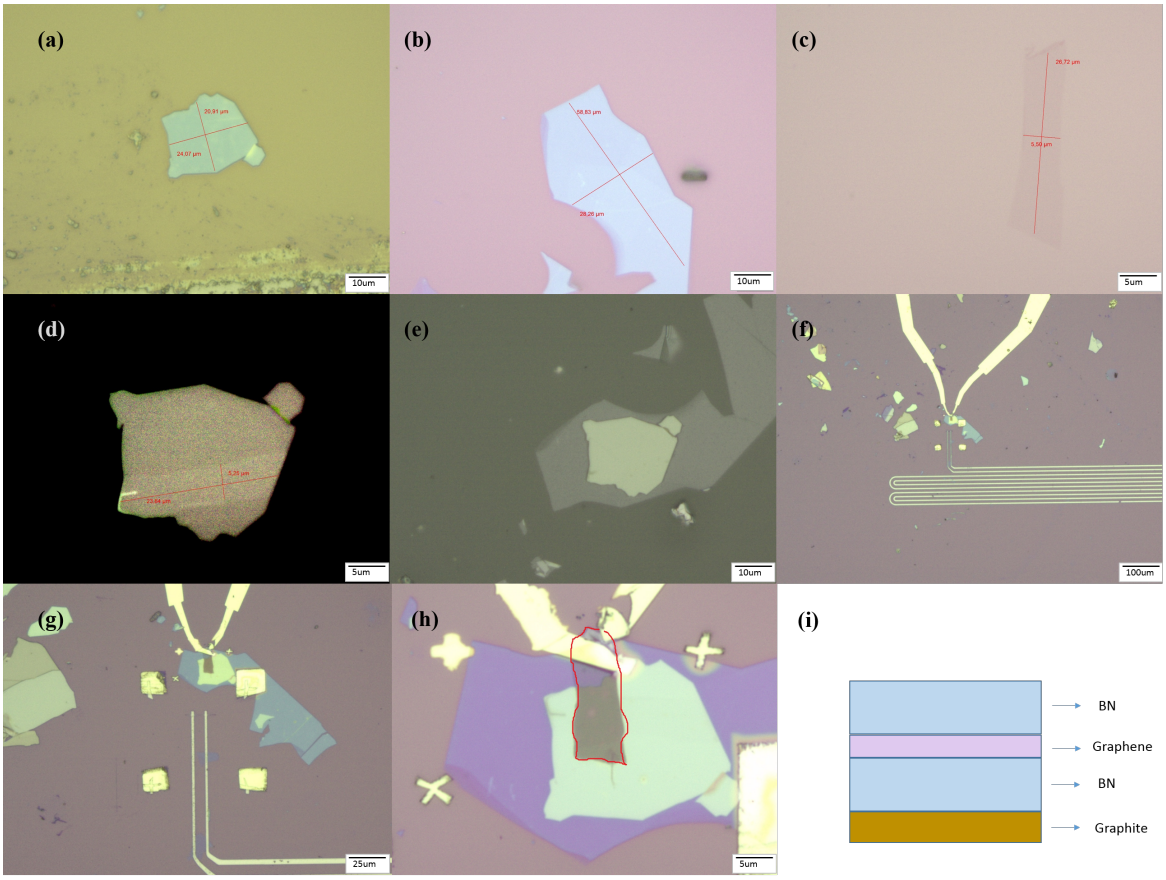


Fig. 3.4.2 (a)(b) are top-hBN and bottom hBN on silicon substrate before transfer. (c) The monolayer graphene. (d) The image shows the top BN succeeded in picking up monolayer graphene, then took a photo with an optical microscope. (e) The photo of BN/Graphene/BN (f)(g)(h) The stack succeed in dropping on the graphite back gate, as the red circle in (h). (i) Stack structure in the end.

## 3.5 Dry release transfer: polycarbonate(PC) film

Even though the PPC film is a useful technique to fabricate boron nitride encapsulated graphene heterostructures, it is hard to pick up some of the other two-dimensional materials, such as CVD-grown $WS_2$, $MoS_2$, etc. In order to couple graphene with TMDCs, polycarbonate(PC) films have been used to fabricate graphene/TMDCs heterostructure in our work. The PC dry transfer process can also remove blisters from fully formed heterostructures [14]. The PC dry transfer method also enables the heterostructure interfaces to be cleaned simultaneously. The interfaces in other techniques need to be cleaned sequentially [13]. Furthermore, this cleaning method also allows heterostructures based on different two-dimensional materials, such as hBN/$MoS_2$ and hBN/Graphene/$MoS_2$ [14].

In the beginning, a PC film is prepared by drop-casting a solution in chloroform (5 % weight percentage of polycarbonate crystal on chloroform solvent) on a glass slide. Then, the second glass slide is used to squeeze and spread the PC solution between the two slides. The slides have to be immediately slipped apart and remaining it on the glass slide to enable the chloroform to evaporate. After the drying process, the PC film is ready to be picked up and mounted onto the PDMS. A detailed description of the PC film preparation is shown in Figure 3.5.1.

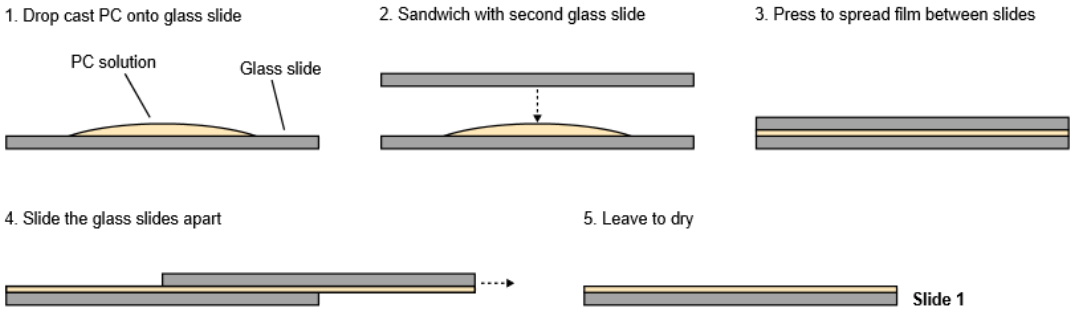


Fig. 3.5.1 The preparation of PC film [14]

The process starts by placing the PC film carefully to attach the target hBN flake, then lifting the glass slide while maintaining the substrate at 40°C, Figure 3.5.2 (a). This chosen temperature allows the PC film to pick both hBN and graphene flakes with an almost 100 % success rate, and it would be lower at room temperature. The hBN sticks to the PC film and is removed from the $SiO_2$/Si substrate when the stamp is lifted, Figure 3.5.2 (b). Then we can control the position of hBN to a chosen graphene flake and place the two flakes in contact, Figure 3.5.2 (c), again at 40°C. In this step, it is possible to choose the clean area on the graphene flake because only the contact area of graphene with hBN will be picked up due to the preferential adhesion of graphene to hBN. Again, we repeat the same process to pick up the bottom hBN in Figure 3.5.2 (e),(f). The heterostructure hBN/Graphene/hBN is now attached to the PC film

For the purpose of dropping the stack onto the substrate, the stage temperature is heated up to 180 °C, and then we bring the stamp into contact with the substrate, Figure 3.5.2 (g). At 180 °C, the PC film is above the glass transition Tg 150°C [87], bringing about a decreased viscosity, allowing the stack to remain on the substrate, as seen in Figure 3.5.2 (h),(i).

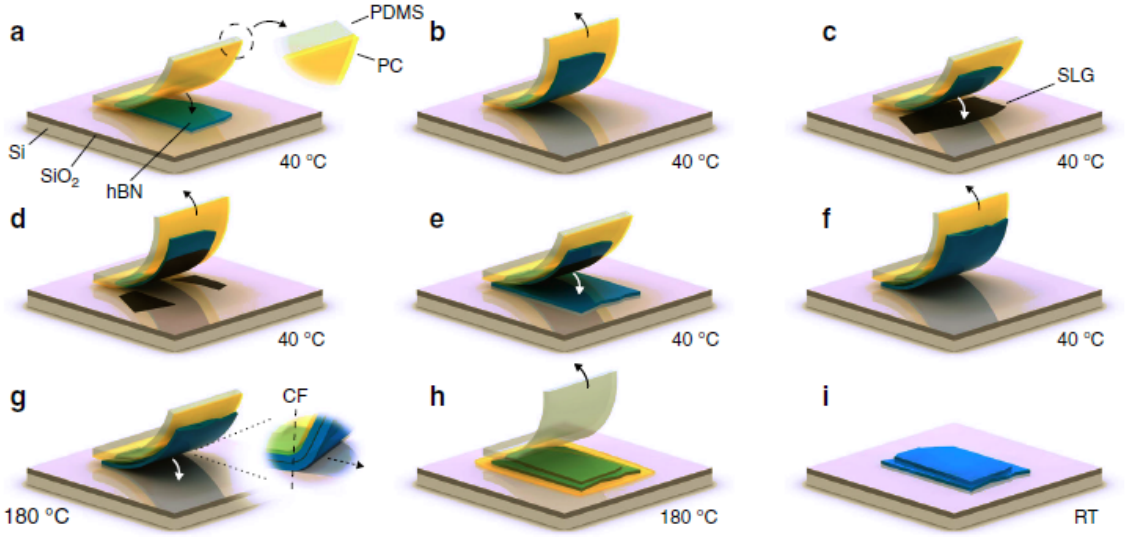


Fig. 3.5.2 Scheme of the PC cleaning dry transfer process [14].

The advantage of the PC film is that it is possible to directly lift the monolayer graphene or TMDs from the substrate. The PPC film can only pick up hBN from the substrate, but not monolayer graphene or other TMDs. In this case, for example, if we want to make a simple heterostructure such as a graphene/$WS_2$ stack, we can simply pick up monolayer graphene and then drop it onto the monolayer $WS_2$. PC dry-release transfer is an easy way to couple graphene with other TMDs with a very high success rate. Figure 3.5.3 shows a simple stack we often made. Figure 3.5.3 (a) and (b) are monolayer graphene and $WS_2$. We can easily lift monolayer graphene from the substrate by heating the PC film above 120°C, then drop the graphene flake onto the WS2 by increasing the temperature to 170°C. After that, the substrate was soaked in chloroform solvent for 20mins to remove the PC film on the graphene/$WS_2$.

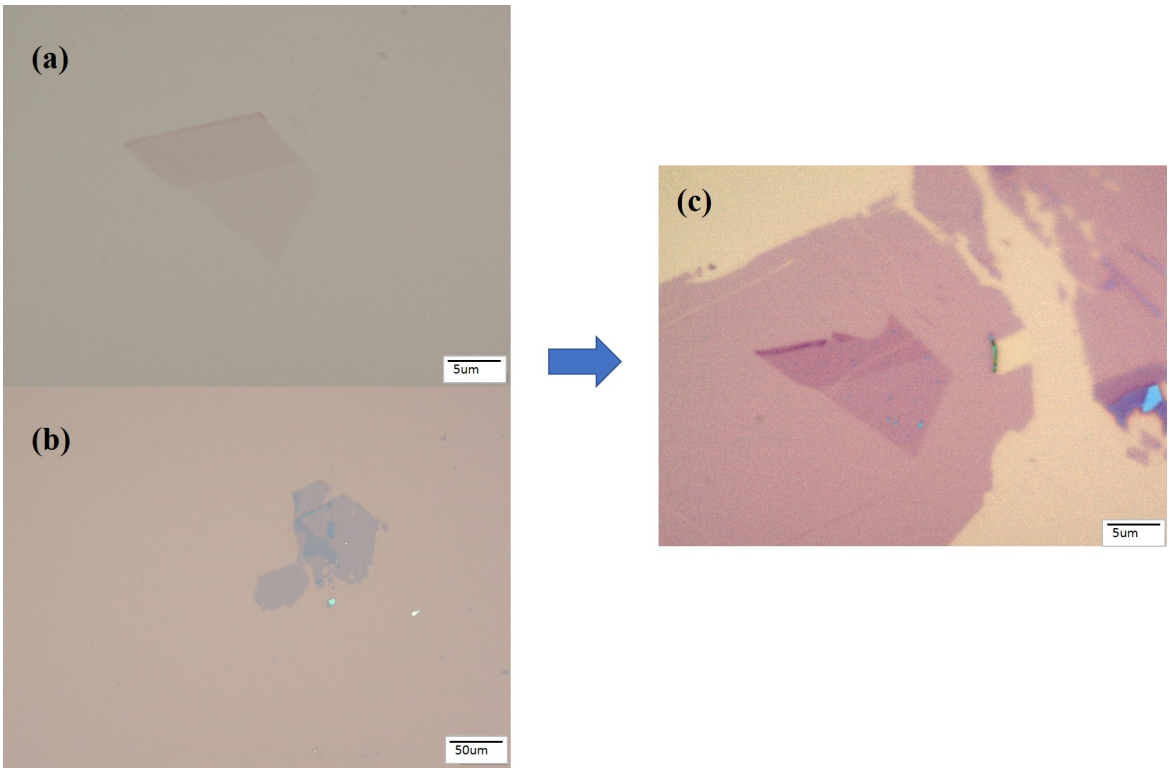


Fig. 3.5.3 (a) and (b) are graphene monolayer and $WS_2$ monolayer, respectively. (c) The graphene is coupled with the $WS_2$ monolayer by the PC transfer method.

## 3.6 Dry release transfer: polycaprolactone (PCL)

The main advantage of PCL film is avoiding the temperature effect from heating during the fabrication process because the dropping down the temperature is only 65°C. I tried this method to help the another Ph.D. student in our group. In his case, he is working on a temperature-sensitive material, a topological insulator BiBr, which degrades when the temperature is higher than 120°C. Therefore, in this kind of material, we can first prepare a designed device and then use the low-temperature transfer method to land the target material on the device in order to prevent degradation or phase transition.

The PCL stamp was prepared in the following steps, which are similar to the reference [88]. First, the polycaprolactone (Sigma Aldrich, average Mn: 80 000) was dissolved in a tetrahydrofuran (THF) solvent. The mass percent of the mixture was% PCL in THF. Afterward, I kept the mixture in the magnetic stirrer for more than seven days until it completely dissolved. The dissolved solution formed a viscous and transparent liquid. After I got the mixture, I used a similar way to prepare the PCL film as the Figure 3.5.1. In the Pick-up and drop-down of vdW flakes, I first tried the same pick-up and drop-down conditions as the reference, but the success rate was very low (20%). In the meantime, the monolayer became many pieces after the pick-up process due to the strong adhesion of PCL film. The reference [88] shows the same consequence as in my test. Thus, I found that if I kept the temperature lower than 52-55 °C in the pick-up process, the PCL film would not turn liquid state and could still pick up monolayer TMDs. At this pick-up temperature, the monolayer remains an intact slice and still be able to pick up the monolayer. In the end, we can drop the stack or monolayer at 65°C onto the prepared device. By this method, we can avoid the degradation at high temperatures in the transfer process or in the lithography process, which is useful for our group members who are working on topological insulator BiBr (<120°C) or perovskite 2D material $MAPbI_3$ (<85°C).

## 3.7 Deposition of molecular layers: by molecule beam epitaxy and drop-casting

**Molecule Beam Epitaxy**

Molecule Beam Epitaxy (MBE) is widely used in the manufacture of molecular layers on substrates or devices. The fundamental information about MBE will be presented in this section, which includes the basic description of the Ultra-High Vacuum (UHV) environment. There are many books in the literature that explain in more detail the technical information [89][90].

Most thin-film deposition techniques demand a clean environment with high vacuum pressures from $10^{-9}$ Torr. MBE is a technique that requires an even better vacuum. Typically, the base pressure in the growth reactor before starting the deposition process needs to be $10^{-10}$ to $10^{-11}$ Torr range. The key reason for the demand for ultra-low pressure is the high quality of MBE-grown films. $10^{-9}$ Torr is a normal limit value for the necessary pressure because the mean free path has to be larger than the distance between the substrate and the beam sources. This value of pressure is the basic demand and is not sufficient. Actually, the main reason for a UHV MBE environment relates to the contamination of the target molecules that ensure the high purity of the film. The duration of the deposition of one monolayer can be described as the partial pressure through the definition of the flux (number of molecules that hit the surface per unit area in a few seconds):

$$\omega_i = \rho_i \sqrt{\frac{N_A}{2\pi \kappa_B M_i B}} \tag{3.7.1}$$

The $\omega_i$ is the flux of species $i$, $\rho_i$ is the partial pressure of the species $i$, and $M_i$ is the molar mass of the species $i$. $N_A$ and $\kappa_B$ are Avogadro and Boltzmann constants. For example, by using typical growth rates for GaAs through MBE, the maximum pressure of the residual gases in the vacuum reactor is about $10^{-11}$Torr. That means the deposition process can only proceed in a highly efficient UHV environment.

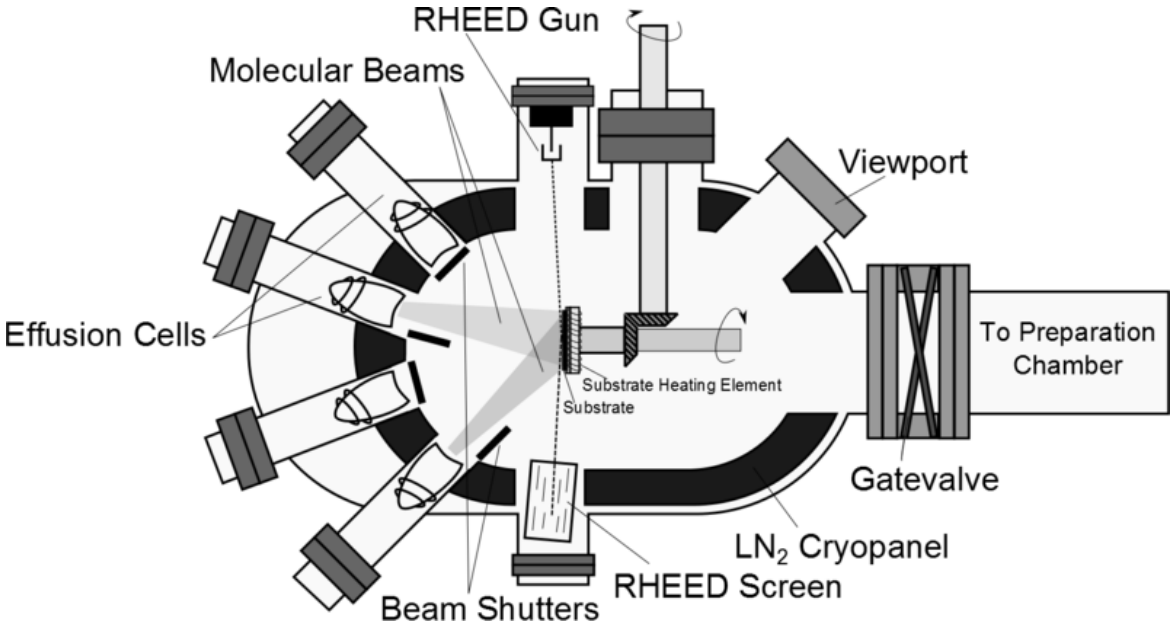


Fig. 3.7.1 Sketch of the growth module of an MBE system. Source:[91].

The substrate manipulator and source cells are the important parts of the growth module, as shown in Figure 3.7.1. Before mounting the substrate for the MBE deposition process, it is important that the substrate heater and the source cells are heated above the growth temperature to degas all the remaining contaminants adsorbed on the surface. After the degassing process, the substrate manipulator and effusion cells are then cooled down to the operating temperatures. Of course, the molecular sources have been checked before loading the substrate into the chamber. The prime sources in MBE are thermal effusion cells directly mounted in the growth chamber, and desired evaporation rate can be achieved by increasing the cell temperature, which directly affects the molecular flux. After the preparation work, the substrate can transfer to the sample holder in the chamber. The substrate temperature is one of the crucial parameters during growth. Then, by controlling the shutters in the cells where containing the desired material, the deposition can proceed.

### Drop-casting method

Drop casting is a basic, simple, and low-cost method for the deposition of molecular layers, see Figure 3.7.2. This method has been used for the formation of small coatings on limited surfaces, and it needs only a very small amount of solvent. This technique is similar to spin coating, but the main difference is that no substrate spinning is required. And the drop is poured on the substrate or device and allowed to dry out without spreading. The film thickness and properties only depend on the volume of the solution dispersion and concentration. Other factors which affect the film structure are the rate of evaporation and the drying process. The films formed using this method used to be non-uniform due to inconsistent drying conditions and uneasy control. The formed films are thicker at the center and thinner at the edges. In this kind of method, volatile solvents are normally preferred, which can well wet the substrate.

One of the advantages of spin coating is less waste of material. But on the other hand, there are several drawbacks of this method, including difficulty in controlling the thickness of the film and non-uniform film formation on substrate or device.

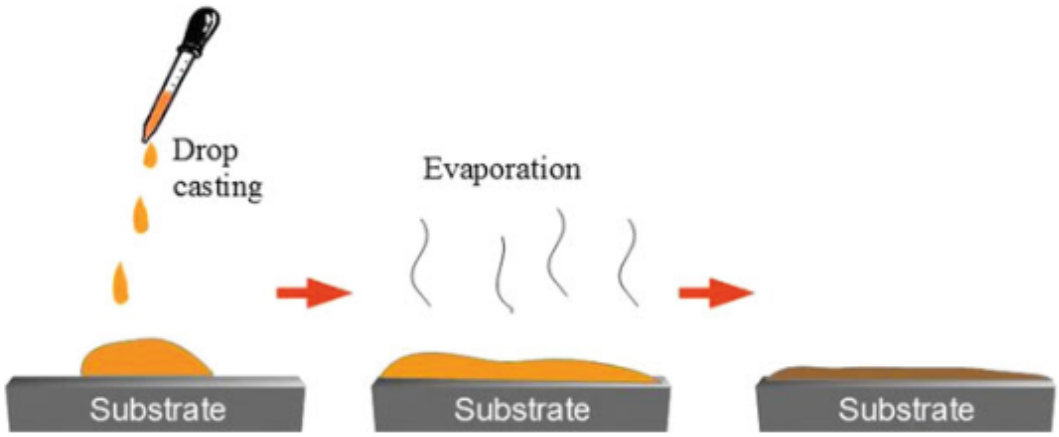


Fig. 3.7.2 Schema of the deposition using the drop-casting method [92].

## 3.8 Device fabrication process

After we got the desired monolayer or heterostructure, we used electron beam lithography, reactive etching, and physical vapor deposition to create a device on the monolayer or heterostructure. This section goes over the fabrication of the device step by step. Note that what is presented here is a general overview of the steps involved and the challenges that we faced in the process.

The main tool in the fabrication is electron beam lithography. Electron beam lithography (e-beam lithography) is a technique that uses an accelerated beam of electrons to pattern the designed device on substrates that have been coated with an electron beam sensitive, positive resist. When the electron beam spot on the resist, the solubility of the resist changes, enabling selective removal of exposed regions of the resist by immersing the sample in a developer. In our lab, we have a spin coater and two types of positive resist, PMMA, and CSAR, as seen in Figure 3.8.1 (a). Normally, we used PMMA resist in the fabrication of ohmic contacts (Ti/Au) and CSAR resist for the superconducting contact because CSAR is better adapted to sputtered contacts, such as the deposition of superconducting Molybdenum Rhenium alloy (MoRe). After the spin coating, we can draw a designed pattern on the resist, precisely on the monolayer or heterostructure, through an e-beam lithography system, as shown in Figure 3.8.1 (b).The positive resist can be removed by immersing the sample in the developer, then the designed pattern appears. Afterward, in the hBN encapsulated graphene or stack, reactive ion etching is etched through the covered hBN layer in order to reach graphene for making 1D contact. When we have the desired pattern after the developing process, we used the electron beam PVD to deposit Ti/Au contacts on the device, and the DC sputtering PVD is used in the superconducting contacts Molybdenum Rhenium alloy (MoRe), as seen in the Figure 3.8.1 (d). The final step is removing the unwanted metallic films after deposition by lift-off procedure, immersing the sample with a lift-off solution. If everything goes well, the film deposited on the designed pattern should stay while the film deposited on the resist should be washed away.

When there is only monolayer two-dimensional material or thin heterostructure (< 50nm), the recipes that we used are shown in Figure 3.8.3 No.1 and No.2. However, when the thickness of van der Waals heterostructure is higher than 50nm, cracks appear after immersing the sample in the developer, and can lead to short circuit problems, seen in the Figure 3.8.2. The cracks are probably caused by the strain inside the resist due to the height of the van der Waals heterostructure. Therefore, I developed three recipes to eliminate the cracks problem, seen in Figure 3.8.3 recipes 3, 4, and 5. By the increase of the thickness of the resist as recipe 3, three layers PMMA, we can avoid the cracks after developing the process at room temperature. Or, we keep the developer in the refrigerator and immerse the sample

in low-temperature developer after e-beam lithography. Both methods can well eliminate the crack problem after removing the resist in the developer. The schematic process of dry transfer and device fabrication can be seen step by step in section 3.9.2.


Fig. 3.8.1 (a) Spin Coater. (b) Lithography system. Scanning electron microscope Zeiss Supra55VP. (c) Reactive ion etching system. (d) Electron beam PVD and DC sputtering PVD system.

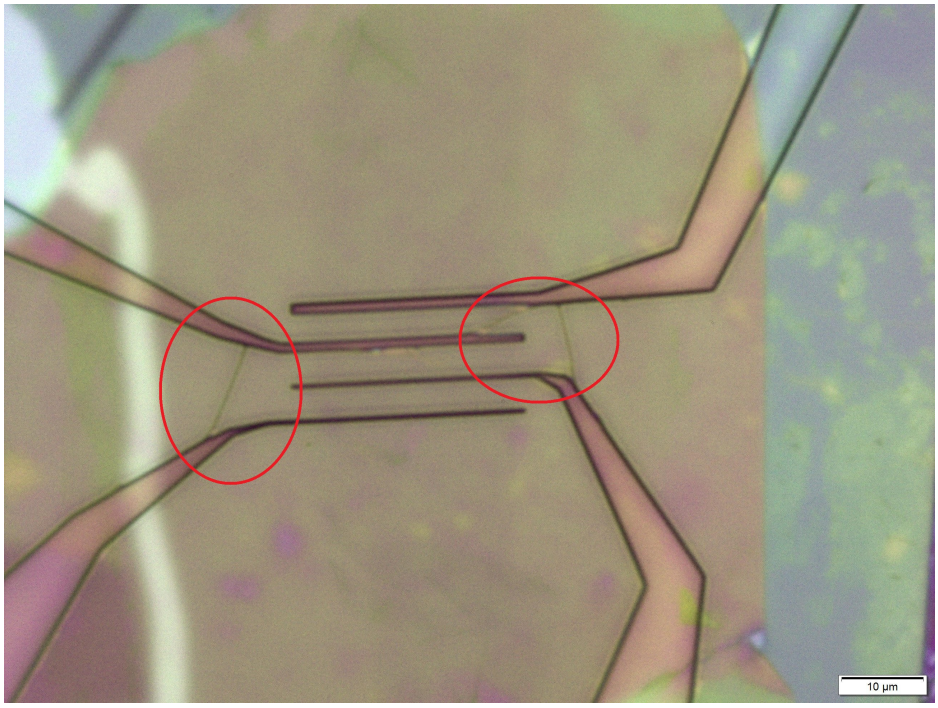


Fig. 3.8.2 The cracks appear after the developing process on the heterostructure due to the strain of the resist. The thickness of the van der Waals heterostructure in the test sample is higher than 300nm.

| | 1. PMMA 950 A6 | 2. CSAR 62 resist | 3. three layers PMMA | 4. PMMA 950 A6 (in the refrigerator) | 5. CSAR 62 resist (in the refrigerator) |
|---|---|---|---|---|---|
| Prebaking | 1 min at 180℃ | 1 min at 180℃ | 1 min at 180℃ | 1 min at 180℃ | 1 min at 180℃ |
| Spin coating | 2000 rpm, 1 min | 4000 rpm, 30s | 1. PMMA A6 495<br>2. PMMA A6 950<br>3. PMMA A6 950<br><br>4000 rpm 60s for each layer | 2000 rpm, 1 min | 4000 rpm, 30s |
| Baking | 1 min at 180℃ | 3 min at 180℃ | 2 min at 180℃ | 1 min at 180℃ | 1 min at 180℃ |
| Area dose | 330 uC/cm^2 | 105 uC/cm^2 | 500 uC/cm^2 | 430 uC/cm^2 | 200 uC/cm^2 |
| Developing solution and time | 45s in MIBK/IPA developer. | 45s in AR 600-546 developer,<br>30s in IPA. | 3s in MIBK/IPA developer. | 50s in IPA/DI water(70%/30%) developer in refrigerator. | 20s in AR 600-546 developer in refrigerator. |
| Lift-off | 1 hr in acetone or DMSO (dimethyl sulfoxide) at 50℃. | 1 hr in 1-3 dioxolane at 50℃. | 1 hr in acetone or DMSO (dimethyl sulfoxide) at 50℃. | 1 hr in acetone or DMSO (dimethyl sulfoxide) at 50℃. | 1 hr in 1-3 dioxolane at 50℃. |
| | | | For thickness of heterostructure > 50nm. | For thickness of heterostructure > 50nm. | For thickness of heterostructure > 50nm. |

Fig. 3.8.3 Recipes of PMMA and CSAR resist used in the e-beam lithography process. Recipes 3, 4, and 5 are used when the thickness of the van der Waals heterostructure is higher than 50nm to prevent the cracks problem, as shown in Figure 3.8.2.

## 3.9 Contribution to other research projects

In my main Ph.D. project, I had to wait for the MBE deposition of the molecular layer on a graphene device in another laboratory. Therefore, I took advantage of my spare time to help other researchers, postdocs, or Ph.D. students in the fabrication of van der Waal heterostructure for their research projects. In general, we started with the fabrication of the target two-dimensional material they needed. Then, depending on the dry transfer methods that I knew, we figured out a reliable method to fabricate the van der Waal heterostructure for them. Either I directly fabricated the stack for them, or I taught them the necessary dry transfer methods for their project. In section 3.9.1, I briefly explain the projects that I participated in during my Ph.D. career. Most pictures in section 3.9.1 were taken during the fabrication process, which didn't appear in the published article. In addition, I add my third project as an example to show how I make stacks and the process of device fabrication in section 3.9.2.

### 3.9.1 Published works

**Substrate influence on transition metal dichalcogenide monolayer exciton absorption linewidth broadening**

This project has been accomplished with Luiz TIZEI, Steffi WOO, and Fuhui SHAO from the Scanning Transmission Electron Microscopes (STEM) group in LPS [93]. An hBN/$WS_2$/hBN sample was deposited onto the holey carbon support TEM grid, and an hBN/$WS_2$ sample deposited onto a 15nm amorphous SiNx windowed TEM grid was made for the STEM group. Both samples also include regions where the TMD is not fully encapsulated by hBN (i.e., regions of freestanding $WS_2$, $WS_2$/hBN, and $WS_2$/SiNx). This provided many substrate configuration combinations to study the effects of hBN and/or SiNx as substrates for TMDs, and how they can influence the exciton absorption linewidths, as measured using electron energy-loss spectroscopy in an electron microscope. In addition, the TMD monolayer roughness was measured using nano-beam electron diffraction, finally demonstrating that monolayer roughness trends directly with the exciton linewidth. However, it is the interfacial cleanliness and substrate-induced charge trapping that contribute the most to linewidth broadening.

I used hBN/$WS_2$ on the $Si_3N_4$ TEM grid sample as an example to demonstrate the transfer process, as seen in Figure 3.9.1. The Figure 3.9.1 (a) and (b) are the thin hBN and CVD-grown monolayer $WS_2$, and (c) is the optical microscope image while picking up $WS_2$

by hBN flake on PC film. Afterward, we dropped the stack on the $Si_3N_4$ TEM grid. How to dop the stack on the fragile TEM grid was an obstacle because we had to immerse the hBN/$WS_2$/$Si_3N_4$ TEM grid into the chloroform solution to remove the PC film in the end, which can lead to losing the stack and breaking the grid. Figure 3.9.1 (f) is the enlarged image of (d), and (f) is the image of the other sample, the hBN/$WS_2$/hBN sample deposited onto the holey carbon support TEM grid.

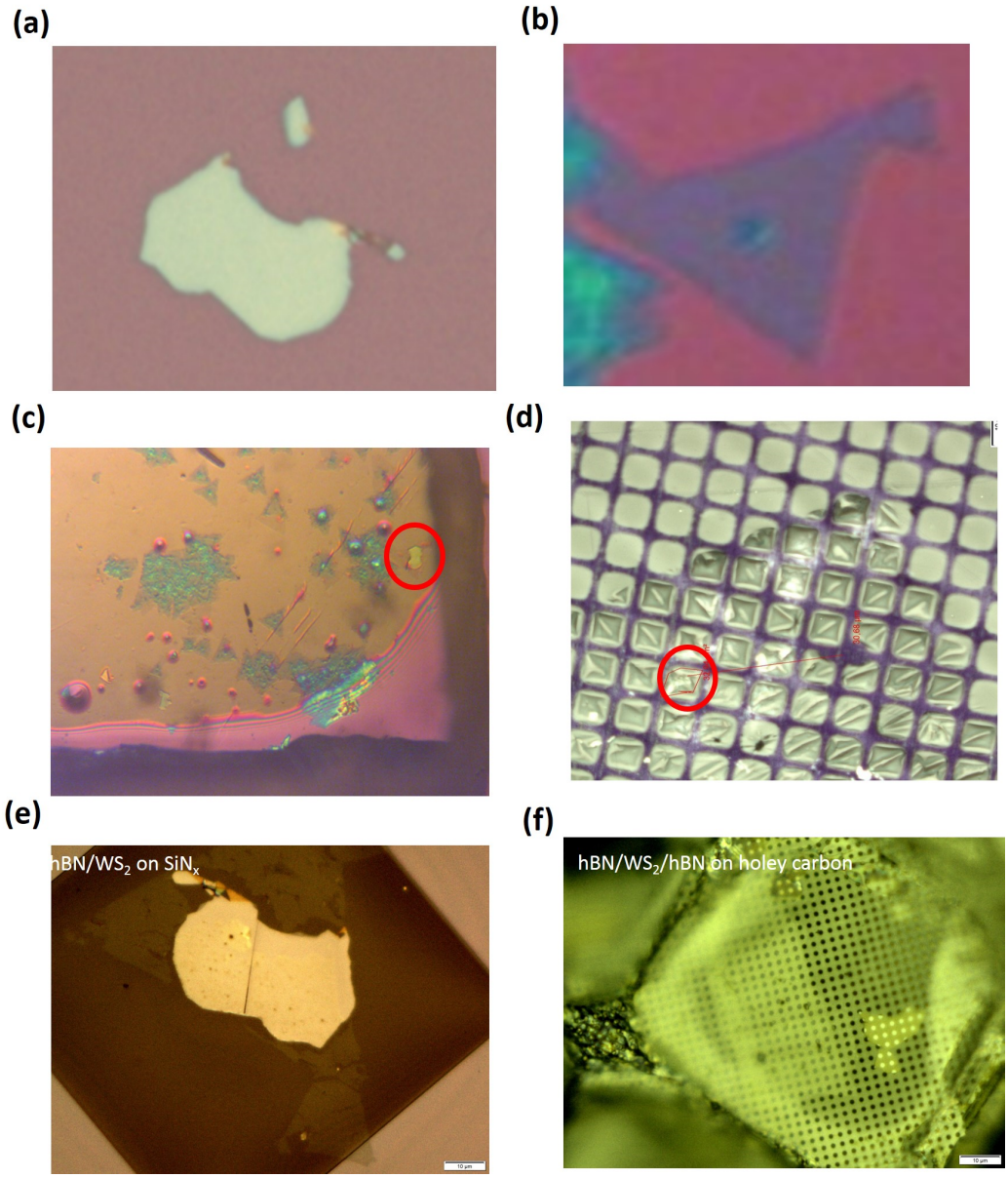


Fig. 3.9.1 (a) Thin hBN made by exfoliation. (b) CVD-grown monolayer $WS_2$. (c) Optical microscope image during pick-up $WS_2$ by hBN. (d) hBN/$WS_2$ drop on the $Si_3N_4$ TEM grid. (e) Enlarged image of (d). (f) The second sample, hBN/$WS_2$/hBN sample deposited onto the holey carbon support TEM grid.

**Detection of graphene's divergent orbital diamagnetism at the Dirac point**

This work has been done with the Ph.D. student, Jorge VALLEJO, in our group and with my supervisor Hélène BOUCHIAT [94]. The main idea of this project is to measure the gate voltage–dependent magnetization of a single graphene monolayer encapsulated between hBN by using a sensitive giant magnetoresistance (GMR) sensor. I was in charge of teaching Jorge how to fabricate monolayer graphene and hBN, as well as the PPC and PC dry transfer techniques, in order to build an hBN-encapsulated graphene stack. Eventually, we succeeded in creating hBN/Graphene/hBN vdw heterostructure, as seen in Figure 3.9.2 (a). In addition, we precisely landed the stack on the location we wanted on the GMR sensor, as shown in Figure 3.9.2 (b). 3.9.2 (b).

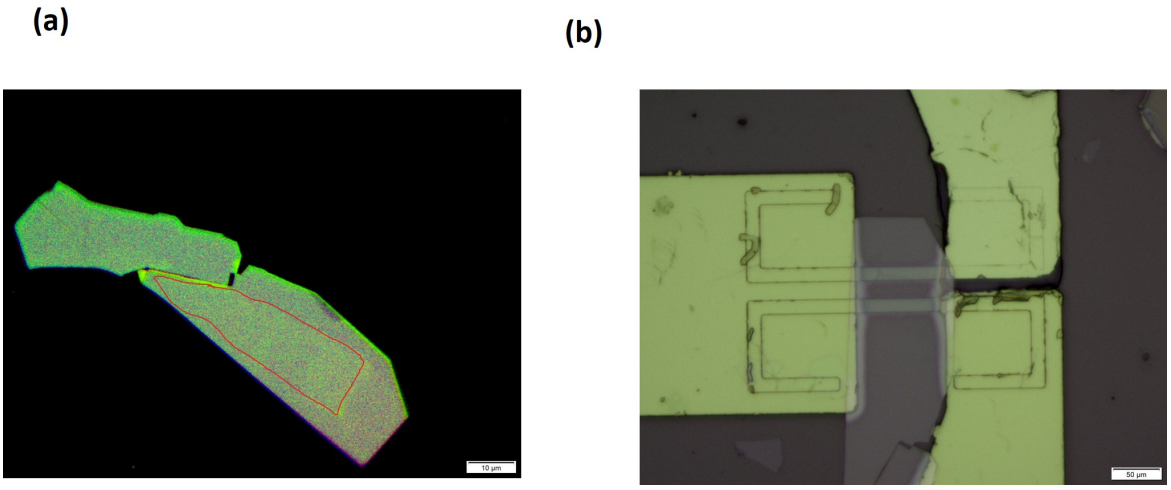


Fig. 3.9.2 (a) hBN/Graphene/hBN heterostructure image in the optical microscope. By changing the contrast of OM, the monolayer graphene can be seen. (b) The hBN-encapsulated graphene precisely lands on the GMR sensor.

**Phase-dependent dissipation and supercurrent of a graphene-superconductor ring under microwave irradiation**

This work was finished with the former postdoc Ziwei DOU and published in 2021 [95]. I made a boron-nitride/graphene/boron-nitride (BN/G/BN) stack for him and dropped it on a superconducting (MoRe) resonator at the location he preferred. Figure 3.9.3 shows the SEM and optical microscope images of the final device.

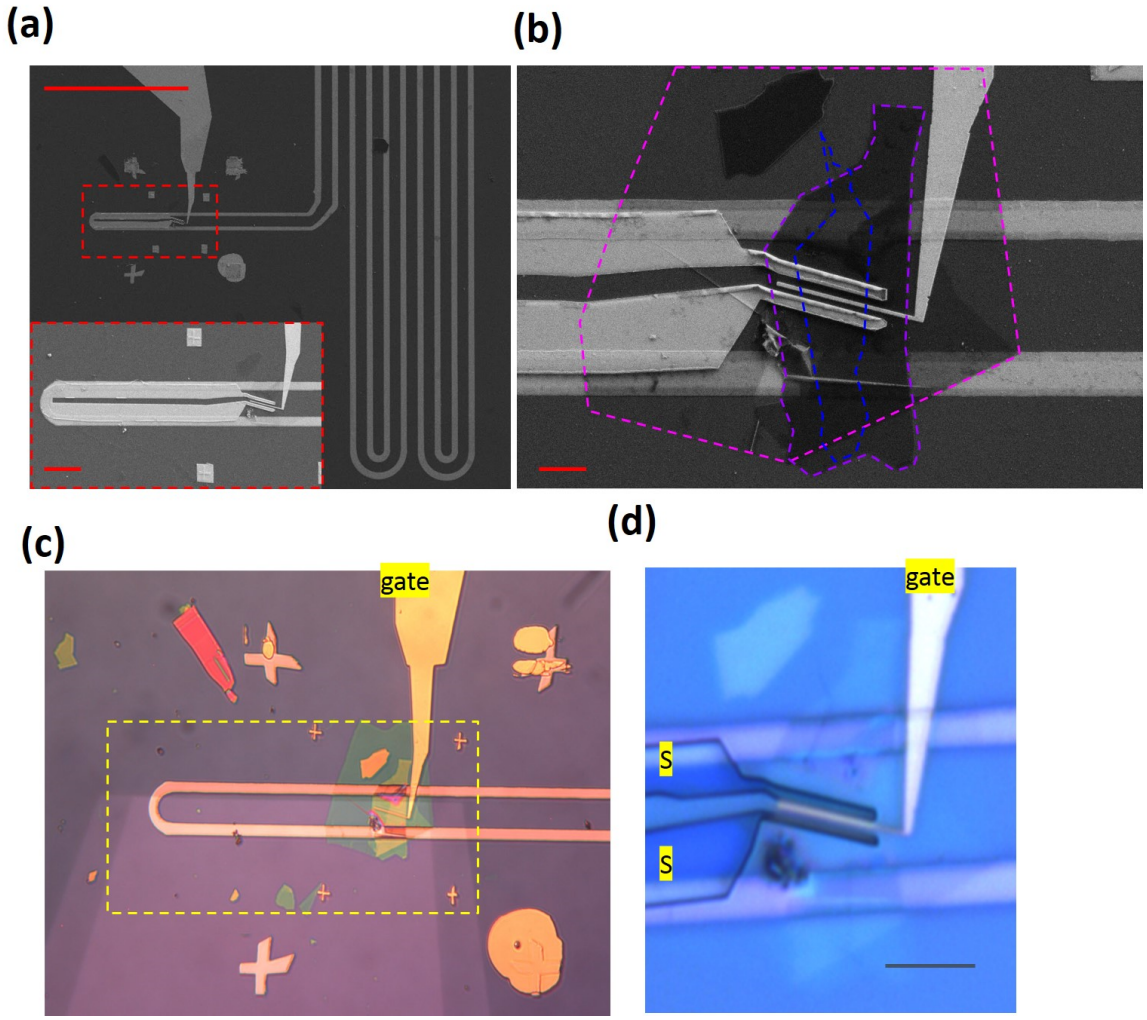


Fig. 3.9.3 (a) SEM images of the section of the MoRe resonator. Scale bar: 100 m. The red box image is the zoomed-in image of the SGS junction. Scale bar: 3 um. (b) Purple and magenta dashed outlines: top and bottom BN. White dashed outline: graphene. (c) and (d) are the optical microscope image in the same area as (a) and (b).

### 3.9.2 Ongoing projects

**Edge state of spin-orbit induced band inversion in $WS_2$ encapsulated bilayer graphene via proximity effect**

In this section, I use an unfinished project of mine to describe the stacking process of vdw heterostructure and the process of device fabrication, which are related to many tools that I mentioned in the previous sections. Figure 3.9.4 (a) (a) shows the Sketch of the structure of the stack in this project, and (b), (c), (d) are bilayer graphene, monolayer top $WS_2$, and monolayer bottom $WS_2$. The bilayer graphene was made by exfoliation. The monolayer $WS_2$ was obtained by the Au-assisted exfoliation, and the size of monolayer $WS_2$ is bigger than 50um, which eases the fabrication of the vdw heterostructure during the transfer process. Figure 3.9.4 (e) and (f) are the bottom hBN and graphite back gate. By the PC dry transfer method, we can establish $WS_2$/BLG/$WS_2$/hBN/Graphite stack, as shown in Figure 3.9.4 (g). The (h) is the enlarged optical microscope image of (g). The bilayer graphene can be seen simply by changing the contrast of OM. After the lithography process, I succeeded in making the Superconductor-normal metal-superconductor (SNS) junction with Molybdenum Rhenium (MoRe) superconducting contacts. Then I used the PDMS stamp method, like section 3.3, covering the top hBN upon the device, as shown in Figure 3.9.4 (i). In the end, I did lithography again to deposit Ti/Au as the top gate on the SNS junctions. All the steps in the device fabrication process are displayed in Figure 3.9.5.

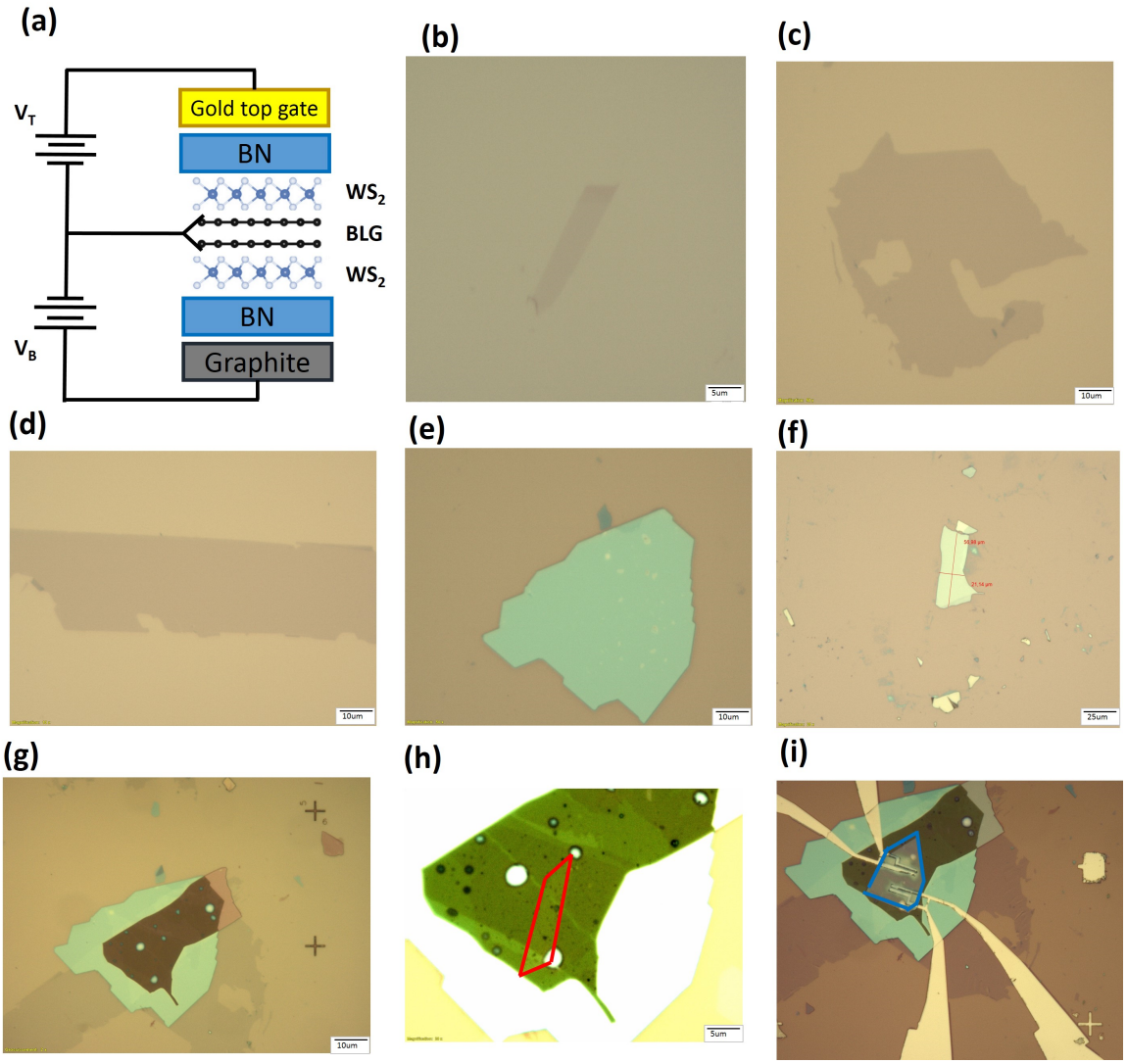


Fig. 3.9.4 (a) Device schematic for a symmetrically $WS_2$ encapsulated bilayer graphene device. (b) Bilayer graphene is made by exfoliation. (c) Monolayer $WS_2$ is made by Au-layer assisted exfoliation. (d) Same as (c). (e) Thin bottom hBN flake. (f) Graphite flake as a back gate. (g) The stack of $WS_2$/BLG/$WS_2$/hBn/Graphite is fabricated by the PC dry transfer method. (h) Enlarged optical microscope image of (g). The red circle is the location of bilayer graphene. (i) Stamping the top hBN on the junctions by the PDMS dry transfer. The blue shape is the top hBN after covering the device.

After we got the desired vdw heterostructure, I chose recipe 4 (shown in Figure 3.8.3) for this work because the estimated thickness of the vdw heterostructure is larger than 50nm. In the beginning, I used the spin coater coating PMMA A6 950 resist on the substrate, then drew the cross marks pattern close to my target stack by the e-beam lithography. After immersing the substrate into the developer, the cross marks are clearly seen, as shown in Figure 3.9.5 (a) and (b). Those cross marks are important for us to identify the location of bilayer graphene so that we can precisely draw the designed pattern on the bilayer graphene. Afterward, we used e-beam lithography again to make the designed pattern accurately on the bilayer graphene with the help of cross marks. After drawing the designed pattern by e-beam lithography and removing the resist by the developer, the designed device pattern is exactly located on the position of bilayer graphene, as seen in Figure 3.9.5 (c) and (d).

Before the deposition of MoRe superconducting contacts, it's important to notice that we have to use the reactive ion etching or ion beam etching to etch through the top monolayer $WS_2$ in order to reach the bilayer graphene ($WS_2$/BLG/$WS_2$/hBN/Graphite). After the etching step, we keep the sample in a high vacuum sputtering PVD chamber to deposit the MoRe superconducting contacts on the sample. Then, we immersed the sample in the Dimethyl sulfoxide (DMSO) solvent to remove the resist. The following step is to cover the device with top hBN. In this case, we directly exfoliated hBN on PDMS and then stamped the hBN as a dielectric layer upon the region of the junction, as the description in section 3.3. After the etching, PVD deposition, and stamping hBN steps, the image of junctions have shown in Figure 3.9.5 (e) and (f). The length between 2 contacts is around 300nm. Finally, we did spin coating of resist, e-beam lithography, Ti/AU deposition by e-gun PVD, and lift-off again to create top gates on hBN. The images of the final device are in Figure 3.9.5 (g), (h).

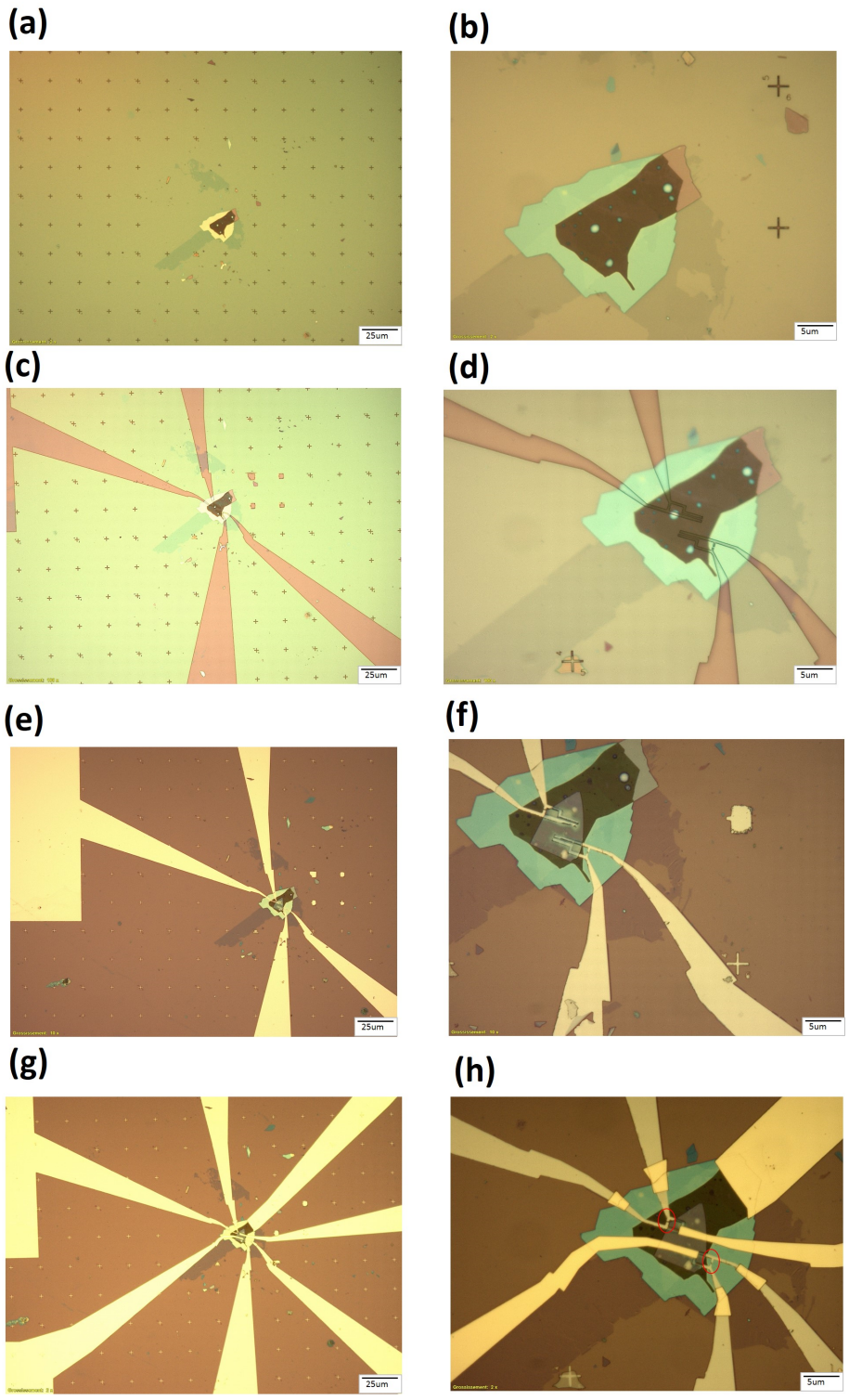


Fig. 3.9.5 (a)(b) Optical microscope image at 20x and 100x magnification after spin coating resists, e-beam lithography, and developing process. The cross marks are clearly seen. (c)(d) Optical microscope image at 20x and 100x magnification after drawing the designed pattern by e-beam lithography. (e)(f) After the PVD deposition of MoRe superconducting contacts and lift-off to remove the resist. Then we covered the top hBN flake of the region of the junction as a dielectric layer by PDMS dry transfer method. (g)(h) Repeating the spin coating, e-beam lithography, developing, PVD deposition, and lift-off process again to create Ti/Au top gates.

From work in chapter 4, we showed that the strong spin-orbit interactions induced in graphene by $WS_2$ lead to the formation of quasi-ballistic edge states, which are stabilized by the strong SOIs. The effects of proximity-induced SOI on van der Waals heterostructures built around bilayer graphene (BLG) and tungsten diselenide ($WSe_2$) have been confirmed in the formation of a distinct incompressible, gapped phase at charge neutrality by using high-resolution capacitance measurements, to enable observation of new topological phases [96]. This research paved the way for us to go further in the investigation of strong SOI induced in graphene by WS2. The vdw heterostructure is shown in Figure 3.9.4 3.9.4 (a).

### Before closing the SQUID loop

We plan two steps for the investigation of this sample. First, before closing the SQUID loop (red circle in Figure 3.9.5 (h)), the device is a simple SNS junction. In the beginning of the measurement, a resistance map as a function of the top gate and bottom gate can be a useful tool to indicate the emergence of a gate-tunable insulating state and edge state. Afterward, by controlling the magnetic field and different dephasing effects, the Fraunhofer pattern can be a beautiful method to exhibit interference effects and to investigate the transition of bulk state to edge state by tuning the top gate and bottom gate voltage. In the higher field regime, we should be able to see robust proximity-induced superconductivity that persists in high magnetic fields due to the protected quasi-ballistic edge states.

### After closing the SQUID loop

After the transport measurement of a simple SNS junction, we can close the SQUID loops by deposition of tungsten in the device (red circle in Figure 3.9.5 (h)). Because the transport is expected to occur ballistically along two edges of bilayer graphene with strong induced SOIs, we can use the extreme sensitivity of the "current-phase" relation (CPR) between the Josephson current ($I_j$) flowing through bilayer graphene and the superconducting phase difference at its ends monitored by the flux through the SQUID $\phi$. The CPR of a Superconductor/Insulator/Superconductor (SIS) Josephson junction is known as sinusoidal $I_j(\phi)=I_J\sin\phi$, where $I_C$ is the critical current [97].We expect to find the superposition of two sawtooth-shaped signals of slightly different periods demonstrating the ballistic conduction along two edges of the bilayer graphene.

**Fano resonance on graphite/$WS_2$/graphite sample deposited onto sapphire(0001) substrate.**

The graphite/$WSS_2$/graphite sample was deposited onto a sapphire(0001) substrate made for the STEM group. This sample was used for optical extinction measurements at 6K by their collaborators to confirm the results observed in electron energy-loss spectroscopy on similar samples deposited onto holey carbon support TEM grids. Following the work of substrate effects, graphite, which should also satisfy all the criteria of a good substrate but as a conductor, was also investigated. Similar to the hBN encapsulation sample, graphite encapsulation also demonstrated narrow exciton absorption linewidths. However, asymmetric (instead of Lorentzian) lineshapes reminiscent of Fano resonance were observed. Such lineshapes can be described by a two-dimensional sheet conductivity model of the TMD in the presence of the conductive environment to reflect the electromagnetic coupling between the TMD and the graphite. The results from these samples are summarized in a manuscript in preparation (Steffi Woo et al.).

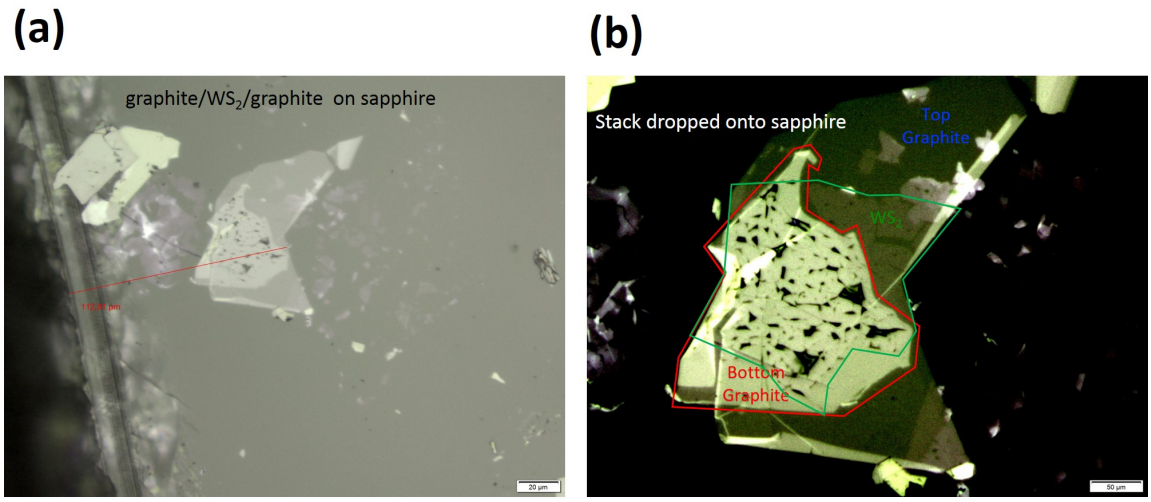


Fig. 3.9.6 (a) Optical microscope image of graphite/$WS_2$/graphite on sapphire substrate. (b) Enlarged image of the stack in (a).

# Chapter 4

# SOI Enhanced Robustness of Supercurrent in Graphene/$WS_2$ Josephson Junctions

In this chapter, we describe the study of graphene/$WS_2$ Josephson Junctions. We present the results showing that spin-orbit interactions (SOIs) enhances the robustness of the measured supercurrent. The text and figures are published in our article [98], and I was in charge of carrying on the measurement and plotting the result figures from experimental data.

In this work, we demonstrate the enhanced robustness of the supercurrent through graphene-based Josephson junctions in which strong spin-orbit interactions (SOIs) are induced. We compare the persistence of a supercurrent at high out-of-plane magnetic fields between Josephson junctions with graphene on hexagonal boron-nitride and graphene on $WS_2$, where strong SOIs are induced via the proximity effect.We find that in the shortest junctions both systems display signatures of induced superconductivity, characterized by a suppressed differential resistance at a low current, in magnetic fields up to 1 T. In longer junctions, however, only graphene on $WS_2$ exhibits induced superconductivity features in such high magnetic fields, and they even persist up to 7 T. We argue that these robust superconducting signatures arise from quasiballistic edge states stabilized by the strong SOIs induced in graphene by $WS_2$.

## 4.1 Motivation

Magnetic fields are known to be detrimental to ordinary s-wave superconductivity because of the pair-breaking effect of the Zeeman component, which can flip the spins in the spin-singlet Cooper pair [51]. Magnetic fields also affect superconductivity via an orbital effect, a geometry dependent dephasing of Cooper pairs by the vector potential. This orbital effect determines the field-dependent interference pattern of the critical current in spatially extended Josephson junctions [99][100].

Spin-orbit interactions (SOIs) play a crucial role in mitigating these field-induced pair-breaking effects. Recently, Ising pairing in transition-metal dichalcogenides (TMDs)was found to confer the robustness of superconductivity owing to spin-momentum locking, by which the spin polarization of Cooper pairs is prevented[101][102]. While the role of SOIs in stabilizing the spin component of the Cooper pair was emphasized in many previous studies, the effect of SOIs on orbital depairing is only beginning to be explored [103][104].

In this Letter, we demonstrate that SOIs can enhance the superconducting proximity effect in high out-of-plane magnetic fields in graphene-on-$WS_2$-based Josephson junctions. These junctions consist of graphene encapsulated between hexagonal boron nitride (hBN) and $WS_2$, which induces strong SOIs in graphene via the proximity effect[15, 10, 11, 16, 17]. The magnetic field dependence of the critical current through graphene-based superconductor–normal-metal– superconductor junctions has been already extensively studied [105–107]. It is characterized by a Fraunhofer-like pattern resulting from interference between the uniformly distributed Andreev pair trajectories and decays rapidly at fields above a few flux quanta through the sample. However, specifically in very clean short ballistic junctions, residual supercurrent periodic oscillations at very high fields were observed and associated with the physics of the quantum Hall (QH) effect [108].

In addition, we also investigate junctions in the opposite, diffusive limit. The junction lengths (L) range between 100 and 500 nm from the short- to long-junction regimes. Although the junctions are diffusive, surprisingly, we find clear signatures of induced superconductivity with manifestations of a supercurrent even in magnetic fields in the Tesla range for the graphene-on-$WS_2$ junctions. By contrast, this behavior is not observed for graphene-onhBN junctions outside the short ballistic regime, i.e., for lengths greater than L=200nm. We argue that this robust induced superconductivity arises from quasiballistic trajectories along the sample edges, stabilized by strong SOIs induced in graphene by $WS_2$.

## 4.2 Sample description and characterization in low field

We compare two types of samples: hBN/graphene/$WS_2$ (Gr/$WS_2$) and hBN/graphene/hBN (Gr/hBN) junctuibs. Graphene and hBN are mechanically exfoliated from graphite and hBN crystals, and monolayer $WS_2$ flakes are grown by chemical vapor deposition [109]. hBN and graphene are picked up by the typical dry-transfer technique with polydimethylsiloxane(PDMS) and polypropylene carbonate(PPC) and then deposited onto $WS_2$ or hBN [13]. One-dimensional superconducting contacts are patterned by electron beam lithography, followed by reactive ion etching and sputtering 100nm MoRe. MoRe is a type-II superconductor with high critical field $H_{c2}$ 80000G (8T) and critical temperature $T_c \simeq$10K [108]. The junctions are defined by their length (L) and width (W), W $\simeq$10m for all samples, whereas L varies between 100 and 500nm, as seen in the Figure 4.2.1 (a). Measurements are performed in a dilution refrigerator, at 100mK unless otherwise specified, using a conventional lock-in technique.

From the previously demonstrated studies via weak antilocalization that graphene on TMDs acquires by proximity strong SOIs thanks to the heavy elements such as molybdenum (Mo) or tungsten (W) that they contain [11, 17, 47]. While the intrinsic SOI in graphene is small (24eV) [43], it is enhanced by contact with a TMD flake, up to 1meV–10meV depending on the type and thickness of the TMDs. Specifically, it was found that monolayer tungsten-based TMDs such as $WS_2$ or $WSe_2$ induce the strongest SOIs in graphene [11, 17]. Therefore, our Gr/$WS_2$ junctions include graphene with strong SOIs as a normal region. Since the resistivity of the TMDs is much larger than that of graphene, the electrical current can be considered to flow entirely through the graphene in the Gr/TMD bilayer.

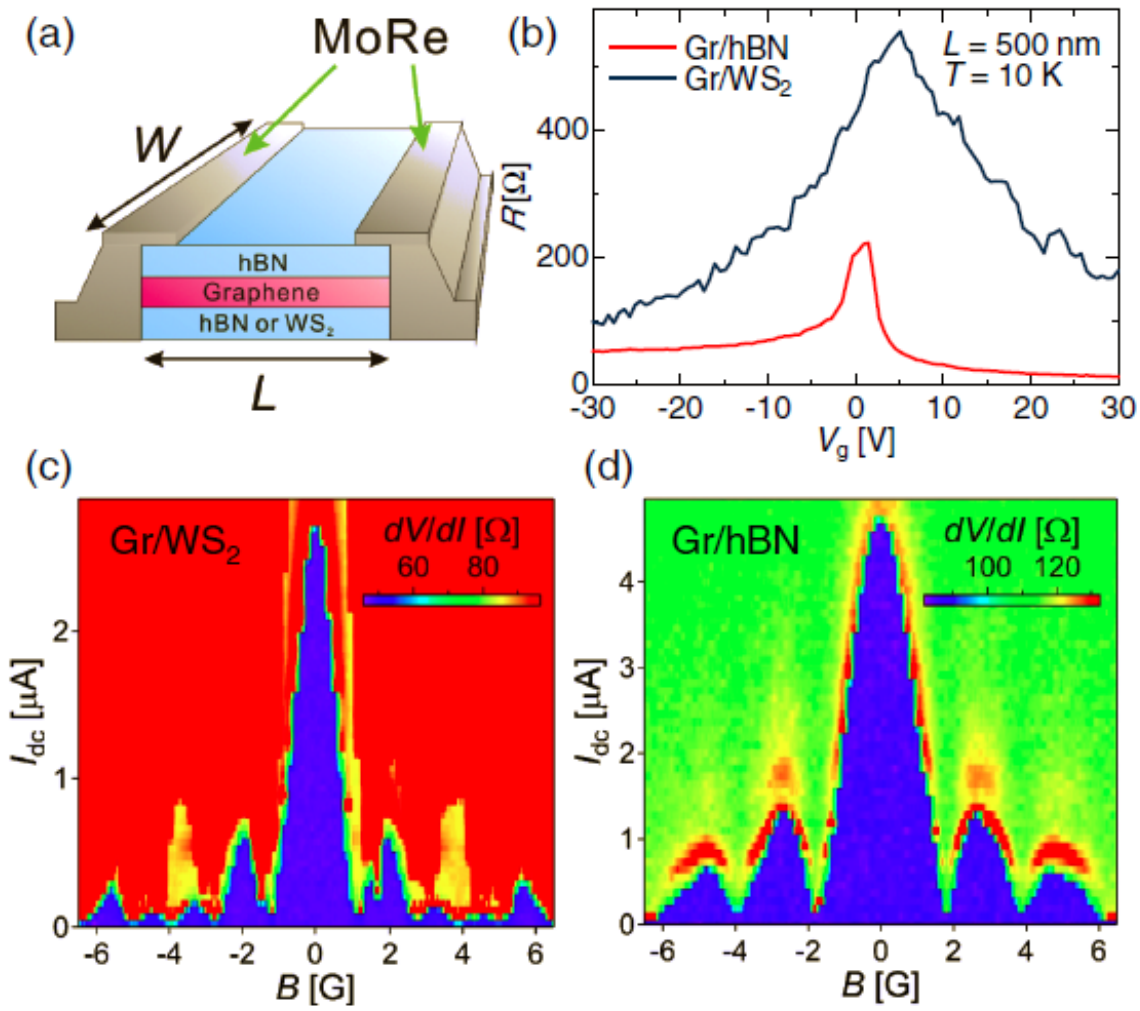


Fig. 4.2.1 Device structure and transport properties around zero magnetic field. (a) Schematic illustration of a graphene-based Josephson junction device of length L and width W employed in this study. (b) $V_g$ dependence of R for the Gr/$WS_2$ and Gr/hBN junctions with MoRe in the normal state (L = 500nm). The contact resistance is subtracted in the data. (c),(d) Color-coded dV=dI, plotted as a function of Idc and B for Gr/$WS_2$ [(c)] and Gr/hBN junctions [(d)] with L = 500nm measured at $V_g$ = 60 V.

We first discuss the results in the normal state. 4.2.1 (b) displays a typical gate voltage ($V_g$) dependence of the resistance (R) for Gr/$WS_2$ and Gr/hBN junctions (L = 500 nm) measured above the $T_c$ of MoRe in zero field. The Dirac peak is sharper in the Gr/hBN junction than in the Gr/$WS_2$, indicating that the mobility of graphene on hBN is higher than that of graphene on $WS_2$. While it is reported that multilayered TMD flakes may constitute as flat and clean substrates for graphene as hBN [96], we note that in our experiments we work with monolayer TMD grown by chemical vapor deposition, which may contain polymer residues left over from the transfer process to the sample substrates and which also is not as flat as the multilayer hBN used for the Gr/hBN junctions. In fact, all the Gr/hBN junctions have higher mobility than the Gr/$WS_2$ junctions. Particularly, the Gr/hBN junction with L = 100nm displays oscillations of R with $V_g$ in the hole-doped region, consistent with previous reports of Fabry-Perot oscillations [105, 106]. This is also in agreement with our estimate of a mean free path $l_e$ 100nm from diffusive samples whose L is longer than $l_e$. Interestingly, Fabry-Perot oscillations are not observed in Gr/$WS_2$ junctions even for L = 100 nm, consistent with the lower mobility of Gr/$WS_2$ junctions.

After cooling the sample below Tc of the superconducting contacts, we measured the differential resistance (dV=dI) as a function of the dc current (Idc) and magnetic field (B) around zero field. A small ac current Iac was added to Idc, and the corresponding ac voltage was detected by a lock-in amplifier, yielding dV/dI. Figure 4.2.1 (c)(d) displays the color-coded dV/dI of Gr/$WS_2$ and Gr/hBN junctions [L = 500nm, same samples as Fig. 4.2.1(b)] as a function of Idc and B at low fields. Both samples exhibit clear regions with zero dV/dI at a low dc current, corresponding to an induced supercurrent. Deviations from the typical Fraunhofer pattern are presumably due to current inhomonegeities through the junctions. We note that the critical current (Ic), defined by Idc at which dV/dI is maximum, is larger for the Gr/hBN junction than that for the Gr/$WS_2$ junction. This indicates that the induced superconductivity is stronger for the Gr/hBN junction at low fields and is consistent with the higher mobility of the Gr/hBN junctions [see Fig. 4.2.1(b)].

The low field behavior displayed in Fig. 4.2.1(c),(d) is the expected Fraunhofer-like interference pattern for a supercurrent flowing uniformly throughout the entire width of the graphene sheet [51, 99, 100].Whereas the value of Ic varies for different junctions, similar behaviors are observed for all junctions. The oscillation period corresponds to the junction area if the magnetic focusing effect is taken into account [110–112].

## 4.3 Characterization in high field

To investigate the induced superconductivity at high fields, we next increased B around 1T (10000G) and similarly measured dV/dI as a function of Idc and B. Figure 4.3.1 compares Gr/$WS_2$ and Gr/hBN junctions with different L (L = 100, 300, and 500nm). Considering the relation between the Thouless energy ($E_T = \hbar D/L^2$) with the diffusion constant D in the diffusive regime and $E_T = \hbar v_F/L$ in the ballistic regime) and the superconducting gap $\Delta_0$ (= 1 meV) of MoRe, both L = 100nm junctions are in the short-junction limit ($E_T > \Delta$), while the others are in the long-junction limit ($E_T < \Delta$). Interestingly, for the shortest, L = 100nm, junctions, a relatively large 100nA wide dip of dV/dI is observed in certain fields, even around 8000G for both Gr/$WS_2$ and Gr/hBN junctions, and oscillates as a function of B. In the previous study on graphene ballistic Josephson junctions [105], field dependent and sample-specific differential resistance dips at a low current were also observed around 5000G, and the B and $V_g$ regions of low dV/dI were termed "superconducting pockets." In our shortest samples, the superconducting pockets are still visible around B = 16000G for the Gr/$WS_2$ junction. We note that all Gr/$WS_2$ junctions, even the shortest one with L = 100 nm, are in the diffusive limit because of the shorter $l_e$. Whereas the field dependence is similar for both types of 100-nm-long junctions, we find a stark difference for the longer junctions, L = 300 and 500nm. While superconducting pockets persist around B = 10000G for Gr/$WS_2$, they are clearly suppressed for Gr/hBN. We note that the typical oscillation field scale of the superconducting pockets is about 1.5G, identical to the width of the Fraunhofer-like pattern main lobe.

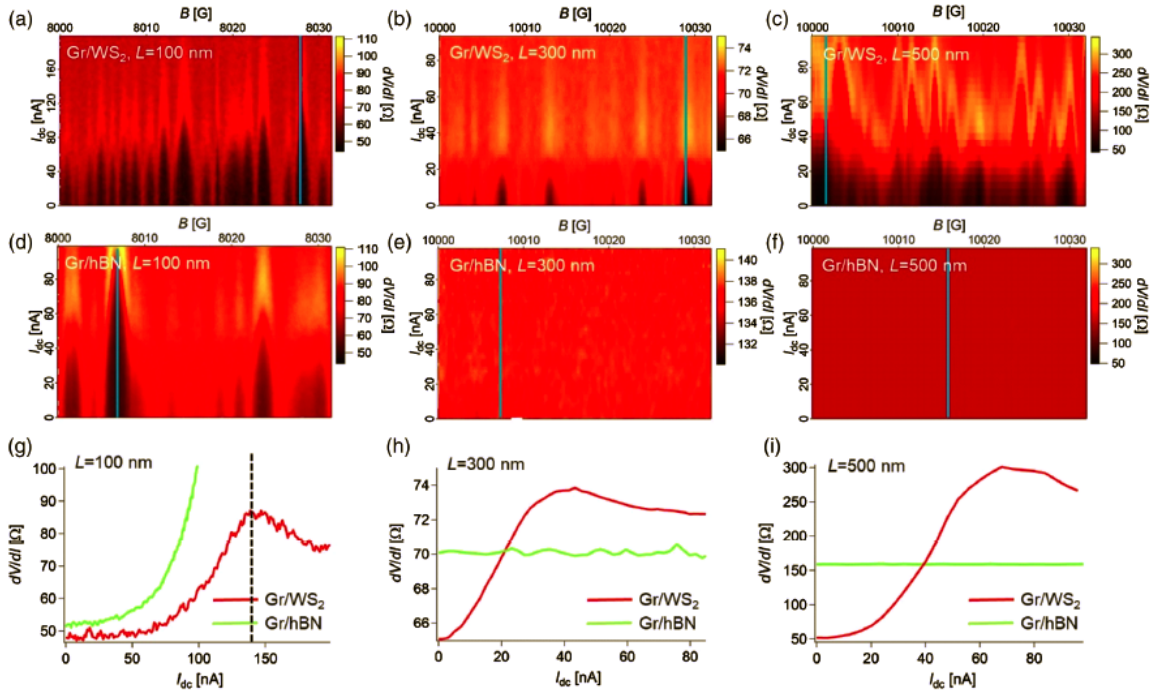


Fig. 4.3.1 Color-coded dV/dI as a function Idc and B around B = 10000G at $V_g$ = 60V for all samples. For L = 100nm [(a),(d)], superconducting pockets are clearly visible, in the form of field regions of low dV/dI at low Idc, for both the Gr/$WS_2$ and Gr/hBN junctions around B = 8000G. For L = 300nm [(b),(e)] and L = 500nm [(c),(f)], superconducting pockets are visible only for the Gr/$WS_2$ junction. (g)–(i) Cross-sectional image along the light blue line shown in (a)–(f) of dV=dI as a function of Idc forGr/$WS_2$ and Gr/hBN junctions with different L. Red and light green curves are from Gr/$WS_2$ and Gr/hBN junctions, respectively. The suppressed dV/dI at low Idc, signature of an induced superconducting proximity effect, is clearly visible for the Gr/$WS_2$ junctions of every length but only for the shortest Gr/hBN junction. In (g), the peak (or bump) of dV/dI for Gr/hBN is located out of the range of Idc in the measurement, and in (h) [(i)], the dV/dI for Gr/hBN (Gr/$WS_2$) is vertically shifted to compare to that for Gr/$WS_2$ (Gr/hBN). The residual resistance around 50 at Idc = 0 for (a)–(i) arises from the measurement wires. The dashed line in (g) represents the value of Idc, which defines Ic.

In 4.3.2, we provide the data from the L = 500nm Gr/$WS_2$ junction, displaying how the oscillations persist up to 70000G. These results demonstrate that superconducting pockets can persist at much higher fields for Gr/$WS_2$ than for Gr/hBN, in the longest junctions.

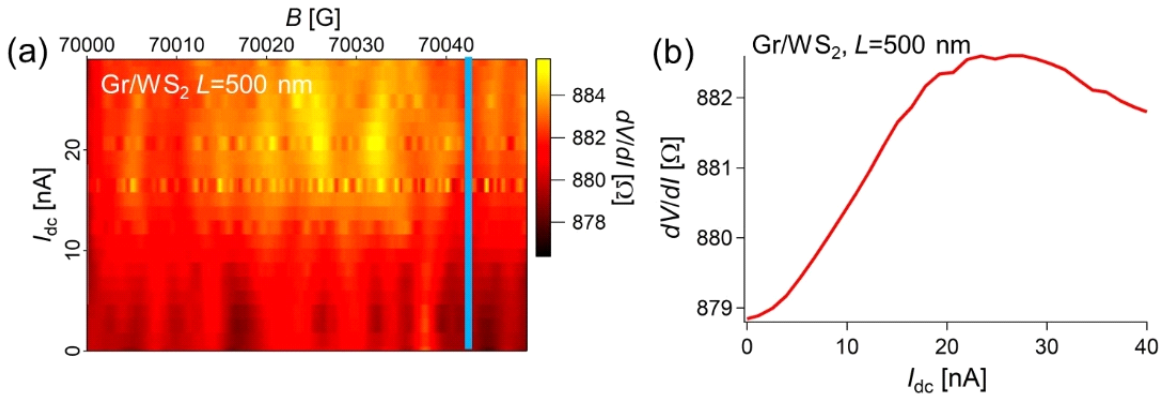


Fig. 4.3.2 Supercurrent fluctuation at B=70000 G and Vg = 60 V, from a L = 500nm Gr/$WS_2$ junction:(a) Supercurrent fluctuations around B = 70000G(7T) for L = 500nm Gr/$WS_2$ junction at Vg = 60V. The crosssectional image in (b) is taken along the light blue line in (a) after averaging over a field window of 2 G to minimize the noise due to the pixelization.

Beyond these dV/dI maps as a function of Idc and B in limited field regions, a broader picture can be obtained by following dV/dI at zero dc current bias (ZBR) over a wide range of B. ZBR oscillates between the normal state resistance when no superconductivity is induced and has a minimal dV/dI in the middle of the superconducting pocket when the superconducting proximity effect is strongest. Figure 4.3.3 shows the ZBR as a function of B for all junctions. For L=100nm, the ZBR oscillates with a large amplitude both for Gr/$WS_2$ and Gr/hBN, even near B=18000G. On the contrary, for L = 300nm, oscillations are strongly suppressed, especially for B > 5000G for Gr/hBN, while they persist for Gr/$WS_2$ even at higher fields. The difference is even more striking for the L = 500nm junctions. The oscillation amplitudes are considerably different already at a small field, and large oscillations are visible at B = 18000G for Gr/$WS_2$, while Gr/hBN exhibits almost no oscillations over the entire B range.

We now discuss possible mechanisms by which SOIs can enhance the robustness of the induced superconductivity at high fields. Superconducting pockets at high fields have already been discussed for ballistic junctions [105] in terms of Andreev bound states mediated by chaotic ballistic billiard paths localized at the edges of graphene. Those paths can be considered a ballistic analog of the quasiclassical phase-coherent paths and produce mesoscopic fluctuations of the supercurrent $I_c = \sqrt{< I_c^2 > - < I_c >^2}$ [113]. In the ballistic short junction limit, Ic is estimated as [114].

$$\delta I_c \sim \frac{e\Delta_0}{\hbar} \tag{4.3.1}$$

where $\Delta_0$ denotes the superconducting gap at T = 0. In the diffusive long-junction limit [113, 115],

$$\delta I_c \sim \frac{eE_T}{\hbar}\sqrt{\frac{W}{L}} \tag{4.3.2}$$

We find $\delta I_c \sim$ 240 nA from Eq. (4.3.1) expected to be adequate for short Gr/hBN junctions but slightly larger than our experimental value. Reduced experimental values compared to the theoretical ones were already reported [116, 117] and may be attributed to barriers at the normalmetal–superconductor interface, along with electromagnetic noise or finite temperature effects. We then estimate $\delta I_c$ for diffusive junctions by using Eq. (4.3.2) and obtain $\delta I_c \sim$ 100nA and 50nA for L = 300 and 500 nm, respectively. The latter is in almost perfect agreement with the experimental result, while the former is larger than the

experimental value. However, Eqs. (4.3.1) and (4.3.2) were evaluated for zero field. The field dependence of the critical current was recently theoretically investigated in two-dimensional ballistic junctions similar to our samples [118].

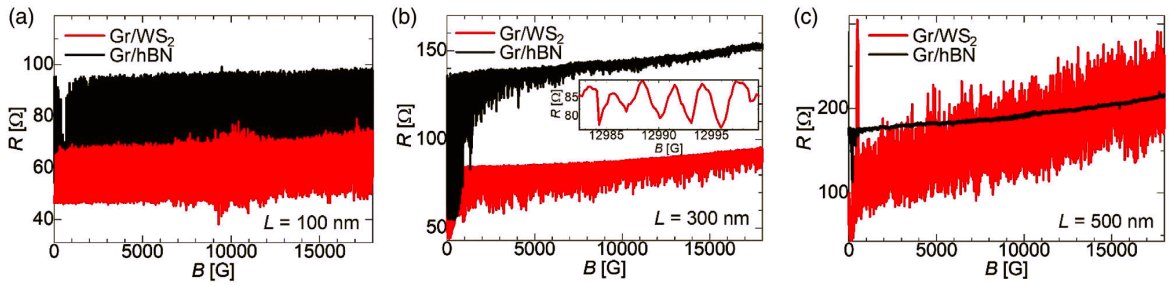


Fig. 4.3.3 Monitoring the superconducting proximity effect over a wide field range, via the zero bias differential resistance variations with B, for the three junction lengths and both Gr/$WS_2$ and Gr/hBN systems, at $V_g$ = 60V. (a) For L = 100nm, both Gr/$WS_2$ and Gr/hBN junctions display comparable oscillation amplitudes up to B $\sim$ 20000G. (b) For L = 300nm, whereas the Gr/hBN junction displays larger amplitude oscillations near B=0, they are rapidly suppressed as B increases. By contrast, the Gr/$WS_2$ junction displays a relatively large amplitude of resistance oscillations that persists even around 20000G. (c) The difference between Gr/$WS_2$ and Gr/hBN is the most striking for L = 500nm junctions. The relative oscillation amplitude of the Gr/$WS_2$ junction's differential resistance is around 50 times greater than that of the Gr/hBN junction over the entire field range. The inset in (b) displays a magnified view of the oscillations for Gr/$WS_2$ around B = 13000G.

As B increases, the supercurrent is localized near the edges, and $I_c$ decays faster ($I_c \propto 1/B^2$) than the typical current fluctuations $I_c$ [118]. Moreover, those fluctuations can persist up to high fields for edges whose roughness is characterized by a correlation length of the order of or larger than the Fermi wavelength. In these conditions, they find $\delta I_c = \alpha E_T/\Phi_0$, independent of field, which corresponds to the current carried by one ballistic channel, with $\alpha = 2\pi/9\sqrt{3}$. This yields $I_c$ 200 nA for the 100-nm-long Gr/hBN junction, in qualitative agreement with our experimental findings. These high field fluctuations are specific to ballistic junctions and therefore not expected in the diffusive regime.

As we comment in the previous text, supercurrent fluctuations are still observed at B = 70000G for the L = 500nm Gr/$WS_2$ sample. This is clearly shown in Fig. 4.3.2. The difference in the oscillation amplitude between Gr/$WS_2$ and Gr/hBN junctions is most striking for L = 500 nm samples. Figure S6 displays the full data of dV/dI compared between Gr/$WS_2$ and Gr/hBN junctions for L = 500nm up to B = 70000G. While the amplitude of the oscillations decays as B increases, it is still much larger for Gr/$WS_2$ than for the Gr/hBN junction at 70000G. This data clearly shows that supercurrent fluctuations can persist even at high fields for graphene with strong SOIs.

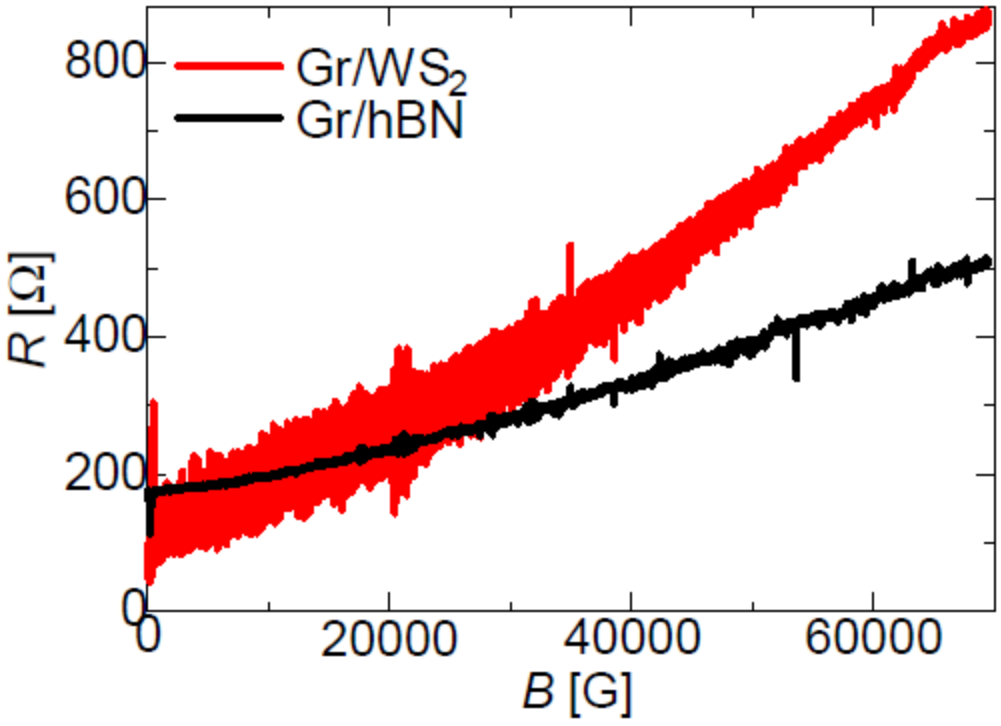


Fig. 4.3.4 Zero-bias dV/dI as a function of B up to a high field: dV/dI for Gr/hBN and Gr/$WS_2$ junctions for L = 500nm from B = 0G to 70000G at $V_g$ = 60V. Striking difference in the oscillation amplitude between Gr/hBN and Gr/$WS_2$ junctions can be seen.

## 4.4 Explanation

In order to explain the robust supercurrent signatures that we find in the diffusive Gr/$WS_2$ junctions, it therefore seems necessary to consider the role of SOIs. SOIs favor the formation of edge states, epitomized by the topological quantum spin Hall phase. However, edge states can also exist in a nontopological system and coexist with bulk states of the same energy. Such edge states are in general sensitive to scattering, but some degree of protection against smooth disorder may exist if the edge states are well separated from bulk states in momentum space. Moreover, spin can also provide additional protection if the spins of the edge state and those of the nearby bulk band are opposite. In the case of graphene on $WS_2$, the analysis of weak antilocalization experiments [11, 16, 17] has shown that the induced SOIs have both a Rashba-type in-plane component and a tenfold larger out-of-plane component, predominantly of the valley Zeeman type probably [119, 120]. The combined effect of these two types of interactions was theoretically shown to generate nontopological edge states along zigzag edges [121]. To explore whether such edge states may explain the persistence and oscillations of supercurrent at high fields, the simulations of Ic as a function of B in graphene stripes containing different types of SOIs. We find that a supercurrent persists up to higher fields with SOIs than without SOIs, even when disorder is included.

We now examine the relation between these edge paths and the chiral edge states of the QH regime. The QH regime develops when the mean free path $l_e \gg 2r_c$ where rc is the cyclotron radius ($l_e = \hbar k_F / eB$) [108]. At $V_g$ = 60V and B = 10000G, for example, $2r_c$ 500nm, thus chiral edge states do not contribute to the Andreev bound states localized at the edge. We note that this $2r_c$ value is much larger than $l_e$ = 30nm of L = 500nm Gr/$WS_2$ junction. At higher fields, $r_c$ becomes smaller than $l_e$, so that the Landau localization of bulk states and the formation of chiral edge states may become relevant. We observe superconducting pockets even at 70000G for the Gr/$WS_2$ junction for L = 500nm, and $\delta I_c \sim$ 30nA, Figure 4.3.2. This value is, however, more than 1 order of magnitude larger than $\delta I_c$ reported in the QH regime with a comparable $r_c$ for shorter and narrower junctions with better quality graphene [108]. This may indicate that the supercurrent enhancement by the SOIs can also be effective in the QH regime.

Another effect of SOIs recently suggested theoretically is the generation of spin-triplet supercurrent flowing close to the edge in combination with magnetic field or exchange interaction in superconductor–normal-metal– superconductor junctions [122–125]. The characteristic confinement length in this case should be the spin-orbit length $\lambda_{so}$, estimated to be of the order of a few hundred nanometer for graphene with strong SOIs. Such a large extent would lead to a supercurrent suppression for fields much below the 10000 gauss range, so that this effect cannot explain the strong lateral confinement we observe. Another interesting possibility, edge supercurrents induced by two-dimensional vortex lattice formation because of Fermi surface warping [126], also seems unlikely because such Fermi surface warping was not observed in the previous angular-resolved photoemission spectroscopy of similar graphene/$WS_2$ samples [127].

## 4.5 Conclusion

In conclusion, we have demonstrated robust proximityinduced superconductivity that persists in high magnetic fields for Gr/$WS_2$ Josephson junctions. Compared to the Gr/hBN control samples, all Gr/$WS_2$ junctions (with L between 100 and 500nm) have lower mobility and are in the diffusive regime. Nevertheless, and most strikingly for longer junctions, superconducting pockets are still observable at 70000G, whereas they are suppressed for Gr/hBN junctions with the same L. We argue that these robust superconducting signatures stem from quasiballistic states confined along the samples edges, stabilized by the SOIs. Because these edge states carry supercurrent at the micrometer scale, one could envisage further investigations, for instance using more elaborate structures for transport measurements, as well as other techniques such as STM or orbital magnetism measurements. Our findings provide important information for progress toward topological superconductivity in which the combined effects of superconductivity and SOIs play crucial roles.

# Chapter 5

# Iron Porphyrin(FeTPP) and Tetracyanoquinodimethane(TCNQ) deposited on graphene

## 5.1 Introduction

**Fe-Porphyrin**

In 1974, the organic molecule was first time used in a functionalized electronic device [128]. The new application of molecular electronics has been widely investigated on the nanometer scale to observe some interesting phenomena, like tunneling electron transport, high-density molecular memory [129, 130], etc.

Recently, using magnetic molecular junctions as spin transport channels has been a novel research field for molecular spintronics [18, 19]. Many experimental and theoretical research results proposed that organic materials perform well in spintronic devices [20, 21]. One of the potential candidates among the organic materials is magnetic porphyrin, such as iron-porphyrin (FeTPP) or platinum-porphyrin (PtTPP), see Figure Figure 5.1.1 (a). The metal complexes of porphyrins offer a wide range of valuable properties, such as conjugated bond structure, well-ordered geometry, and chemical stability [22]. Previous theoretical studies have proven the relatively high spin filtering behavior in $FeN_4$ complexes grafted to graphene nanoribbons or carbon nanotubes [23, 24]. The FeTPP was also used in gas sensing devices due to the controllable electronic current by changing the chemical composition of the molecular junction [25]. The main motivation in this section is inducing magnetism in graphene by coupling with the organometallic molecule FeTPP, which is known to create well-ordered arrays on crystalline conducting surfaces, such as Au, Cu, graphite, and graphene.

### Tetracyanoquinodimethane(TCNQ)

Tetracyanoquinodimethane(TCNQ) is another highly potential candidate to induce magnetism on graphene. Normally, many molecules have shown interaction with the substrate that usually disturbs the magnetism and complicates mutual interactions due to the long distance of magnetic centers [131]. The goal of creating a long-range magnetic ordering of molecules in two dimensions is hard to achieve. One possible approach resulted from discovering magnetic order in organic charge transfer compounds. The metalorganic bulk magnets are composed of Tetracyanoethenide (TCNE), 7,7,8,8-tetracyanoquinodimethane (TCNQ) with metal atoms (V, Fe, etc.), which are intensively studied [132]. These metalorganic bulk magnets reveal long-range magnetic order with high critical temperatures [133, 134]. But properties of a compound always depend on the charge transfer between metal ions and other components. Lately, a new pure organic 2D material with long-range magnetic order has been published [8]. This new system was composed of monolayer TCNQ absorbed on n-doped graphene grown on Ru(0001) substrate; see the chemical structure in Figure 5.1.1 (b). The electron transfer to the TCNQ through the graphene monolayer constitutes a spin-split intermolecular band and leads to long-range magnetic order at 4.6K [8]. The result shows a feasible strategy to add magnetic functionalities to graphene-based heterostructures by deposition of organic molecules.

For TCNQ/Graphene/Ru(0001) system, a study found that the molecules adsorbed on the lower parts of the ripples are charged, but those adsorbed on the upper part of the ripples are not [26]. In addition, the TCNQ molecules lack magnetic moment when adsorbed on the lightly p-doped graphene/Ir(111) substrate. The charge transfer process from gr/Ru(0001) substrate has been proven important to form the intermolecular bands to achieve long-range magnetic order in these purely organic 2D materials [26]. In a nutshell, TCNQ/Graphene/Ru(0001) system is proven to induce magnetic moment and develop long-range magnetic order on TCNQ molecular layer. Here, we're interested in whether the TCNQ also induces magnetic moments on gated graphene.

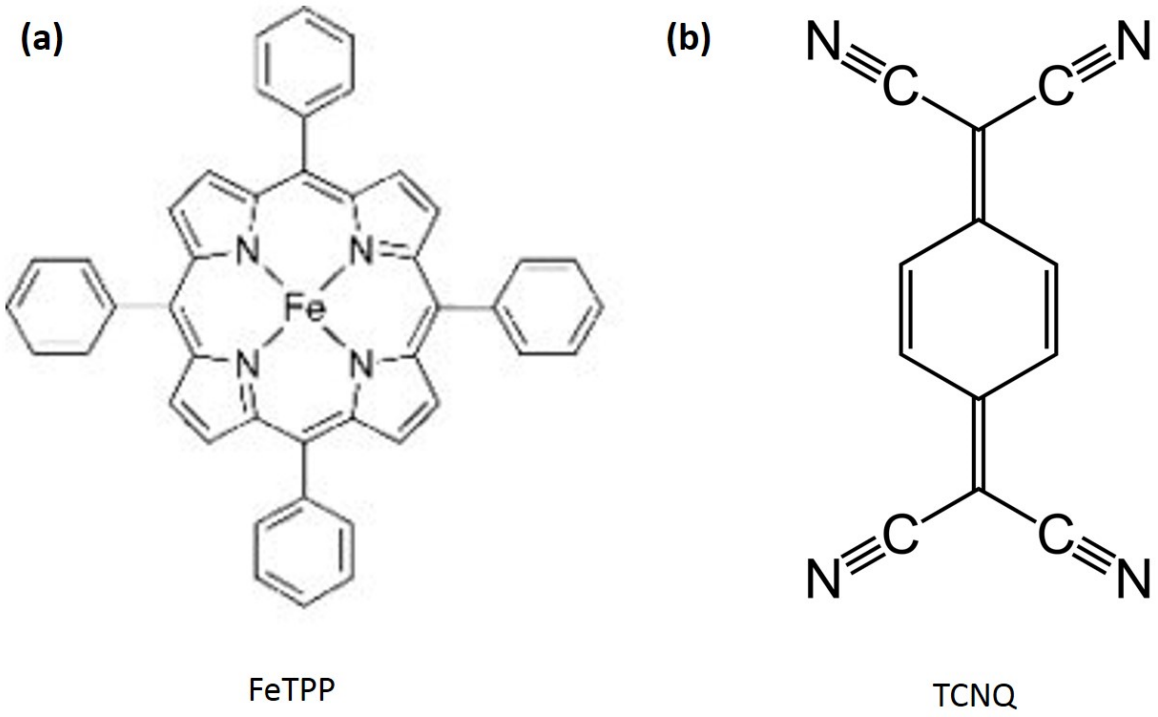


Fig. 5.1.1 (a) Chemical structure of iron porphyrin (FeTPP) molecule. (b) Chemical structure of 7, 7, 8, 8 tetracyanoquinodimethane (TCNQ) molecule.

### Quantum transport as a probe of magnetism

We present a brief discussion of the following results, which are still under analysis. We have shown in section 5.4 that spin-flip scattering in a conductor breaks the phase coherence of electronic wave functions. This is why magnetic impurities are considered the main mechanism limiting the increase of phase coherence length at low temperatures when the inelastic electron-electron interactions are not frequent. The phase coherence length is estimated from the width of the weak localization peak in the low out-of-plane field magneto-conductance. It is, therefore, instructive to compare these estimations on the different samples of graphene coated with magnetic molecules we have investigated. The different behaviors are expected to be seen depending on the coupling between these molecules and conduction electrons in graphene.

## 5.2 Device preparation

The graphene samples were prepared as explained in previous sections by the mechanical exfoliation on $SiO_2$/Si substrate with Ti/Au contacts. Thanks to the collaboration researchers Dr. Jérôme and Dr. Cyril, in the "Laboratoire Matériaux et Phénomènes Quantiques," we were able to deposit 1 to 2 layers of FeTPP and TCNQ molecular layer on each prepared sample by the molecular beam epitaxy. The final structure is in Figure 5.2.1 (a). We measured the gate dependence for all samples at room temperature before and after the deposition of the molecules. The sample size of the FeTPP grafted graphene device is 2.1um length * 3.8um width, and its 2um length * 4.5um width of TCNQ coated graphene sample.

In the Figure 5.2.1 (b), the Dirac point was close to gate voltage 7V (black curve) before the deposition of FeTPP molecular layers, and it shifted 4V to 5V gate voltage after the deposition. This implies that charge transfer occurs between graphene and FeTPP, and the molecules are the electron donor for graphene. Based on the previous study of Platinum porphyrin [27], we knew porphyrins could behave both as electron donors or acceptors, depending on the graphene sheet's initial doping degree. In both donor or acceptor molecules, the Dirac point of graphene is brought toward zero gate voltage: graphene has become neutral. The gate dependence result of FeTPP at room temperature conforms to the previous study of porphyrin [27].

The TCNQ grafted graphene sample also shows a charge transfer from graphene to TCNQ and reveals that the TCNQ molecules are electron acceptors. In the Figure 5.2.1(c), before the TCNQ deposition, the Dirac point is located near 4V in gate dependence measurement, which means the graphene is naturally p-type doped. After the deposition of TCNQ layers on graphene, the Dirac point of the graphene has shifted to the righter position; see in Figure 5.2.1 (c) red curve. Contrary to FeTPP molecules, TCNQ is the electron acceptor to graphene, and graphene gains more holes as the majority after TCNQ deposition. From the study in scanning tunneling microscopy (STM) [8],TCNQ deposited on the epitaxy-grown graphene indicates TCNQ is the strong electron acceptor. The gate dependence measurement is the other evidence to confirm that the TCNQ molecules are electron acceptors to graphene.

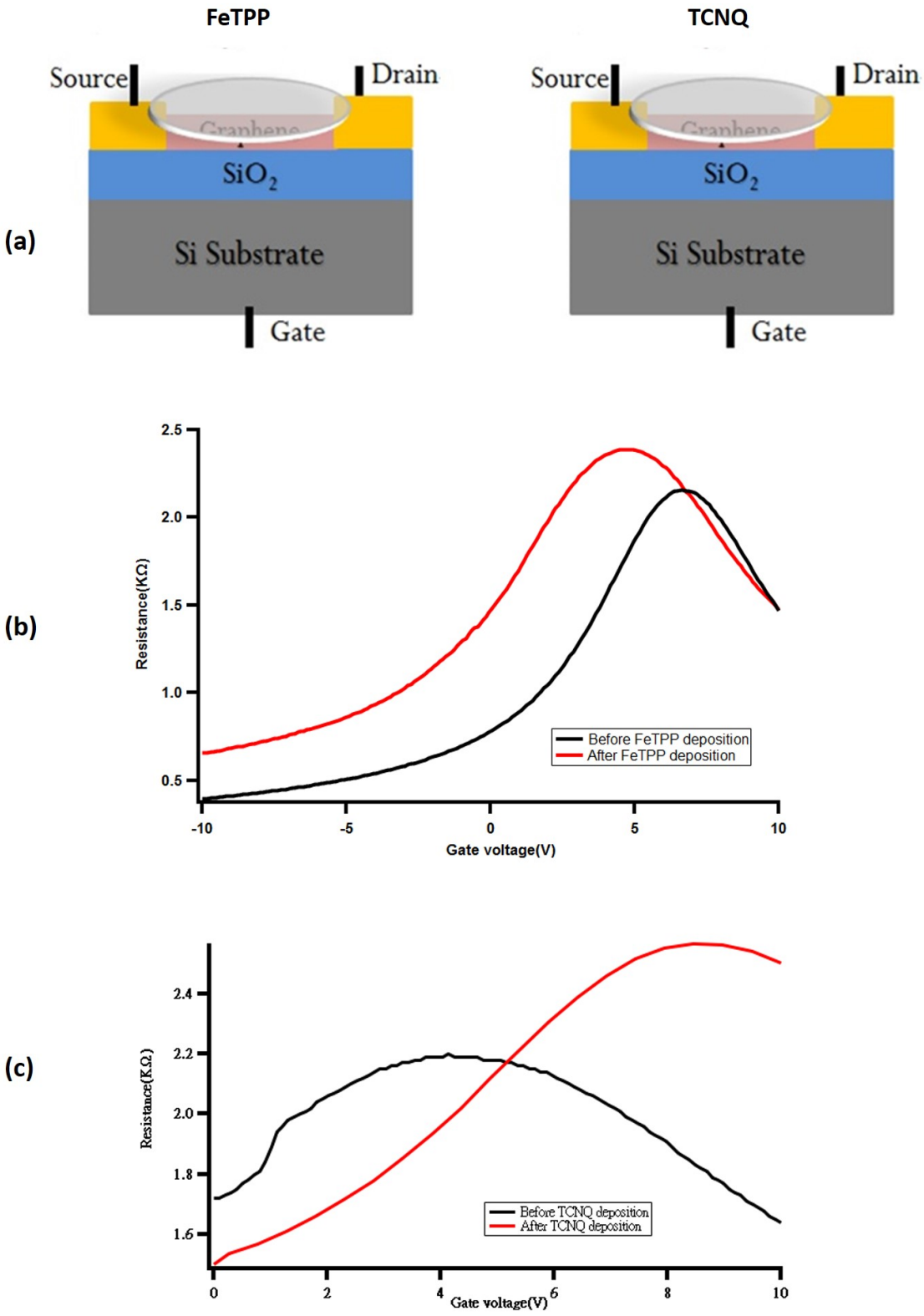


Fig. 5.2.1 (a) Scheme of FeTPP and TCNQ molecular layers grafted on graphene samples by molecular beam epitaxy. (b) Gate dependence at room Temperature before (black curve) and after (red curve) deposition of 1 to 2 layers FeTPP molecule. After the deposition, the charge transfer occurs, and the FeTPP layer is an electron donor to graphene. (c) Same measurement as FeTPP. After the deposition, it also shows the charge transfer, and the TCNQ layer is an electron acceptor to graphene.

## 5.3 In-plane field at 200mK

**Fe-Porphyrin**

In this section, we discuss the magnetoresistance result in the applied in-plane field in both samples at low temperatures because the induced magnetic moment is more sensitive to the applied in-plane field than the out-pf-plane field. Generally, in-plane fields won't directly influence transport since the electronic motion just couples to the component of the magnetic field perpendicular to the graphene. Nevertheless, when the average plane of the graphene sheet is aligned with the applied in-plane field, it introduces a perpendicular component ($\delta B_{\perp}$), which relies on the graphene flake's local slope. The ripples on graphene enable the in-plane field to directly influence transport by changing it to an inhomogeneous out-of-plane field, then forming a random vector potential [135].

Unfortunately, the FeTPP grated-on graphene sample has a back gate leaking problem, so we can't apply the back gate voltage during measurement. Here in Figure 5.3.1 (a), we first move the in-plane field up to 7T, then heat the temperature from 200mK to 6K to agitate the alignment of induced magnetic moment on graphene, then we cool down the temperature from 6K to 200mK afterward. During the quick cooling process, the induced magnetic moment on graphene has been quickly frozen and aligned with the applied in-plane field. Based on this method, the induced magnetic moment on graphene can be realigned and detectable. If there is strong induced magnetism, the magnetoresistance will be asymmetrical by sweeping the in-plane field, which indicates that graphene's time-reversal symmetry has been broken due to the induced magnetic moment. In Figure 5.3.1 (a), we sweep the in-plane field forward and backward between $\pm$2000G five times after heating and cooling at applied 7T in-plane field, and average the sweeping up the curve and sweeping down in Figure 5.3.1 (b). The magnetoresistance measurement shows a symmetrical curve, as seen in Figure 5.3.2 (a), (b) and (c). In addition, the magnetoresistance in the in-plane field for FeTPP grafted graphene sample exhibit reproducible magnetoresistance due to interferences between all the coherent trajectories across the samples. All the in-plane magnetoresistance at heating in the different in-plane fields are symmetric curves, as expected in the presence of time-reversal symmetry of graphene. Depending on the magnetoresistance result, we refer to the weak coupling between graphene and FeTPP molecules that lead to symmetric magnetoresistance.

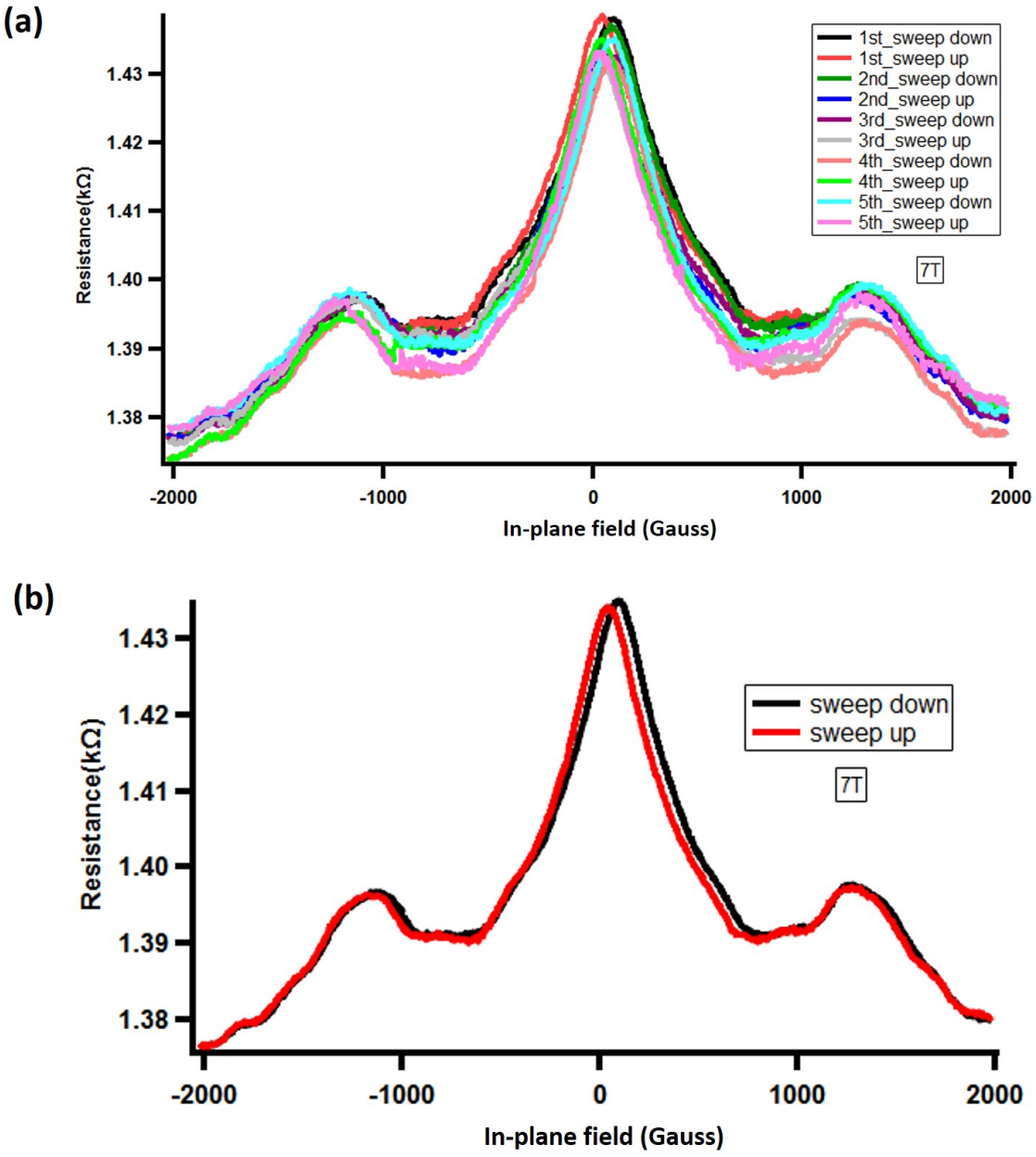


Fig. 5.3.1 (a) In the beginning, we stayed at in-plane Field 7T, then heated the temperature to 7K and waited for the cool down to 200mK. After the cool down, magnetoresistance measurement sweeps between ±2000G in-plane field five times. (b) Each sweeping down curve (black) and up curve (red) is the average result of five curves from (a).

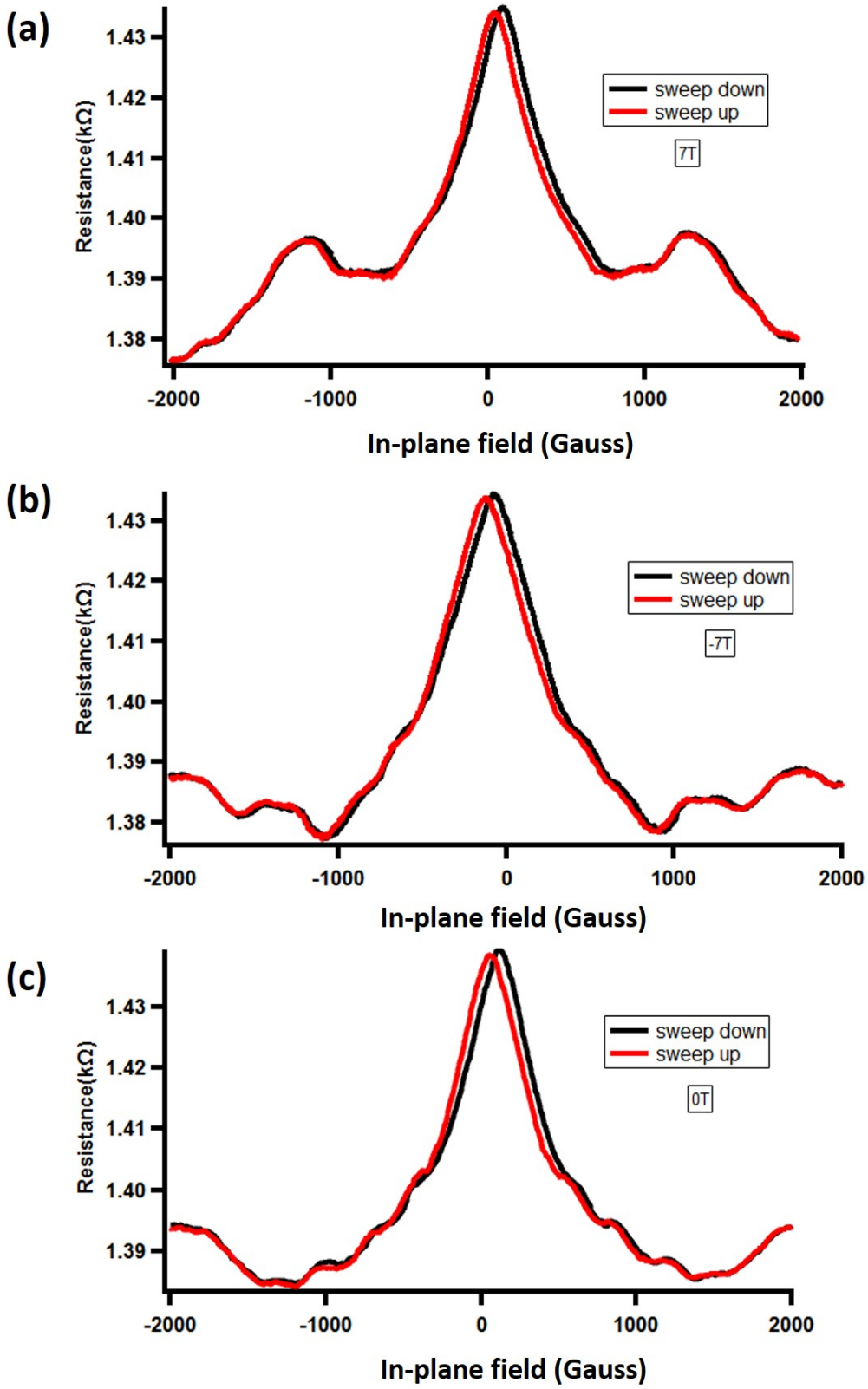


Fig. 5.3.2 (a) Heating and cooling temperature at 7T, then we sweep the in-plane field between $\pm$2000G with $H_{\perp} = 0$. Each curve is the average result from 5 curves. (b) Same measurement, heating and cooling temperature at -7T. (c) Heating and cooling temperature at 0T.

### Tetracyanoquinodimethane(TCNQ)

We did the same measurement for the TCNQ-coupled graphene sample at the same time as the FeTPP-coupled graphene sample. In the TCNQ sample, we expect to see the stronger signature of the induced magnetism because TCNQ molecules deposited on graphene epitaxy-grown on Ru(0001) substrate has revealed the existence of magnetic contrast due to long-range magnetic order between the two TCNQ domains locally in nanometer scales [8]. Figure 5.3.3 is the gate dependence at 200mK. We stay at 50V and -50V gate voltage to do the same measurement as the previous section, heating and cooling at a given in-plane field, then sweeping in the in-plane field.

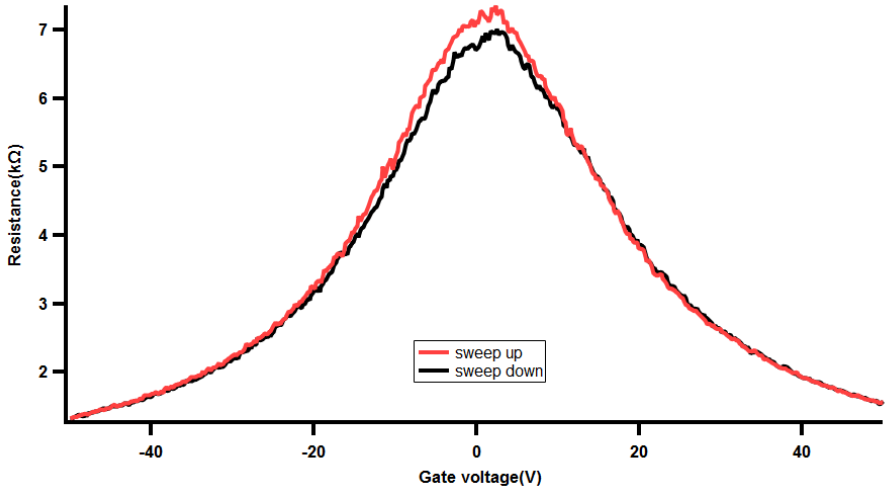


Fig. 5.3.3 Gate dependence of TCNQ grafted on graphene sample at 200mK.

In this sample, one can see that the magnetoresistance in the in-plane field for all curves exhibits asymmetrical magnetoresistance due to the TCNQ-induced magnetic moment on graphene in the presence of time-reversal symmetry breaking, shown in Figure 5.3.4. The TCNQ-coupled graphene sample found a gate-dependent magnetoresistance in the parallel field (Figure 5.3.4 (a). By comparing 50V and -50V, this induced magnetic moment has a stronger effect at applied negative gate voltage because it looks more asymmetrical magnetoresistance. We obtain the same result in Figure 5.3.4 (b) and (c). Interestingly, the clearest asymmetric magnetoresistance reveals at -50V when we heated and cooled the temperature without any applied in-plane field. However, these curves are not reproducible as in FeTPP/Graphene samples, which makes it difficult to discuss a well-defined hysteresis. As shown above, the data measured in the TCNQ-coupled graphene sample in an in-plane field suggest the gate depends on an induced magnetic moment. The asymmetrical magne-

toresistance in all curves indicates the time-reversal symmetry breaking of graphene due to the TNCQ-induced magnetic moment. Here all the MR curves depend strongly on the cooling conditions of the sample, which is not the case for the FeTPP-coupled sample.

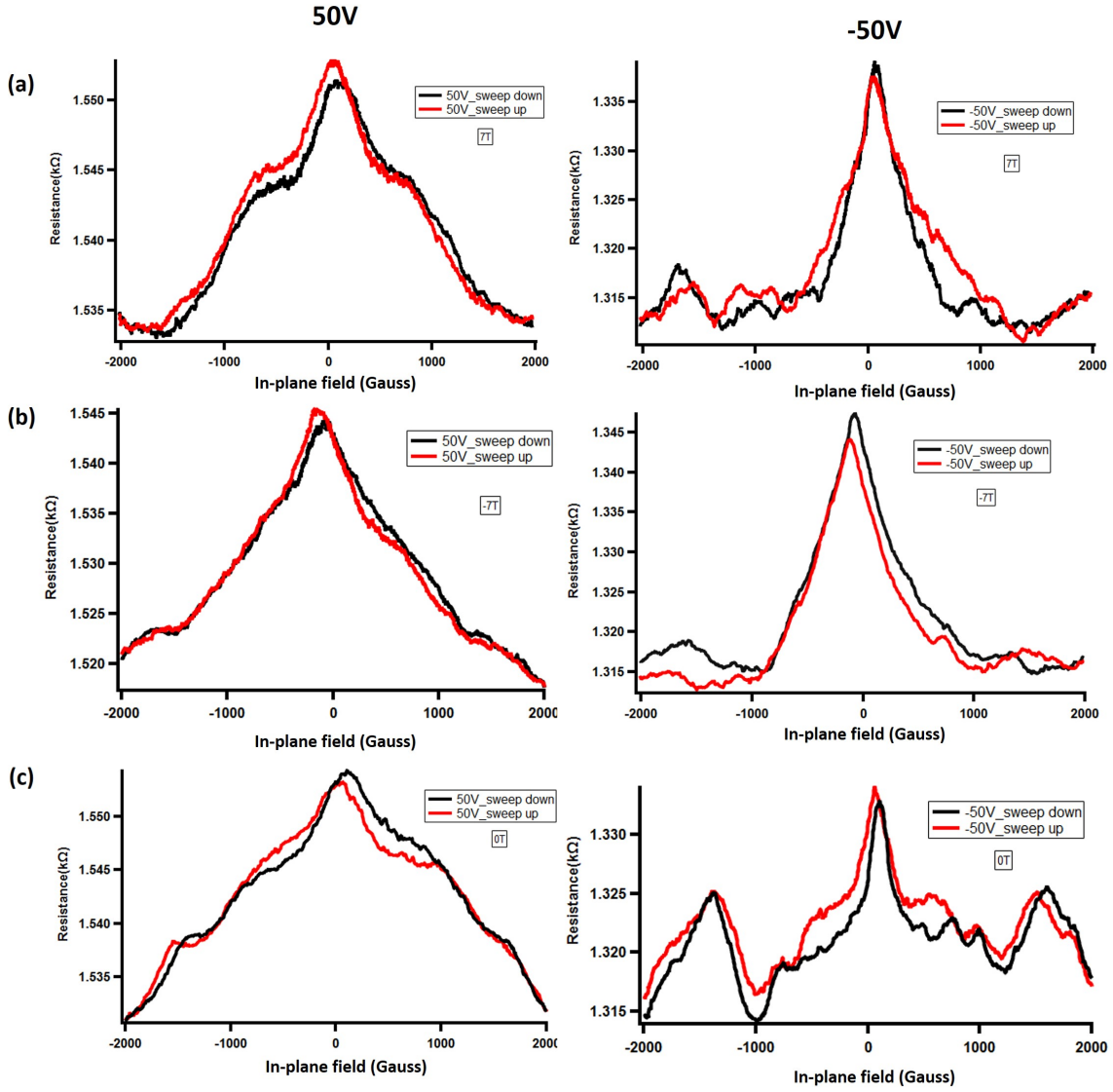


Fig. 5.3.4 Field asymmetry of applied in-plane field magnetoresistance in TCNQ coated sample at 200mK. (a) Heating and cooling temperature at 7T in-plane field, then sweeping in-plane field. Each up and down curve averages from 5 curves at 50V and -50V gate voltage. (b) Same measurement at -7T. (c) The same measurement was after warming and cooling at 0T. The observed asymmetry magnetoresistance at -50V gate voltage and its sensitivity to cooling conditions under the zero or large in-plane field suggests gate dependent magnetic domain.

## 5.4 Magneto-conductance in out-of-plane field at 200mK and 4K

In the applied out-of-plane field, we first show the result on a weak coupling sample, FeTPP grafted on graphene. Because the back gate suffers the leaking problem in this sample, thus we cannot apply gate voltage on this sample. Figure 5.4.1 (a) is the gate dependence before the leaking problem occurred, just to point out the 0V gate voltage in the hole doping area, still far from the Dirac point. Figure 5.4.1 (b) is magneto-conductance result in $\pm$7000G out-of-plane field at 0V gate voltage at 200mK and 4K. The weak localization is seen in 200mK (black curve), but it has been suppressed when we increase the temperature to 4K (red curve), which is a normal result since the sample is weak coupling between FeTPP molecular layer on graphene. When we increase temperature, the dephasing time $\tau_\phi$ decreases, which leads to the suppression of weak localization. Meanwhile, the phase coherence length is also decreased with increasing temperature.

In the TCNQ sample, fortunately, we can detect three different regions for comparison by applied gate voltage, shown in Figure 5.4.2 (a). First, we show the same magneto-conductance measurement as FeTPP/Graphene sample. At 0V gate voltage, the Dirac point in Fugyre 5.4.2 (b), one can see the weak localization has already been suppressed at low temperature 200mK because the lower carrier density can decrease the magneto-conductance by increasing the spin-flip scattering time $\tau_s$ [136]. Then, we observed the same temperature dependence, the weak localization and phase coherence length are decreased with temperature increasing from 200mK to 4K. We estimate $L_\phi$ from the width of the weak localization peak: $B_C \sim \frac{\phi_0}{L_\phi^2}$

Since the Dirac point is located at 0V gate voltage, we can compare the weak localization and phase coherence in electron and hole doping regions by applied gate voltage (30V and -30V), shown in Figure 5.4.3. The 5.4.3 (a) at applied 30V gate voltage shows the weak localization at 200mK is suppressed, and the phase coherence length $L_\phi$ just slightly increased when we increase the temperature. The result suggests the induced magnetic moments destroy and suppress the weak localization in the low field compared with the applied 30V gate voltage, the weak localization at -30V gate voltage is clearer, and the phase coherence length at 200mK is two times larger than the higher temperature at 4K. This result sounds surprising and contradicts results in the in-plane presented above, indicating frozen magnetic domains in the plane at negative gate voltage. Our results show that these frozen domains tend to reduce the spin-flip scattering rate, and therefore the phase coherence time is less affected.

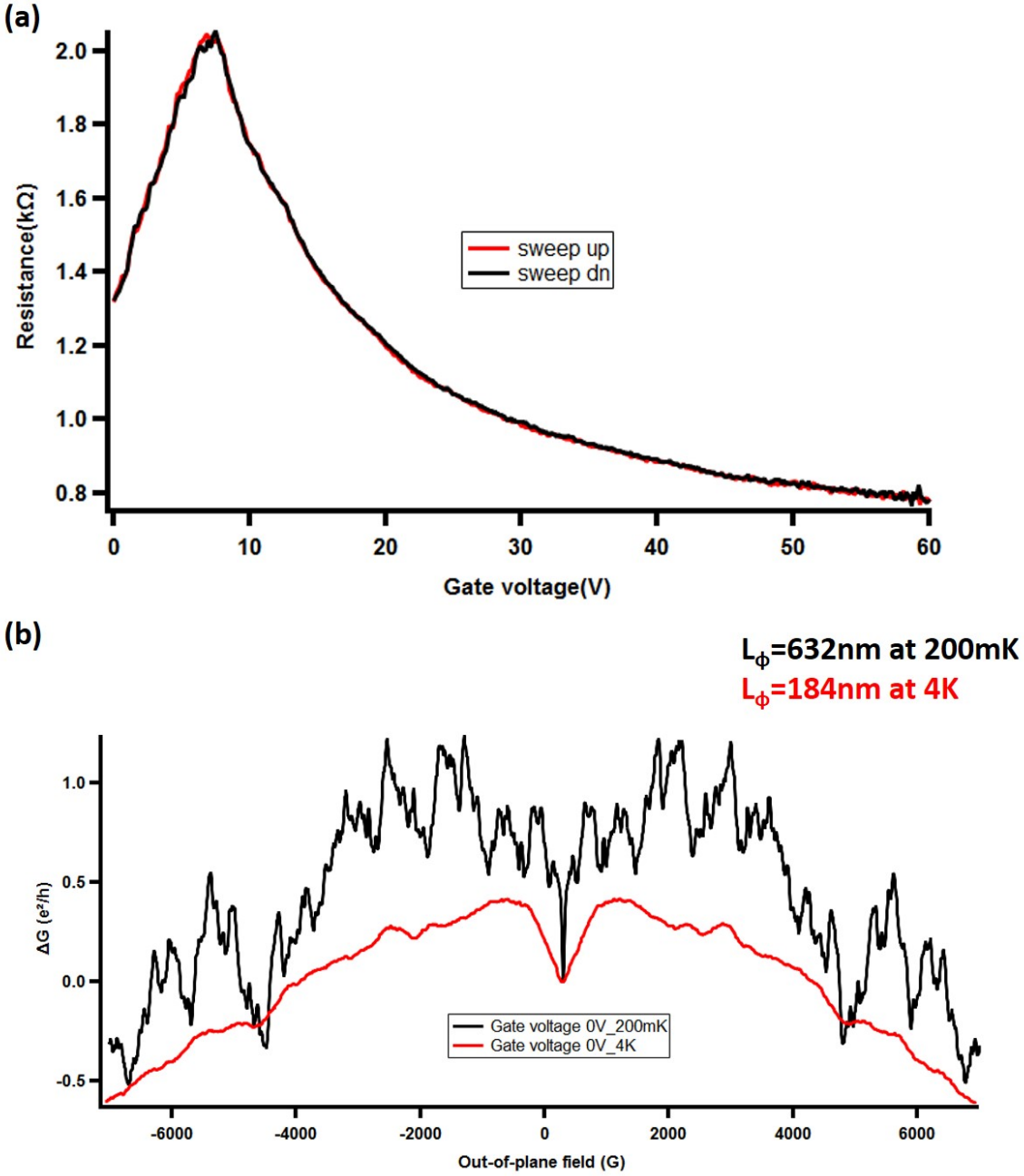


Fig. 5.4.1 (a) Gate dependence of FeTPP molecular layers grafted on graphene sample before the back gate leaking problem occurred. (b) Magneto-conductance result between ±7000G out-of-plane field at 0V gate voltage at 200mK and 4K. In the weak coupling sample (FeTPP/Graphene), the weak localization is clearly suppressed at 200mK, and the phase coherence length $L_\phi$ is decreased with temperature increasing.

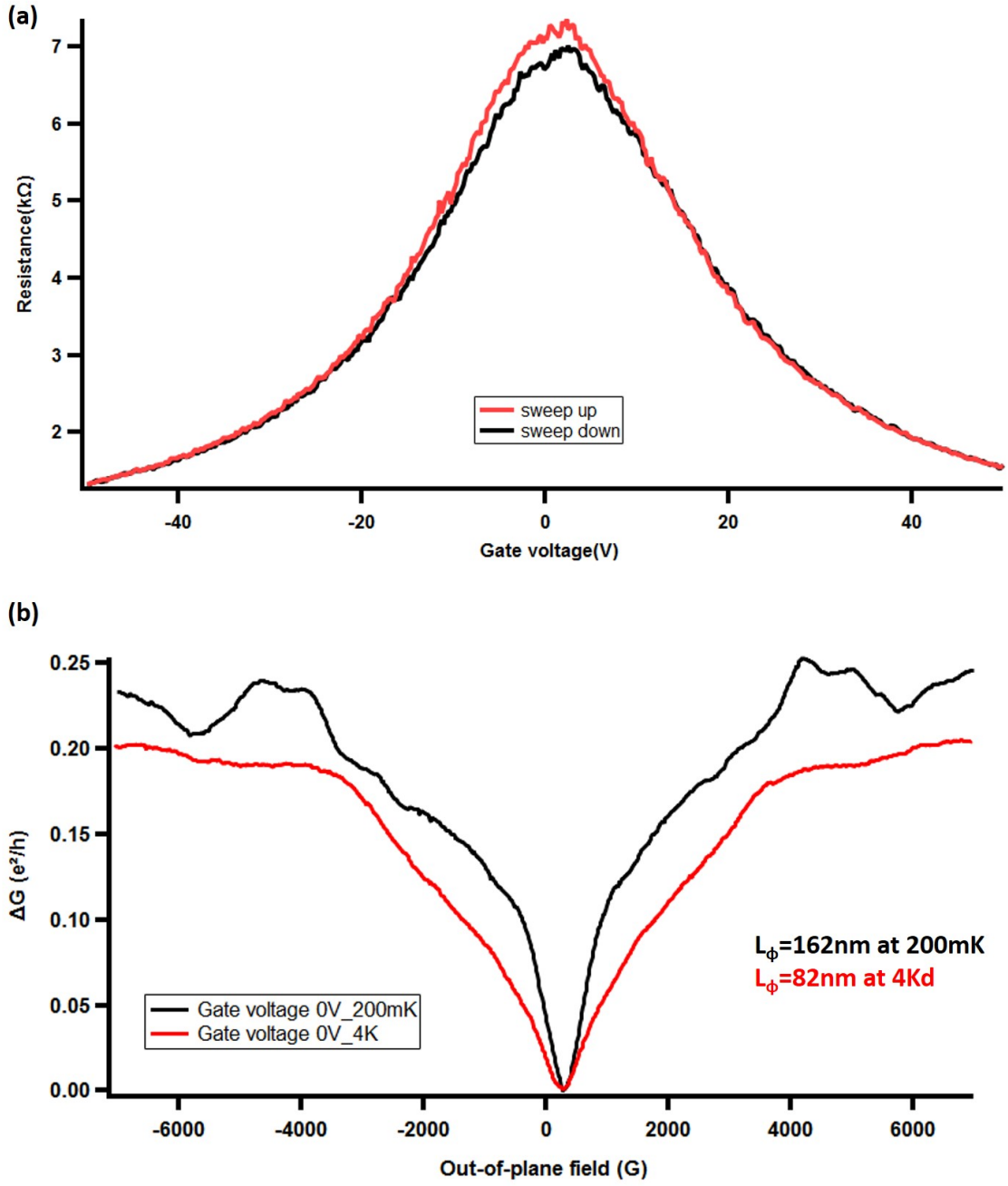


Fig. 5.4.2 (a) Gate dependence of TCNQ molecular layers grafted on graphene sample, the Dirac point is close to zero. (b) Magneto-conductance result in $\pm$7000G out-of-plane field at Dirac point 0V gate voltage at 200mK and 4K. In the stronger coupling sample (TCNQ/Graphene), the weak localization is clearly suppressed at the Dirac point. The phase coherence length $L_\phi$ is decreased with temperature increasing from 200mK to 4K.

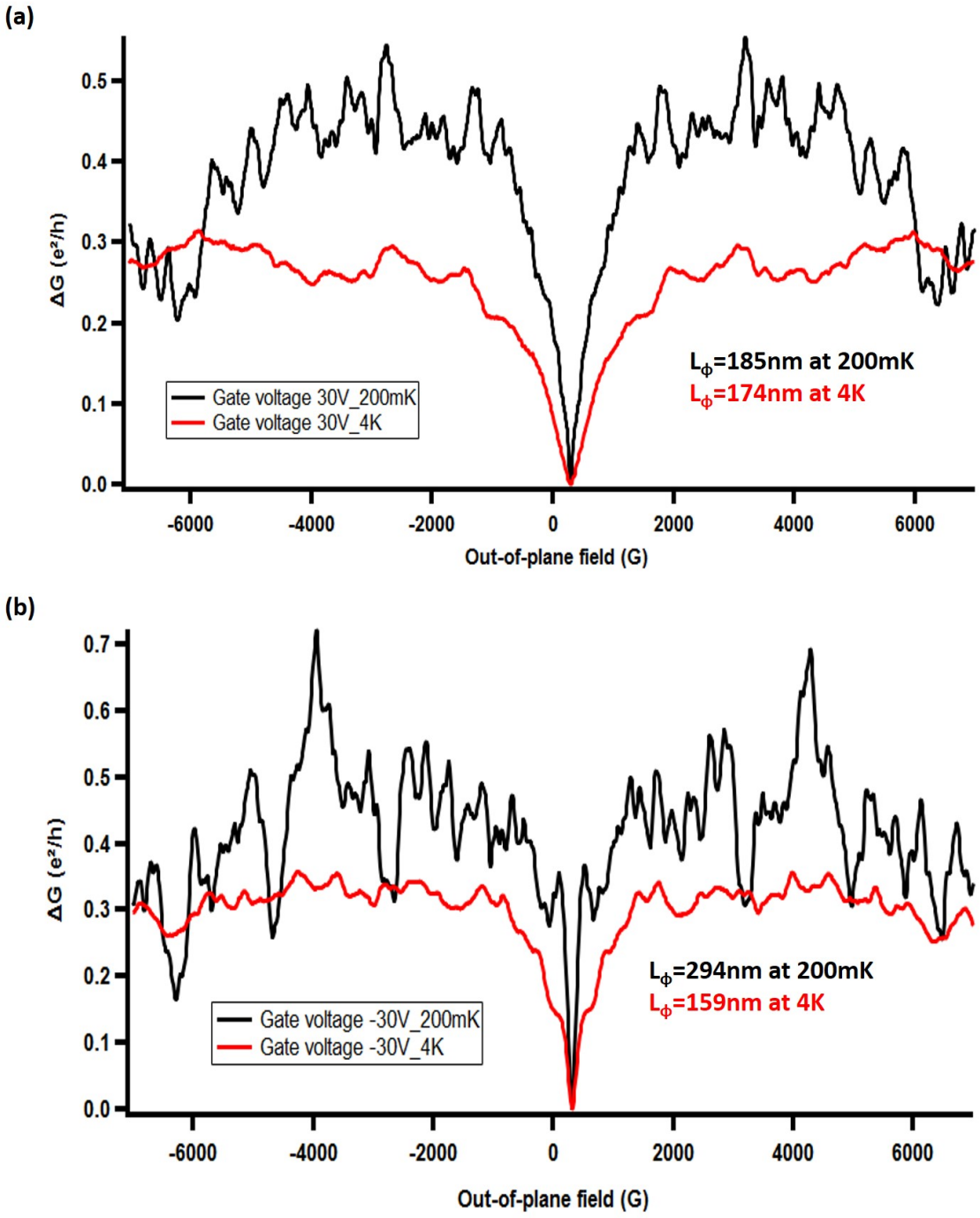


Fig. 5.4.3 (a) Magneto-conductance result in ±7000G out-of-plane field at Dirac point 30V gate voltage at 200mK and 4K. The weak localization is suppressed due to the induced magnetic moment on graphene by TCNQ molecular layer. The phase coherence length $L_\phi$ is decreased with temperature increasing from 200mK to 4K. (b) Same measurement at gate voltage -30V. The weak localization is suppressed due to the induced magnetic moment on graphene by TCNQ molecular layer. The phase coherence length $L_\phi$ is decreased with temperature increasing from 200mK to 4K.

## 5.5 Conclusion

The graphene coated with FeTPP magnetoconductance experiments show a significant increase of $L_\phi$ (by a factor of 3.4) when the temperature is decreased from 4K to 0.2 K, see Figure 5.4.1. This increase has the order of the $T^{-0.5}$ dependence expected when phase coherence is exclusively limited by inelastic electron-electron interactions, which indicates that Fe-porphyrins are not generating an important spin-flip scattering on conduction electrons in graphene. This absence of magnetic scattering is confirmed by conductance fluctuations of the order of 0.7 $e^2$/h at 200mK.

The situation is different for TCNQ molecules, where a smaller increase of $L_\phi$ is observed for both values of investigated gate voltages. This result may indicate the presence of magnetic scattering. Also, the magnetic scattering affects the amplitude of conductance fluctuations 0.1 $e^2$/h at gate voltage 0V, much smaller than 30V. The phenomenon is less clear at gate voltage -30V, where instead, in-plane magnetoresistance indicates the possible existence of frozen magnetic domains whose magnetization is aligned in the plane of the sample and does not contribute to spin-flip scattering. Concerning graphene coated with $TbPc_2$ molecules, we also show only a small increase in phase coherence length in Appendix.

# Chapter 6

# Single-molecule magnet $TbPC_2$ grafted on graphene

## 6.1 Introduction

In 2003, Naoto Ishikawa et al. published the synthesis of an innovative molecular compound in which a terbium atom is placed between two phthalocyanines, phthalocyaninato [137]. This novel compound behaves like a single molecule magnet(SMM) through one metal ion. Ever since single-molecule magnets (SMMs) have brought much attention over the past two decades due to their special magnetic property, compared with other polynuclear transition metal complexes [138, 139], these complexes display a well-defined magnetic anisotropy with larger barriers and pronounced hysteresis. Some properties, like interference effects between tunneling paths [140] and Quantum tunneling of magnetization [141], have been revealed in molecular clusters with a few magnetic atoms. In addition, controllable molecular structures can be achieved at low cost and high yield. Therefore, many SMM containing transition metals or rare earth atoms have been investigated.

Meanwhile, magnetic materials-based spintronics studies have led to significant progress in applications. These applications rely mostly on the magnetoresistive effect, like the observation of the giant magnetoresistance effect(GMR). In thin metallic film systems, when the thin non-magnetic interlayer is placed between two ferromagnetic films, the magnetization of adjacent ferromagnetic films can be aligned parallel or antiparallel based on the thin non-magnetic interlayer, resulting in the resistance change of the orientation of the magnetization. Nowadays, new paths toward spintronics application have developed alternative choices with different types of materials, replacing inorganic material with $\pi$-conjugated organic semiconductors [142]. Organic semiconductors have become an attractive candidate because

of the likely longer spin relaxation times [143] compared with transition metals, including some new properties. As a result, SMMs are promising candidates in the preservation of quantum coherence of the spin in spintronics applications and lead to the possibility of investigating the coherent manipulation of SMMs' spin state.

We are interested in a specific SMM in this work, the $TbPc_2$ double-decker in Figure 6.1.1. $TbPc_2$ comprises six unpaired electrons on the Tb ion with $4f^8$ in the inner shell and one unpaired electron on the nitrogen atom of the phthalocyanine ring that is directly connected with the Tb metal atom in the center. The metal ion is coordinated with an organic ligand to obtain an easy axis. Thus, strong spin-orbit coupling results in a total angular momentum of J = 6. Due to the strong magnetic anisotropy resulting from the interaction of two phthalocyanine (Pc) ligands, the magnetic moment of terbium possesses just two projections on the easy axis $J_z = \pm 6$. Moreover, the hyperfine interaction with the inner shell electrons is caused by the terbium's nuclear spin of 3/2. Thus, the SMM nuclear spin can detect through transport measurement and tuning the charge state of the ligand by applying gate voltage [32, 30, 144].

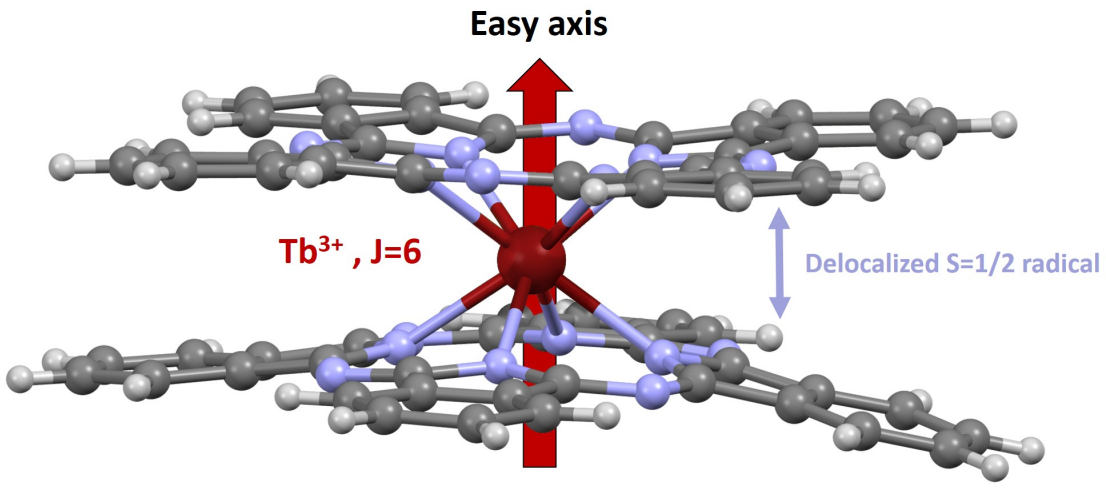


Fig. 6.1.1 Schematic illustration of a $TbPc_2$ SMM. A $Tb_{3+}$ ion (red color) has been sandwiched between two organic phthalocyanines (Pc) ligands. The $TbPc_2$ SMM behaves like an Ising-like spin system because of the strong anisotropic 4f shell of the $Tb_{3+}$ ion and strong spin-orbit coupling, leading to the high magnetic anisotropy and a ground-state doublet $J_z = \pm 6$. delocalized radical has been caused by the oxidation state of the $Tb_{3+}$ ion through the phthalocyanine planes.

The lanthanide single-molecule magnet (SMM) bis-phthalocyanine terbium(III) ($TbPc_2$) has been studied in the graphene nanoconstriction [28] and carbon nanotube [29] as a spin valve device. These devices showed strongly anisotropic hysteresis loops of the magnetoconductance when the easy axis of molecules is aligned along with the applied magnetic field. Anisotropic magnetoconductance signals have been found in other $TbPc_2$ molecular spin-valve devices [30, 31]. The sign and magnitude exchange interaction between the terbium ion and the delocalized conduction electrons over the phthalocyanine ligands of the molecule has been proven and probed in a spintronic configuration [32], EPR measurements [145] and ab initio multi-reference calculations [146]. These studies point to a ferromagnetic coupling result between the Tb(III) ion and delocalized radical spin -1/2 over the phthalocyanine ligands, offering the possibility of spintronic applications.

## 6.2 Device preparation

The monolayer graphene flakes are obtained in this work by the standard exfoliation method. In the meantime, the monolayer $WS_2$ sheet was made through a gold-assisted exfoliation technique, as explained in section 3.2. Then, the monolayer graphene was transferred to the clean p-doped silicon substrate with 285nm oxide (used as the back gate) by the PC dry-transfer method. Here, we prepare two different kinds of samples for measurement. The first sample is a pure graphene sample, and for the second, we placed a monolayer $WS_2$ flake as a substrate for the graphene ($WS_2$/Graphene) to induce strong SOI on graphene for comparison. On each sample, we deposited Ti/Au(5/100 nm) metal as contacts on the graphene sheets and patterned the device with the set of desired two-wire geometries. The sample size of $TbPc_2$ grafted graphene is 0.8um length * 4um width, and it's 0.8um length * 6um width of the $TbPc_2$ coated graphene/$WS_2$ sample.

Then, we deposited $TbPc_2$ SMMs on the prepared graphene samples at room temperature according to the following steps. First, the $TbPc_2$ molecule powder was dissolved in a dichloromethane (DCM) solution. The $TbPc_2$ SMMs powder was prepared by our colleague Stéphane Campidelli in CEA Saclay (method described in Appendix A). The mixture has a green color. Based on the molar concentration, the color can be changed from light green to relatively dark green. We deposited about $10ul$ drop of a $10^{-4}$M solution of $TbPc_2$ in DCM. Afterward, the solution entirely covered the graphene devices, and the DCM dried out, leaving behind only the $TbPc_2$ molecular layers precisely on the graphene device, as seen in Figure 6.2.1. From the previous study, The TbPc2 molecular layer has been proven to form ordered arrays on the graphene surface during the self-assembly process [147].

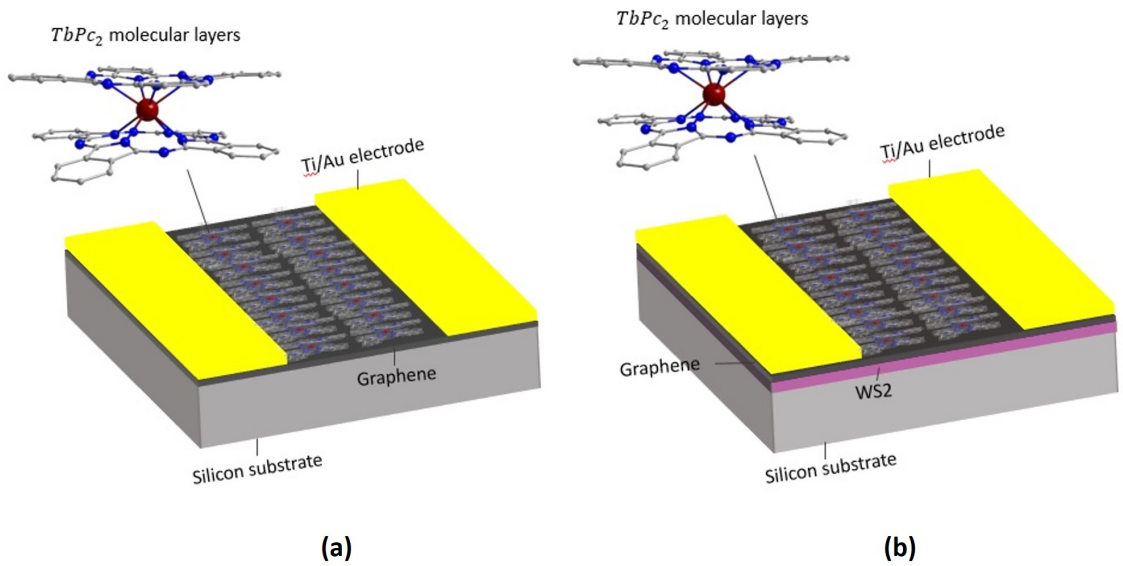


Fig. 6.2.1 Scheme of two graphene transistor samples (a) Monolayer graphene transistor coupled with $TbPc_2$ SMMs molecular layers. $10^{-5}$ M molar concentration $TbPc_2$ deposited on graphene by drop casting. (b) Monolayer graphene and $WS_2$ heterostructure transistor coupled with $TbPc_2$ molecular layers. $WS_2$ induced strong spin-orbit interaction on graphene.

Before drop casting the $TbPc_2$ molecule layer on graphene, we measured the gate dependence of the resistance between the back-gate voltage 10V at room temperature. After the drop casting, we did the same test of gate dependence of the resistance. The result shows a strong charging effect and reveals that the $TbPc_2$ molecules are strong electron acceptors. The charge can easily be transferred to the molecules sitting on the graphene by applying a gate voltage. Since the gate dependence or resistance result in Graphene/$TbPc_2$ and $WS_2$/Graphene/$TbPc_2$ samples having a similar behavior before and after drop-casting of the $TbPc_2$ molecular layers, we use Graphene/$TbPc_2$ sample as an example to describe the effect of the TbPc2 molecules grafted on graphene.

In Figure 6.2.2 (a), the Dirac point of the Graphene/$TbPc_2$ sample is located near 8V in the gate dependence of resistance measurement, which means the graphene is naturally p-type doped before grafted $TbPc_2$ in the ambient environment. At the Dirac point, the majority of carriers of graphene can be tuned to be electrons or holes, which means the majority of the carrier are electrons on the right side of the Dirac point, and the majority of carriers are holes on the left side of the Dirac point. After coating the graphene with $TbPc_2$ by drop casting, the Dirac point of the gate dependence of resistance has shifted farther to the right; see Figure 6.2.2 (b). First, this result shows that $TbPc_2$ is the strong electron acceptor for graphene, and graphene gains more holes as majority carriers after grafting. Therefore, we need to apply a higher back gate voltage to reach the Dirac point, adding more electrons into graphene in the gate dependence measurement to continually transfer the charges between the graphene and $TbPc_2$ molecular layers. Second, the clear hysteresis in Figure 6.2.2 (b) shows up after $TbPc_2$ deposition at room temperature. This result is probably related to the slow relaxation of the hopping processes between neighboring molecules [33, 34]. On the other hand, this phenomenon can be considered an indication of the artificial doping of graphene by transferring charges onto the molecules. In addition, We also notice that the hysteresis has disappeared (Figure 6.2.2 (c)) at 12mK; no charge transfer occurs between $TbPc_2$ and graphene.

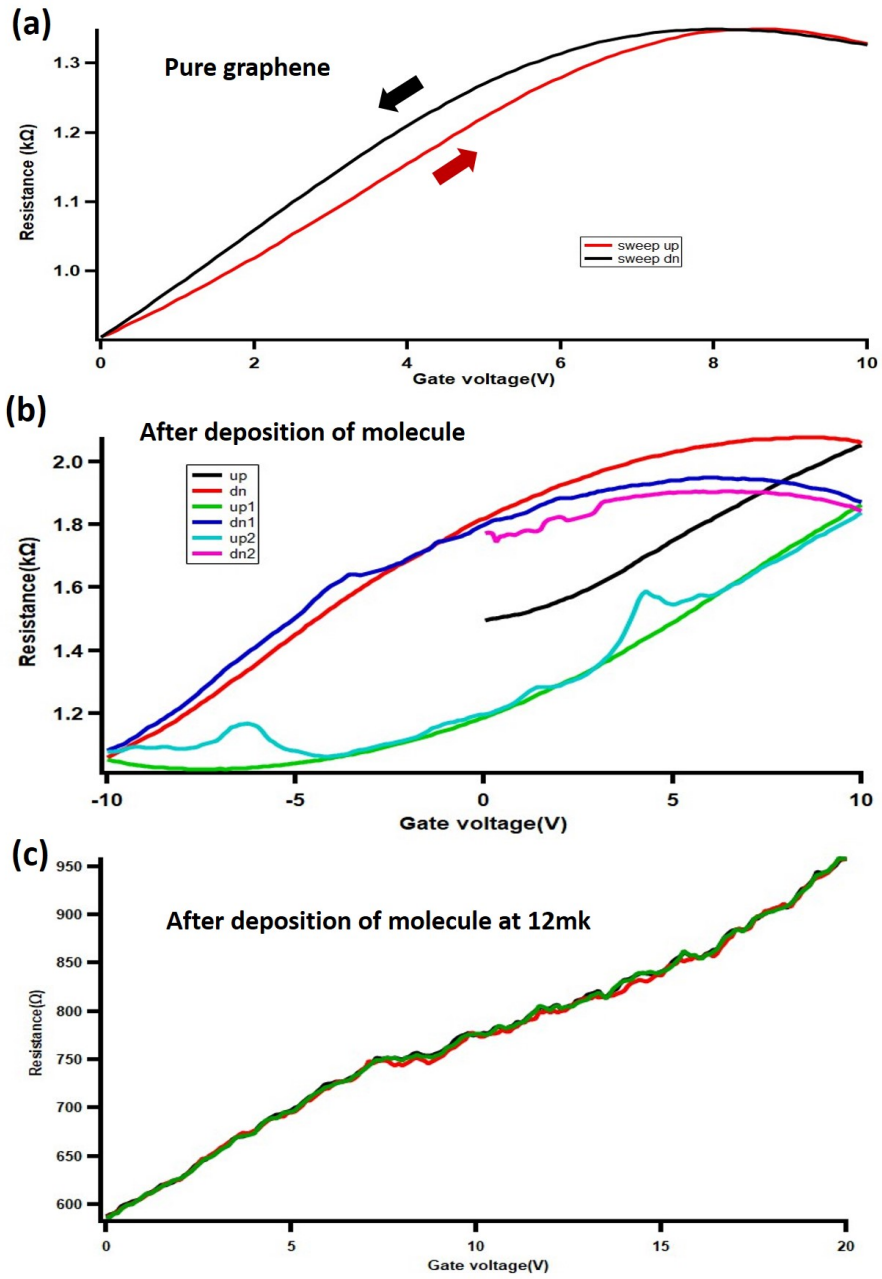


Fig. 6.2.2 Gate dependence measurement applying the back-gate voltage between $\pm$10V. The gate dependence in Graphene/$TbPc_2$ and $WS_2$/Graphene/$TbPc_2$ samples have a similar behavior before and after the drop-casting of molecular layers. Here, we use Graphene/$TbPc_2$ sample as an example to illustrate the effect after the deposition of $TbPc_2$ molecules. (a) Before $TbPc_2$ molecules, drop-casting (b) After $TbPc_2$ molecules drop casting at room temperature, the back-gate voltage is swept forward/backward several times, and the result shows hysteresis due to the charge transfer process between graphene and $TbPc_2$. (c) After $TbPc_2$ molecules drop-casting at 12mK, the hysteresis has disappeared, implying no more charge transfer between $TbPc_2$ and graphene.

## 6.3 Magnetoresistance

**Applied out-of-plane field**

To start with, we have measured two independent graphene samples with Ti/Au contacts at 12mK, Graphene/$TbPc_2$ and $WS_2$/Graphene/$TbPc_2$ samples, which have been covered by $TbPc_2$ molecular layers in order to induce the magnetism on graphene in their magnetic moments. The $WS_2$/Graphene/$TbPc_2$ has strong induced spin-orbit interaction on graphene [11]. Both samples were measured simultaneously between $\pm$3000 Gauss(G) at 12mK while applying a gate voltage of 20V, the magnetoresistance in the out-of-plane field for both samples exhibits irreproducible magnetoresistance in the forward sweep and backward sweep, because the $TbPc_2$ induced magnetic moments on graphene that changed the interferences between the coherent trajectories across the samples, as seen in the Figure 6.3.1. The most intriguing feature is that the higher degree of noise shows up when the applied field is close to zero for both samples. We relate this higher degree of noise close to zero field due to magnetic relaxation processes with time scales of the order of records compatible with the time constant of the measurements. These are due to the $TbPc_2$-induced magnetic moment on graphene. However, the excess noise observed at the low field is absent at 3000G. Also, all curves are asymmetric functions of the magnetic field, as expected in the two-probe measurements in the presence of the time-reversal symmetry breaking due to the induced magnetic moment on graphene [27].

In Figure 6.3.2, we changed the gate voltage to 0V on both samples to see the difference. The magnetoresistance reveals the same features as applied with a 20V gate voltage, like the irreproducible magnetoresistance, the asymmetry curve, and the excess noise around zero fields are observed. But all the features are smaller in size at 0V gate voltage. We noticed that there are no clear weak localization peaks and the amplitude of the UCF is small compared to the quantum conductance. This contrasts with the observation of a larger doping regime in appendix A, where the behavior is more similar to what is shown in chapter 5.4.

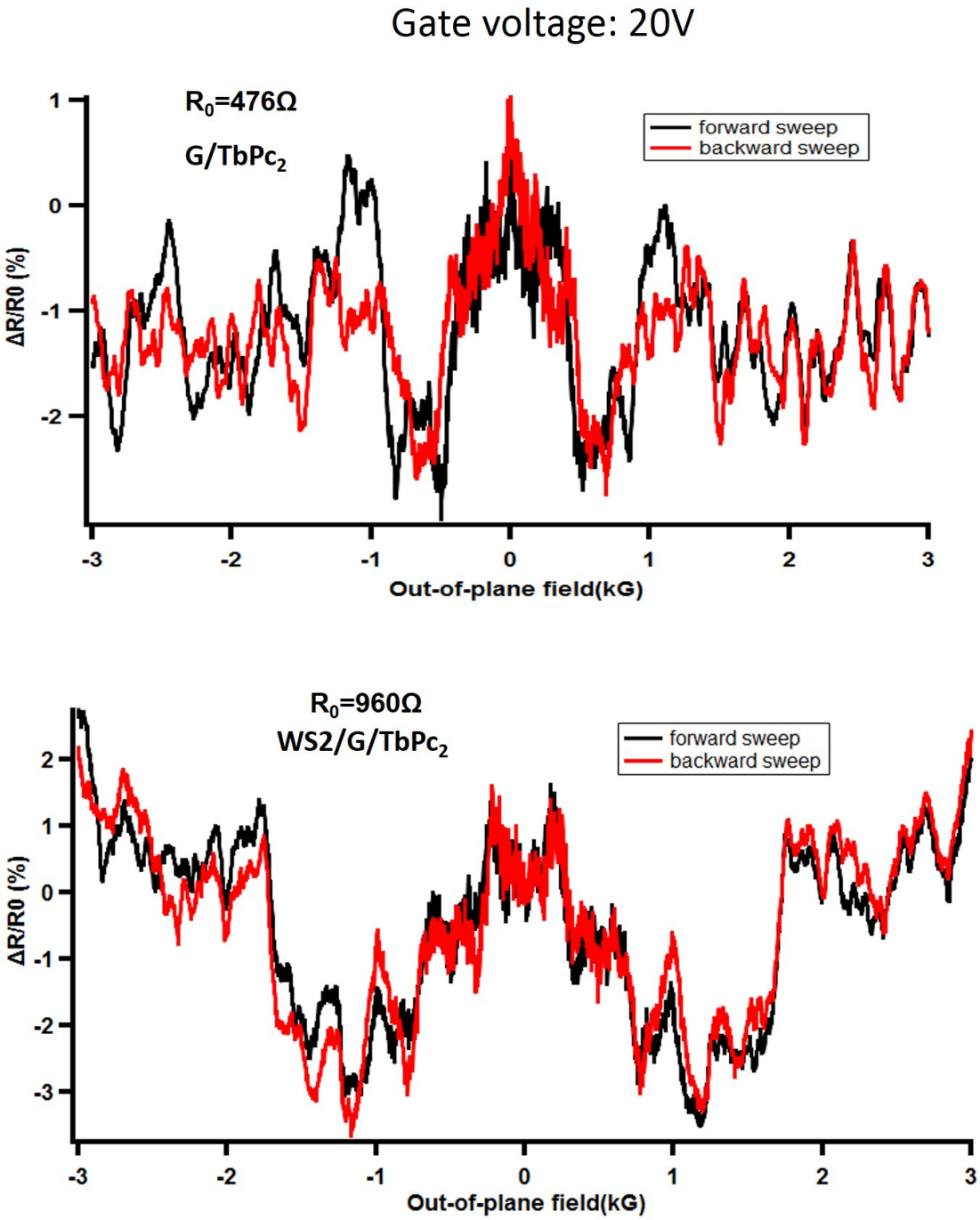


Fig. 6.3.1 Graphene/$TbPc_2$ and $WS_2$/Graphene/$TbPc_2$ samples in the out-of-plane field between $\pm$3000G with applying a 20V gate voltage at 12mk. A higher degree of noise shows up when the applied field is close to zero in both samples.

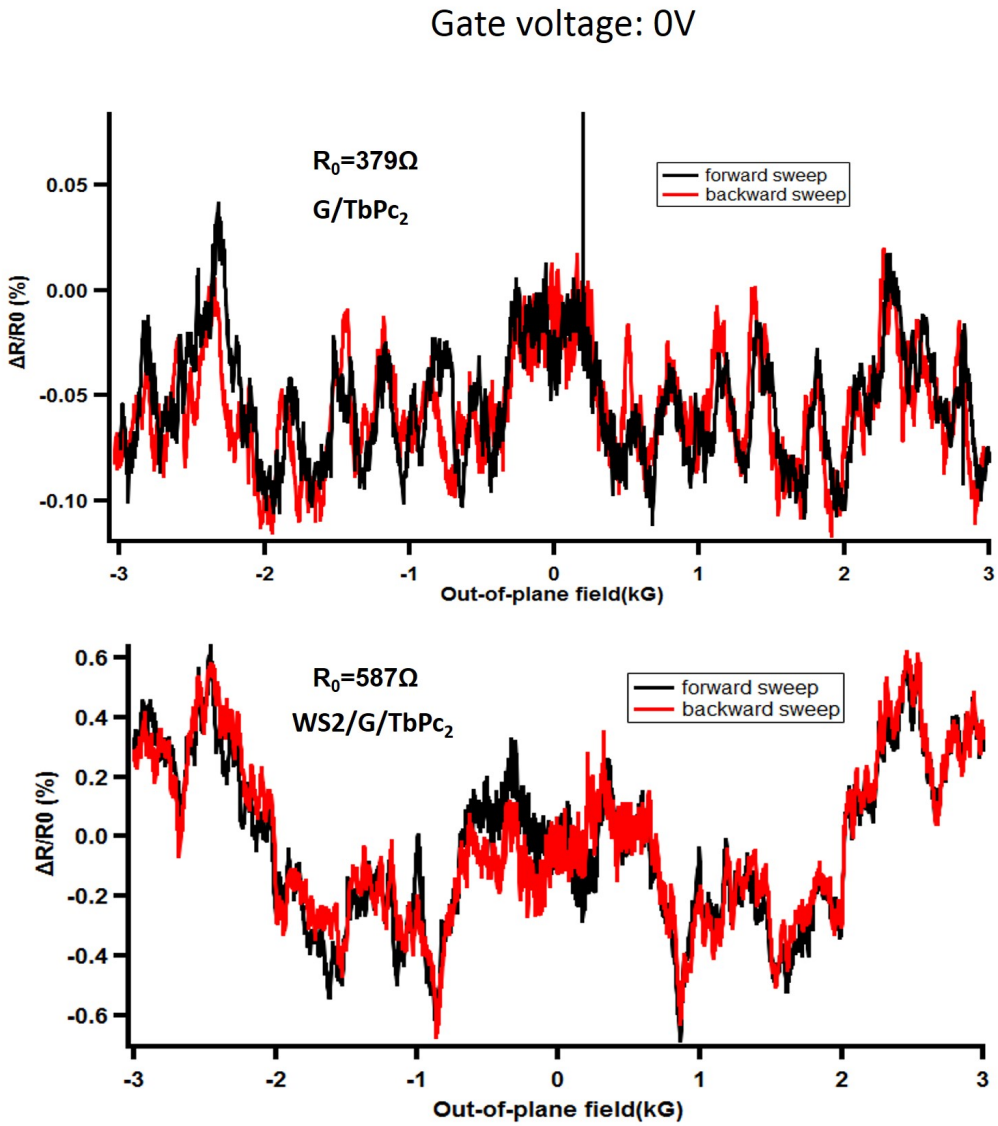


Fig. 6.3.2 Same measurement as Figure 6.3.1 but without applied gate voltage. A higher degree of noise appears when the applied field is close to zero in both samples, but the effect is smaller than applying a 20V gate voltage.

In the following measurements, we record 100 points during 3 mins for each value of the field. The excess noise around the zero fields is now very clear at the low field compared to the high field in Figure 6.3.3 (a). Through this method, the effect of the magnetic moment-induced excess noise in a low field can be quantized and visualized, as seen in Figure 6.3.3 (b). The magnetoresistance measured while waiting 3 mins staying at a given field led to a clear visualization of excess noise between the low field and higher field.

The next question is how to quantify the different degrees of excess noise between low and higher fields. The variance in statistics can be a useful tool to show the different degrees of noise at various out-of-plane fields. Variance is a measure of dispersion which means it is a measure of how far a set of numbers is spread out from their average value $\delta R^2 =< |R- < R >|^2 >$. In the Figure 6.3.4, the red curve represents the variance of the resistance of noise extract from the black curve. The resistance of excess noise in the low field is now more explicit than in the higher field.

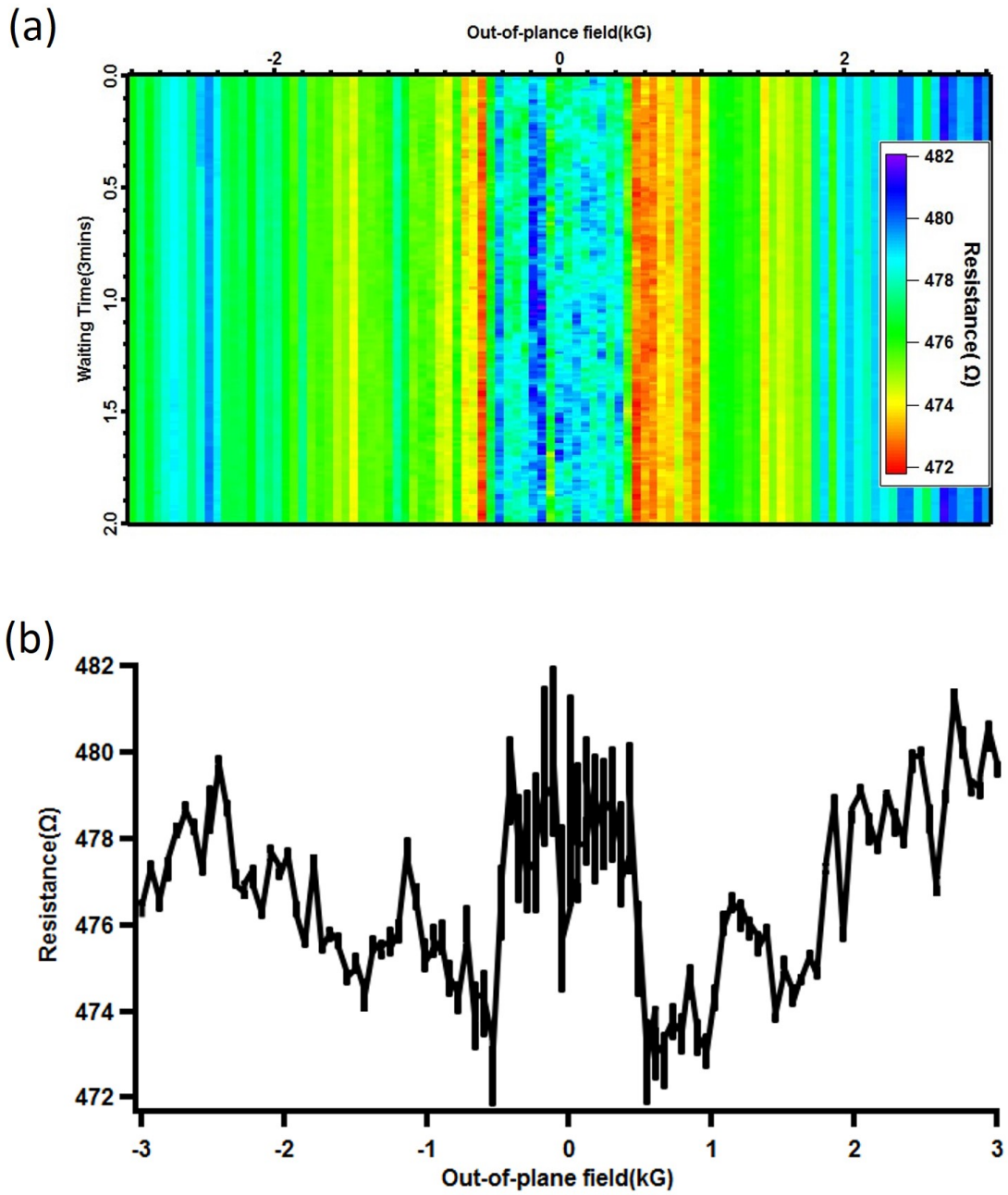


Fig. 6.3.3 (a) Graphene/$TbPc_2$ sample at gate voltage 20V during a sweep of out-of-plane field between $\pm$3000G as an example. In this measurement, we record 100 points during 3 mins in X-axis for each value of the field. (b) The degree of noise fluctuation around the zero fields is very clear after averaging from the result.

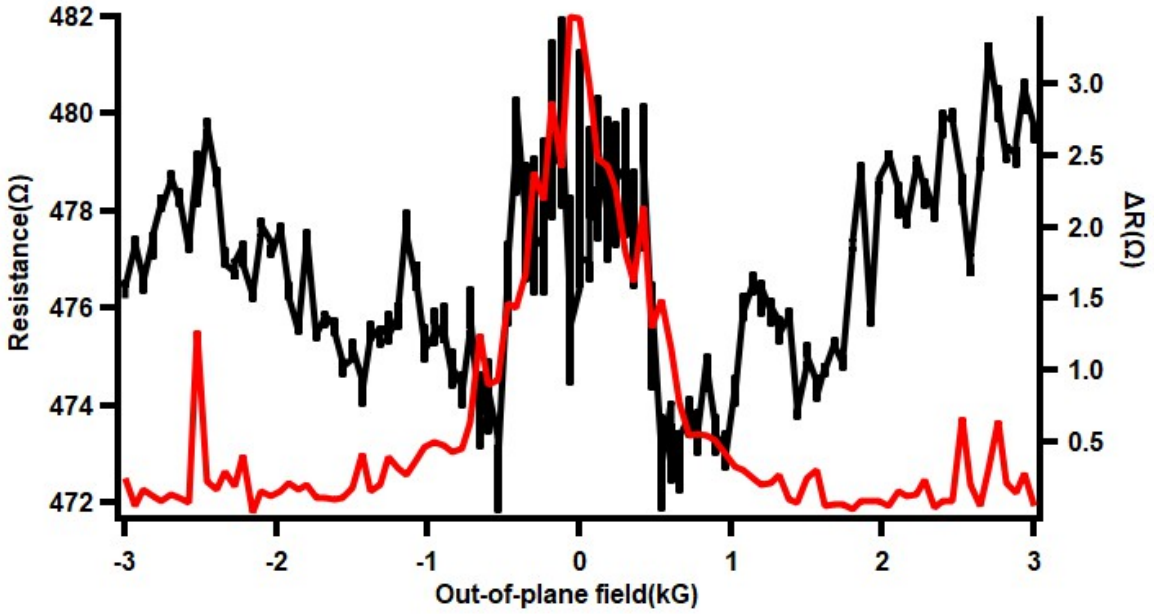


Fig. 6.3.4 Black curve is magnetoresistance while waiting 3 mins staying at a given field, and the red curve represents the variance of the resistance of noise.

### Variance of resistance fluctuations

One can quantify magnetic noise with the variance of resistance fluctuations $\Delta R^2$ between low and high fields. We looked at the gate dependence in each sample. Unfortunately, we could not reach the Dirac point for the Graphene/$TbPc_2$ sample until an applied 80V gate voltage in Figure 6.3.5 (left). However, in the $WS_2$/Graphene/$TbPc_2$ sample, the Dirac point is located close to 55V applied gate voltage, so we can compare $\Delta R^2$ ffor holes (left side of Dirac point) and electrons(right side of Dirac point) in Figure 6.3.5 (right).

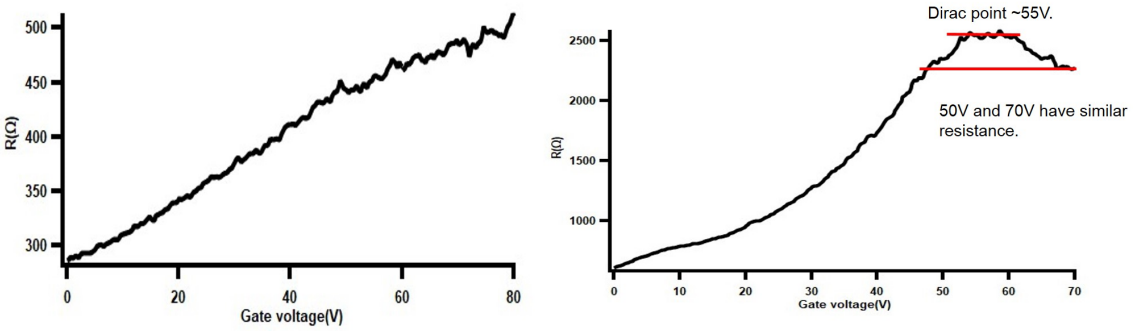


Fig. 6.3.5 Gate dependence of Graphene/$TbPc_2$ sample (left) and $WS_2$/Graphene/$TbPc_2$ sample (right). For the Graphene/$TbPc_2$ sample, we can't reach the Dirac point and stop at 80V. For the $WS_2$/Graphene/$TbPc_2$ sample, the Dirac point locates close to 55V, and we're able to compare the variance of noise when the majority of the carrier are holes or electrons.

Afterward, the variance of resistance noise was determined at different applied gate voltages for both samples. Firstly the magnetic moment-induced noise fluctuation in the low field increased with the applied gate voltage in the Graphene/$TbPc_2$ sample. See Figure 6.3.6 (a). The degree of magnetic-induced excess noise looks rather small at 0V and 20V at zero fields, but the degree of excess noise turns out to be quite clear at higher applied gate voltage until 70V in the low field regime. In the meantime, the $WS_2$/Graphene/$TbPc_2$ sample reveals the largest resistance variance of noise fluctuation in the low field when the applied gate voltage is close to the Dirac point. What is more interesting is that the $WS_2$/Graphene/$TbPc_2$ have similar resistance at gate voltage 70V and 50V, yet the variance at 70V is much smaller than at 50V.

We also investigated the temperature dependence of the noise for both samples at the gate voltage with the highest resistance variance, as seen in Figure 6.3.7. The Graphene/$TbPc_2$ sample at 70V exhibits a decrease of variance in the resistance noise. The magnetic moments' thermal activation rate increases as the temperature increases from 10mK to 200mK. The same behavior is observed for the other sample at 55V.

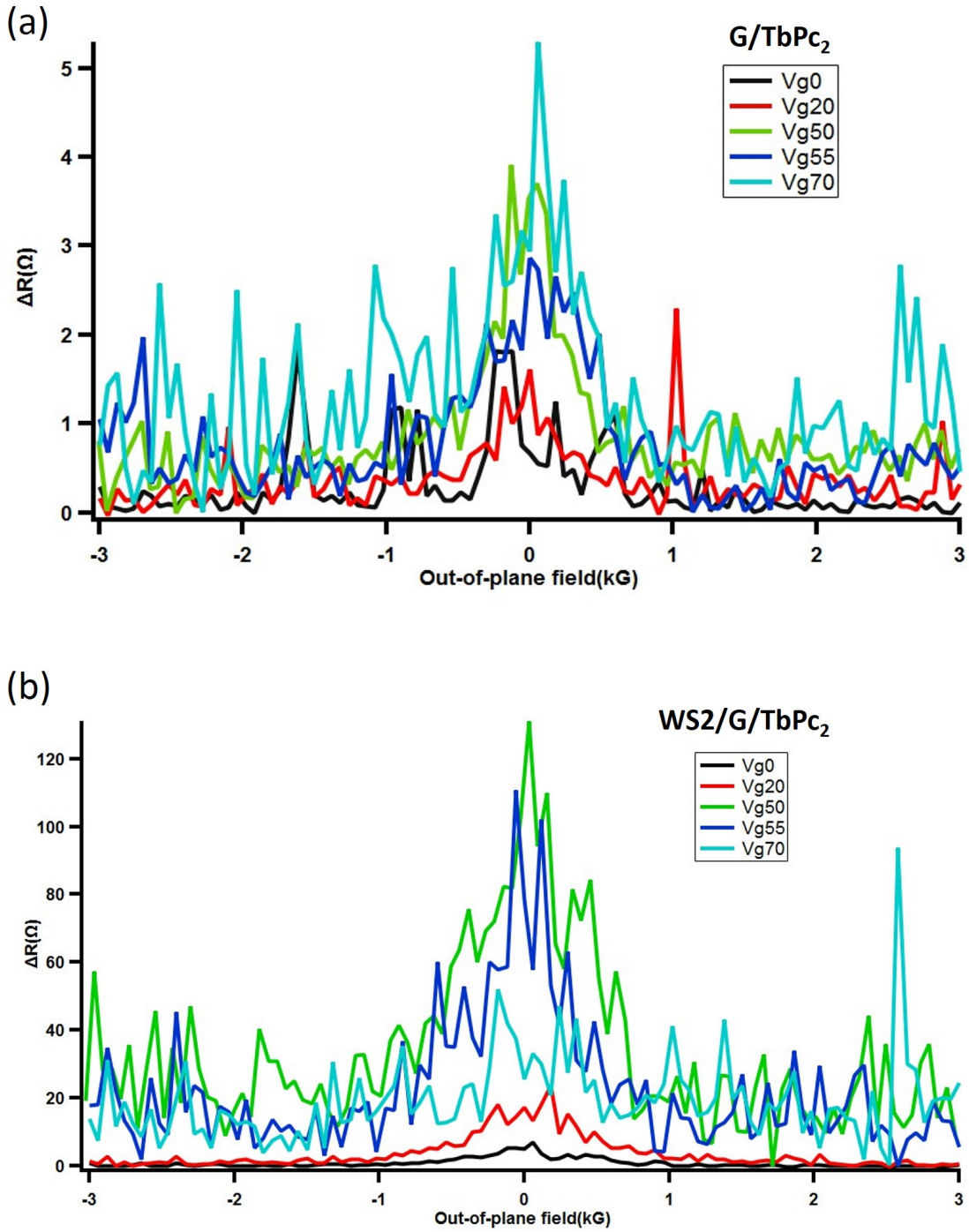


Fig. 6.3.6 (a) All the curves have been shifted for comparison. The variance of noise fluctuation is clearer with increasing applied gate voltage. (b) All the curves have been shifted for comparison. When the gate voltage is close to the Dirac point, the variance of noise fluctuation is larger.

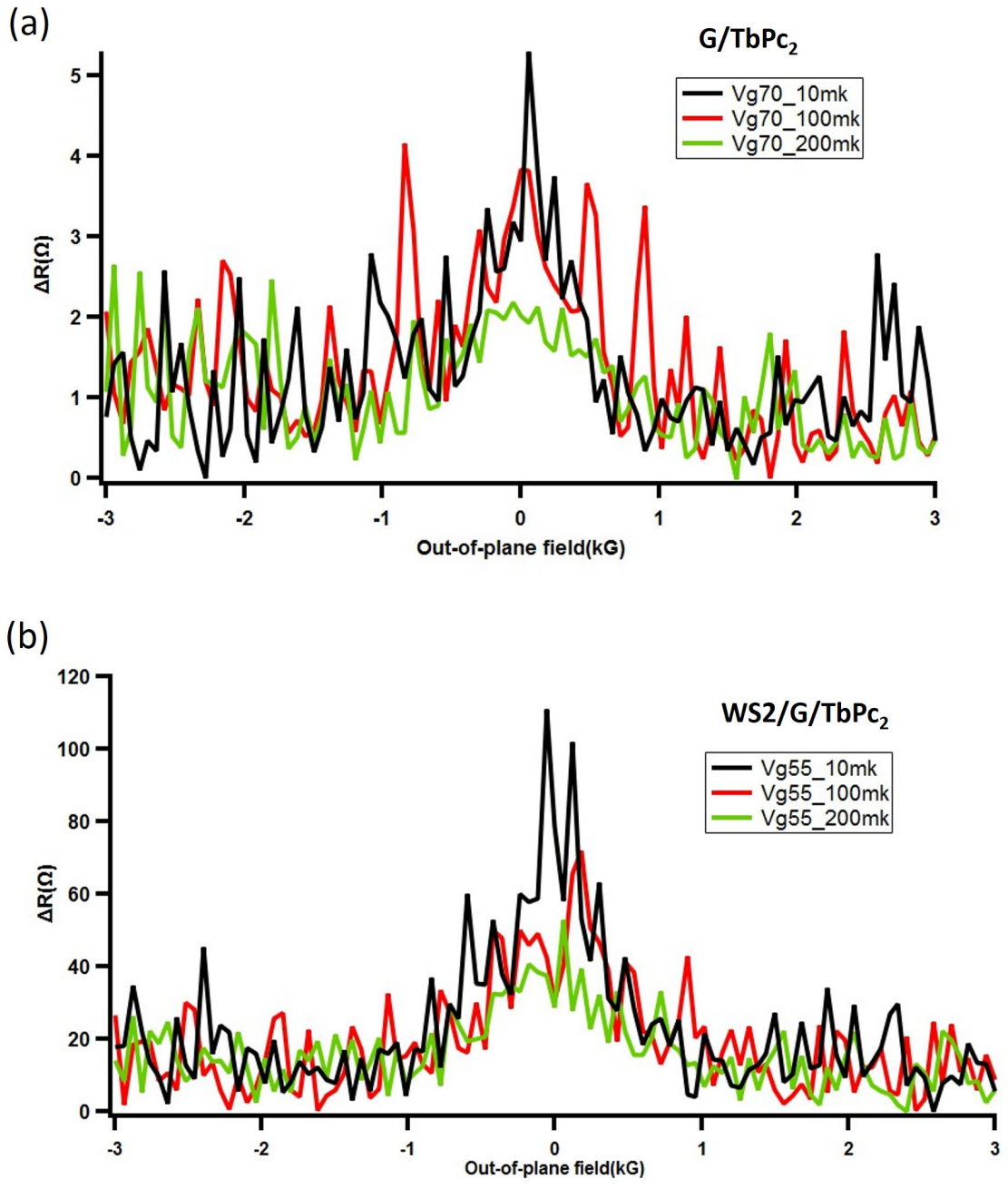


Fig. 6.3.7 (a) Temperature dependence of the variance of noise fluctuation at gate voltage 70V. (b) Temperature dependence of the variance of noise fluctuation at gate voltage 55V.

## 6.4 Low frequency 1/f noise

Previous magnetoresistance results display a magnetic field-dependent noise highest at low temperatures and low fields. In order to quantize the magnitude of noise, we acquire the output signal fluctuations from Lock-In Amplifiers in time and compute the noise spectrum by Fourier transform [35]. A noise spectrum with a 1/f dependence suggests the existence of a broad distribution of two-level systems with a wide distribution of field-dependent spin relaxation times, as seen in Figure 6.4.1.

$$\tau = exp(\frac{E_B}{k_B T}) \tag{6.4.1}$$

Where $E_B$ is the energy barrier, as in Figure 6.4.1, this points to anisotropic Ising-like fluctuating magnetic moments whose characteristic average energy barrier decreases with an out-of-plane magnetic field.

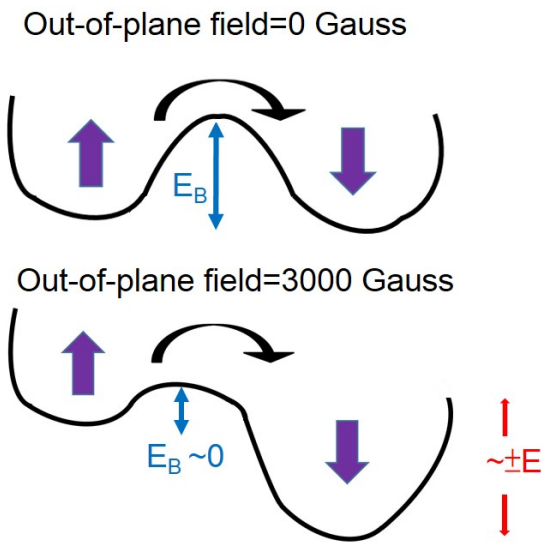


Fig. 6.4.1 Magnetic two-level system at zero fields and 3000 Gauss. $E_B$ is the anisotropy magnetic barrier energy, and the barrier decreases with an applied magnetic field.

We measured the noise spectrum in both samples at the applied 55V gate voltage, which is the Dirac point for the $WS_2$/Graphene/$TbPc_2$. The last sample exhibits the largest resistance variance of fluctuation, as shown in Figure 6.3.6 (b). We computed the noise spectral density of the resistance data between 0.001 and 10Hz at different temperatures from 10 mK to 300 mK, seen in Figure 6.4.2 (a) and (b). First and foremost, almost all data can be fitted with a 1/f curve. We attribute this 1/f noise to the presence of a large distribution of magnetic molecular clusters behaving as a two-level system with a magnetic anisotropy barrier due to the anisotropy field aligning with the molecular Tb spin perpendicular to the graphene layer. However, when the temperature reaches 300mK in the Graphene/$TbPc_2$ sample, the noise spectral density deviates from the 1/f behavior. Besides, the noise magnitude increases at low temperatures due to the increase of universal conductance fluctuations, which appears at low temperatures.

As discussed above, we also have 1/f behavior in the experimental spectra with different applied gates voltage and magnetic fields, shown in Figure 6.4.3 by the green and red curves. The noise spectral density deviates from the 1/f behavior at the 3000G magnetic field. This result proposes that a magnetic field reduces the magnetic barrier energy. The spin can more easily flip so that time scales become too short and are not accessible in our experiment.

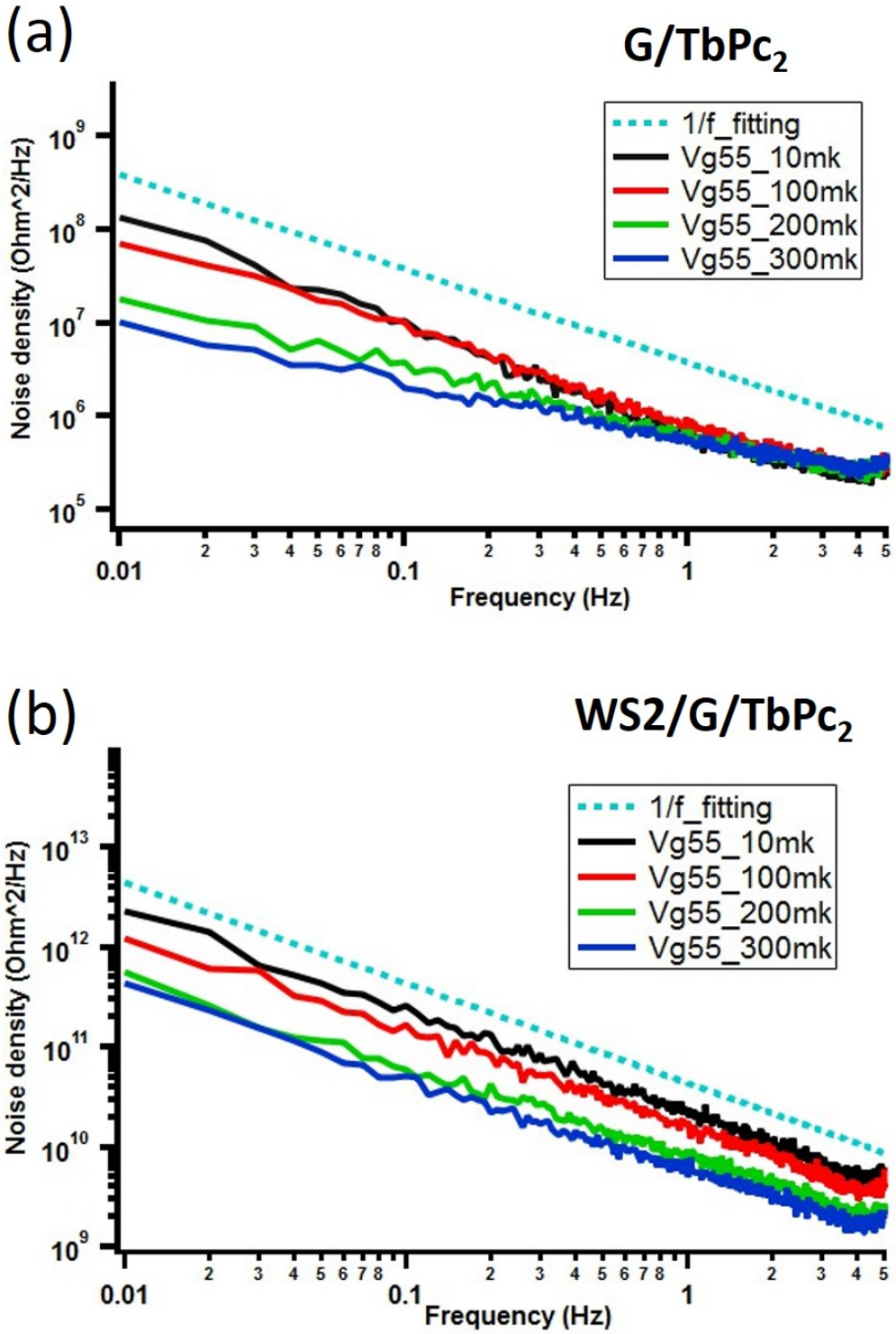


Fig. 6.4.2 (a) 1/f fitting of experimental results of Noise spectral density at different temperatures. The noise magnitude increases at low temperatures. (b) Same measurements with (a). The noise magnitude increases at low T due to the increase of UCF, which rise at low T.

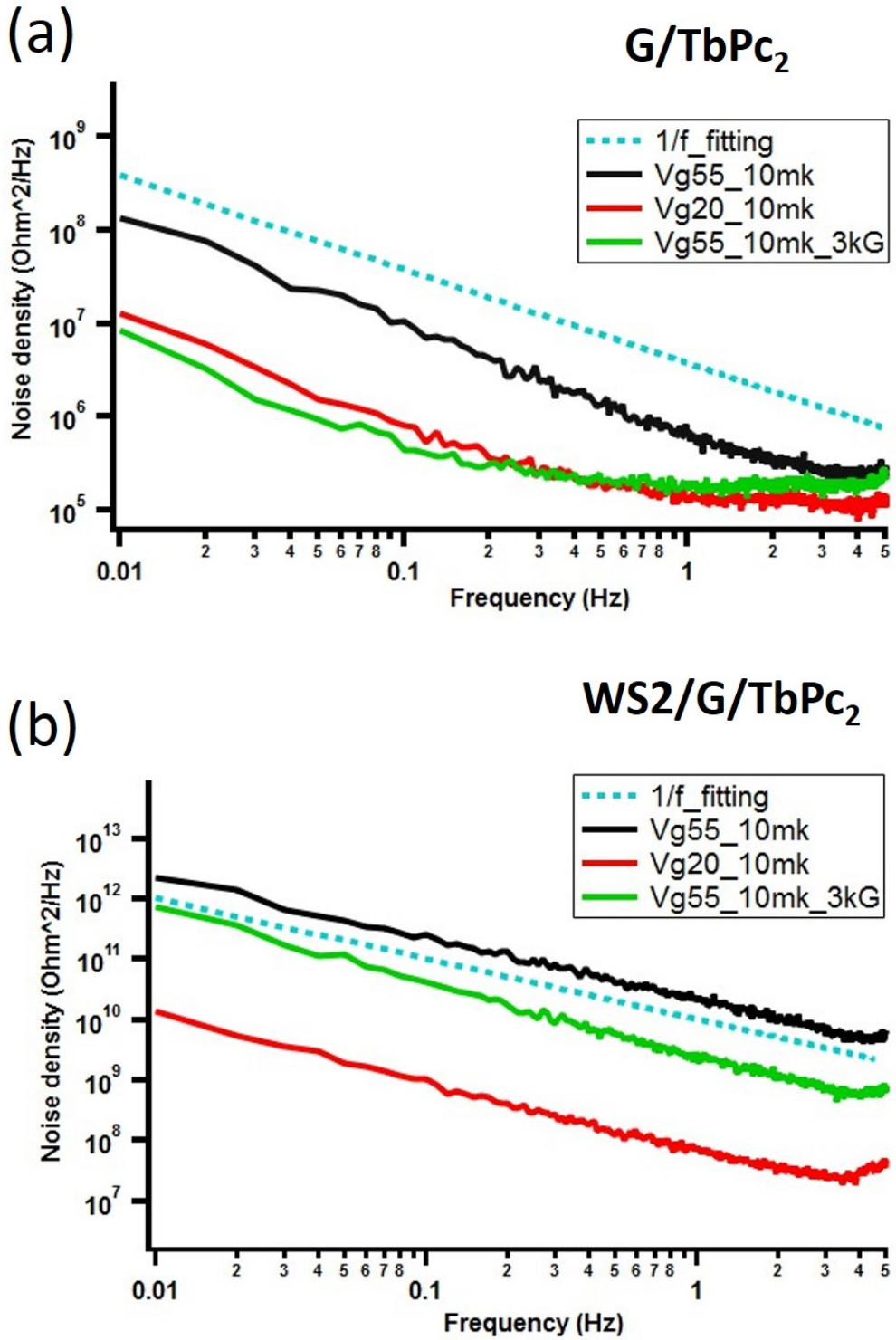


Fig. 6.4.3 (a) 1/f fitting of experimental results of Noise spectral density at different temperatures. The noise magnitude increases at low temperatures. (b) Same measurements in $WS_2$/Graphene/$TbPc_2$ sample.

## 6.5 Supplementary measurement

**Magneto-resistance in the in-plane field**

We have also characterized the same G/$TbPc_2$ and $WS_2$/G/$TbPc_2$ samples in the in-plane field. The applied magnetic field was parallel or antiparallel to the current during the sweeping in-plane field. It's important to mention that the magnetization of $TbPc_2$ bulk crystals exhibits thermal activation or tunneling across an anisotropic barrier on Ising-type anisotropy. Ising-type anisotropy. Also, the spin of molecules flips at zero field and phonon-assisted transitions. Those features have also been observed on the TbPc2 monolayer by XMCD measurements [148–150]. The conductance hysteresis loops have been observed in a $TbPc_2$ grafted carbon nanotube as a function of the in-plane magnetic field with strong uniaxial anisotropy response to the angle of the applied in-plane field [151]. We have also observed field hysteresis at the low temperature of the $WS_2$/Graphene/$TbPc_2$ sample in Figure 6.5.1 at Dirac point.

In section 6.3, the $WS_2$/Graphene/$TbPc_2$ sample reveals the largest resistance variance of noise fluctuation in the low field when the applied gate voltage is close to the Dirac point at 12mK, so we started the measurement at the Dirac point region, as seen in the Figure 6.3.5. The magnetoresistance curve of two samples obtained at a fixed back gate voltage of 55V for the field applied in the graphene plane. The effects of the molecule grafting on the graphene device are visible and reveal the hysteresis loop on $WS_2$/Graphene/$TbPc_2$ sample in the Figure 6.5.1 (b). Since the applied voltage 55V is still far from the Dirac point in Graphene/$TbPc_2$ sample, the magnetoresistance in the sweeping in-plane field does not display a clear hysteresis loop. In the sweep starting from -4000G to 4000G (black curve), the magnetoresistance has initially increased and reached the maximum value, and then it abruptly drops when the applied field is about to cross zero fields. The symmetric behavior is observed with the magnetic field swept in the opposite direction (red curve). The main features are reproducible in Figure 6.5.1 at two up-sweep and two down-sweep curves.

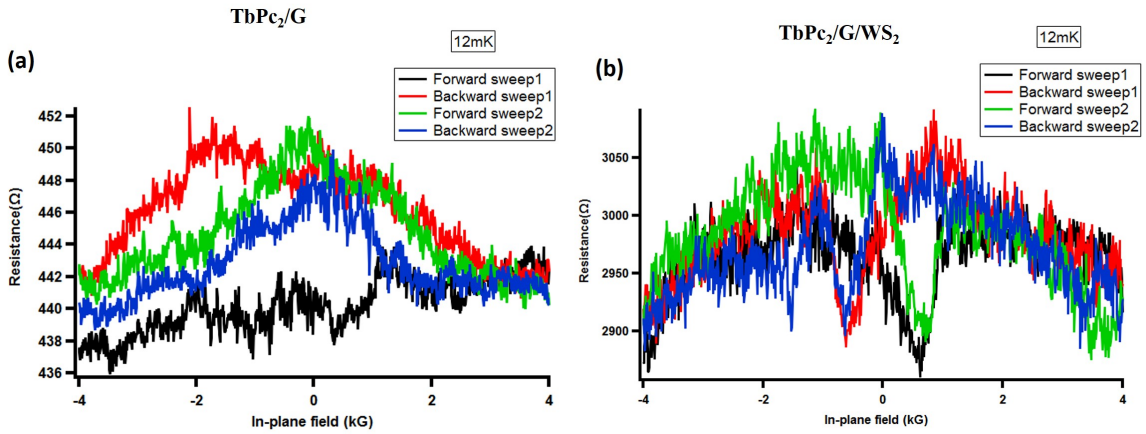


Fig. 6.5.1 The magnetoresistance of G/$TbPc_2$ by sweeping in-plane magnetic field four times between $\pm$4000Gauss at 12mK. (b) Same measurement in $WS_2$/G/$TbPc_2$ sample.

However, from these very low-temperature data, we cannot conclude the magnetic origin of this hysteresis. On the other hand, a thermal origin is more likely, as explained below. The temperature of the dilution fridge measured during the experiment also exhibits hysteresis in the same range of magnetic field corresponding to the superconducting/normal transition region of tin-lead solder. It is worth noting that this hysteresis disappears when increasing the temperature to 400mK. Meanwhile, the hysteresis was not observed on G/$TbPc_2$ sample.

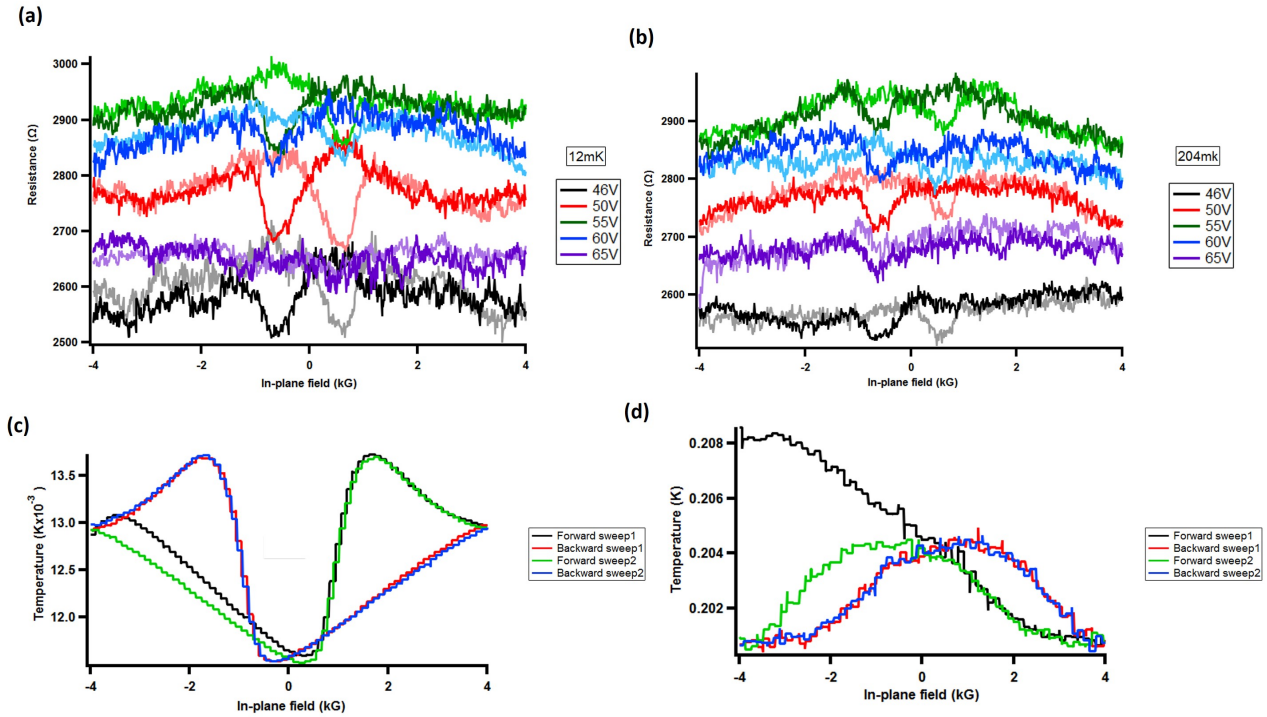


Fig. 6.5.2 Magnetoresistance in the applied in-plane field with different gate voltages. Each curve is the average of two up-sweep curves or two down-sweep curves. (b) Same measurement at 204mK. (c)(d) The temperature variation during up-sweep and down-sweep.

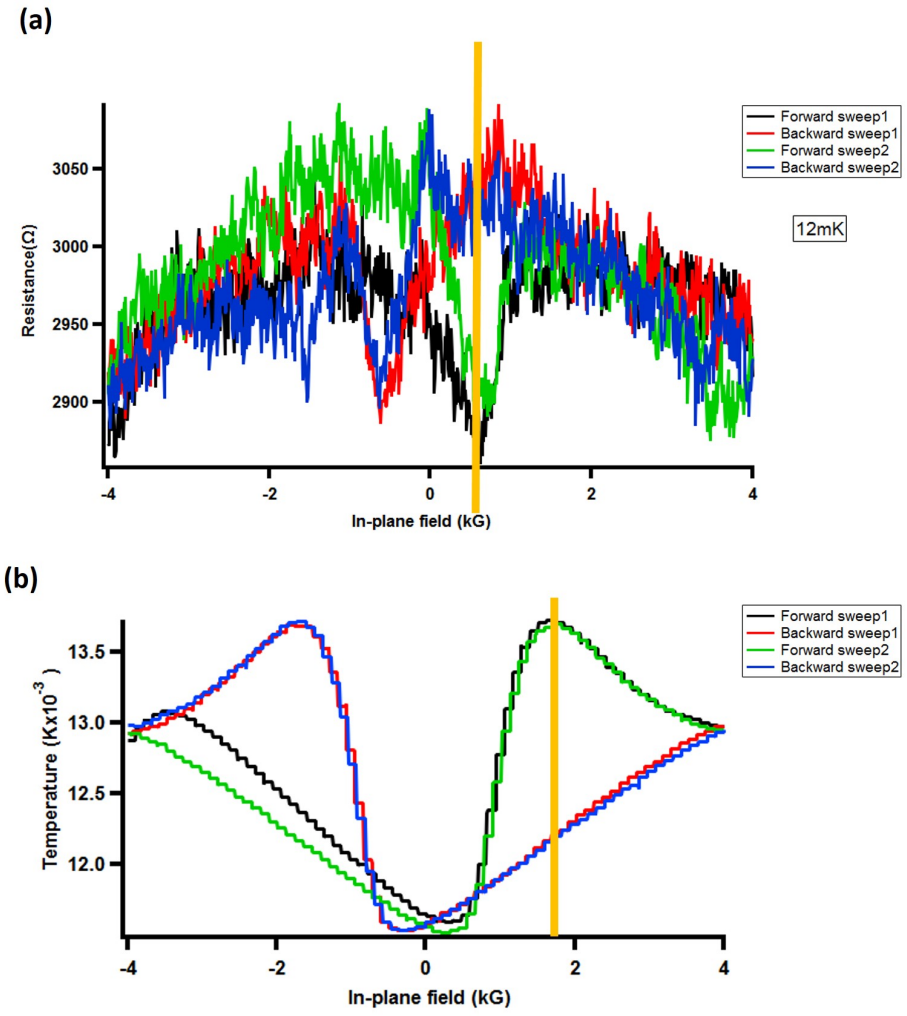


Fig. 6.5.3 (a) The magnetoresistance of $WS_2$/G/$TbPc_2$ by sweeping in-plane magnetic field four times between $\pm$4000Gauss at 12mK. (b) The temperature variation during field sweep at 12mK.

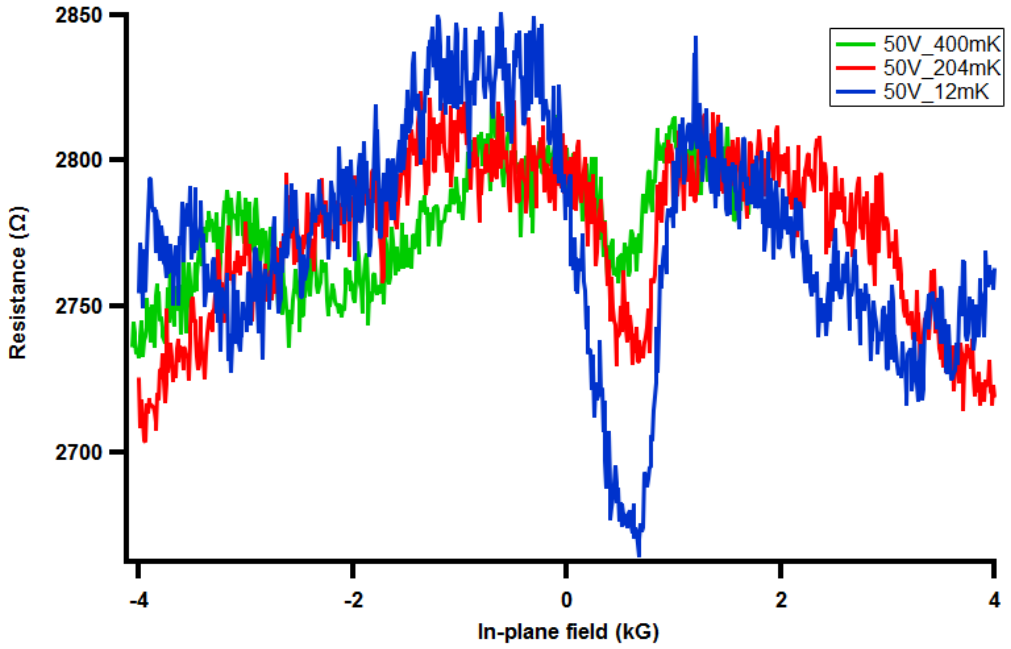


Fig. 6.5.4 $WS_2$/G/$TbPc_2$ sample. Magnetoresistance of the up-sweep curve at fixed gate voltage 50V with different temperatures from 12mK to 400mK.

**Fraunhofer-like patterns in Josephson Junction**

Here, we investigate the effect of $TbPc_2$ molecules grafted on graphene/$WS_2$ Josephson Junction with MoRe superconducting electrodes. The size of the junction is 300nm*4um. The critical current oscillated at the low magnetic field, revealing the conventional Fraunhofer interference pattern. Figure 6.5.5 shows the gate dependence of the measured sample. Unfortunately, due to the back gate leaking problem, we can only stay at the 0V back gate voltage, which is the high hole doping region.

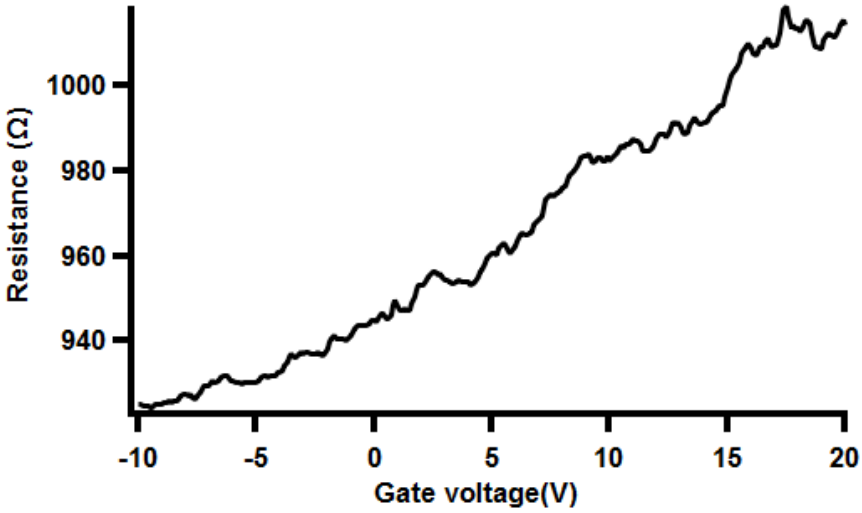


Fig. 6.5.5 Gate dependence of $WS_2$/G/$TbPc_2$ Josephson Junction before back gate leaking occurs.

Figures 6.5.6 (a) and (b) display the differential resistance dV/dI as a function of the small out-of-plane magnetic field in the down-sweep and up-sweep between 10 Gauss. To measure dV/dI, a small AC current (Iac) is added to the DC current (Idc), breaking the superconducting state. The two main features are clearly observed: (i) The shift of the main lobe between down-sweep and up-sweep; (ii) The presence of an asymmetric Fraunhofer-like pattern. The Fraunhofer-like oscillations are clearly observed in (a) and (b), which is a signature of field-induced interference in the supercurrent flowing through the junctions (red color). These hysteretic Fraunhofer patterns have only been found in ferromagnetic Josephson junctions, such as few-layer ferromagnetic insulator $Cr_2Ge_2Te_6$ Josephson junctions [152] and the thin film $Pd_{0.9}Ni_{0.1}$ ferromagnetic Josephson junctions [153], but not in the carbon-based material. Hysteretic Fraunhofer patterns can be another tool to present the induced magnetism on graphene by grafting $TbPc_2$. Compared with Figure 4.2.1, graphene/$TbPc_2$ and $WS_2$/graphene/$TbPc_2$ junctions, the asymmetric Fraunhofer-like pattern is the other interesting phenomenon. In a study of InAs/InGaAs heterostructures based superconductor- semiconductor-superconductor (SNS) junctions [111], they observed the critical current develops a pronounced asymmetry Fraunhofer pattern between positive and negative Bz (150mT) when an in-plane field (400mT) is applied. In the carbon nanotube (CNT) decorated with a $TbPc_2$ system [151], the uniaxial anisotropy and the hysteresis loop in easy axis are indicated in the plane of CNT as well as graphene [28]. Therefore, the asymmetry Fraunhofer pattern can be evidence of the in-plane easy axis on graphene induced by coupled $TbPc_2$ molecules.

Figure 6.5.6 (c), (d) is the Fraunhofer-like pattern in down-sweep and up-sweep between $\pm$5 Gauss. Interestingly, the shift of the main lobe almost disappeared in a smaller sweeping field, but the asymmetry of the interference patterns is still clear. In the end, we increased the sweeping field to $\pm$20 Gauss, and the magnitude of the shift of the main lobe increased with increasing the amplitude of the sweeping field. In Figure 6.5.7, we stay at a fixed Idc current to check the dV/dI of B $\pm$10 Gauss, as seen in Figure 6.5.7 (b) and (d). Indeed the dV/dI of the B field reveal the asymmetric interference pattern and the shift of the main lobe. But, when we applied the magnetic field to the MoRe superconducting electrodes, it was possible to trap flux in the electrodes, which can also be the reason for inducing the shift of the main lobe. Therefore, it is necessary to heat the temperature to eliminate the trapped flux inside MoRe electrodes and reproduce the same measurement to confirm the features. Unfortunately, the sample was dead at the end of the experiment. Whereas we stayed in the very low field during the measurement, still, it is important to do a reproducibility experiment to verify the features in the future. That's why I keep this result in the supplementary measurement section.

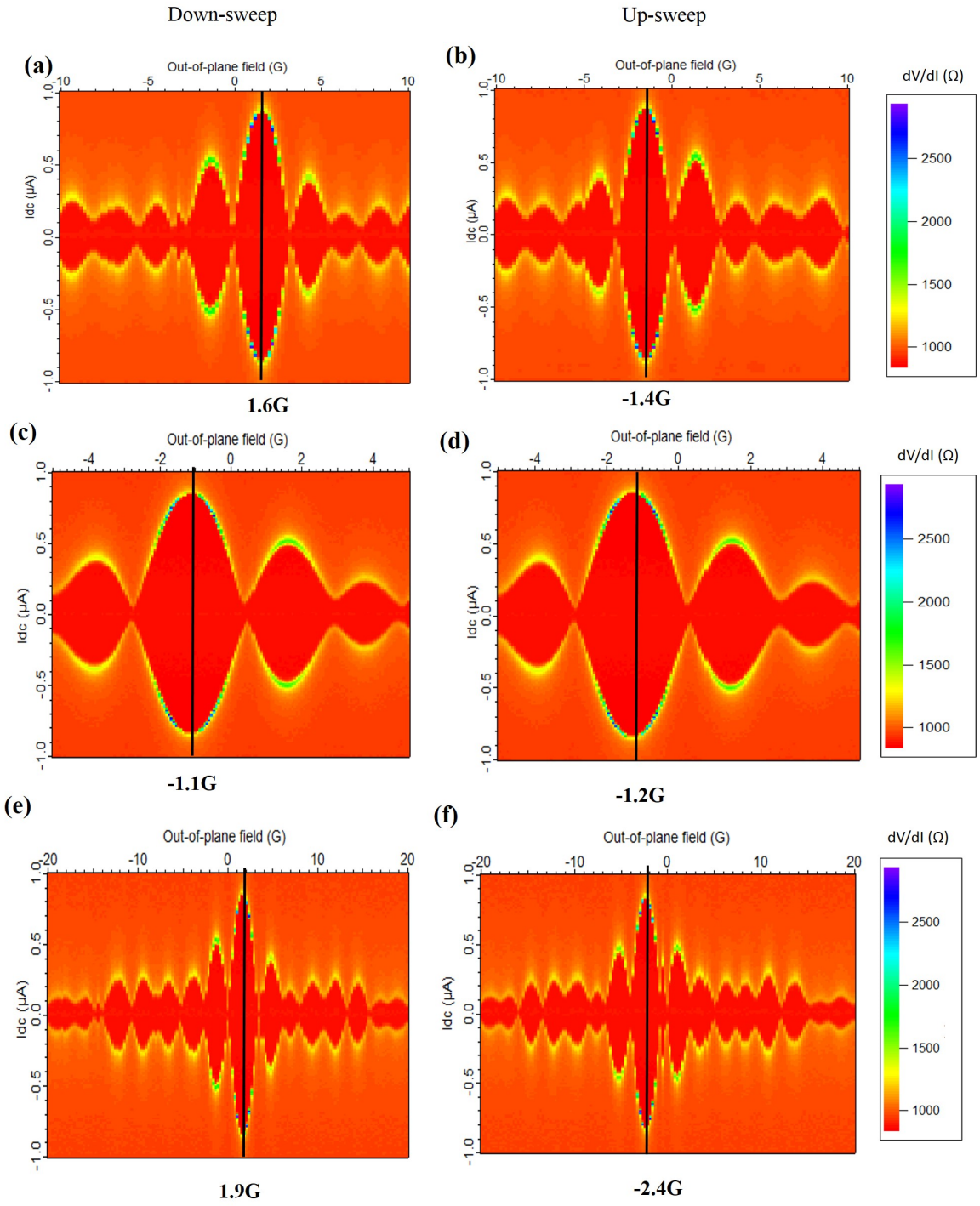


Fig. 6.5.6 (a) dV/dI plotted for both the DC current (Idc) and field (B) in down-sweep (10G to -10G). Fraunhofer-like oscillations are visible. (b) Same measurement but in up-sweep (-10G to 10G). (c) Down-sweep between ±5G. (d) Up-sweep between ±5G.(e) Down-sweep between ±20G. (f) Up-sweep between ±20G. The dark red zone corresponds to the superconducting state.

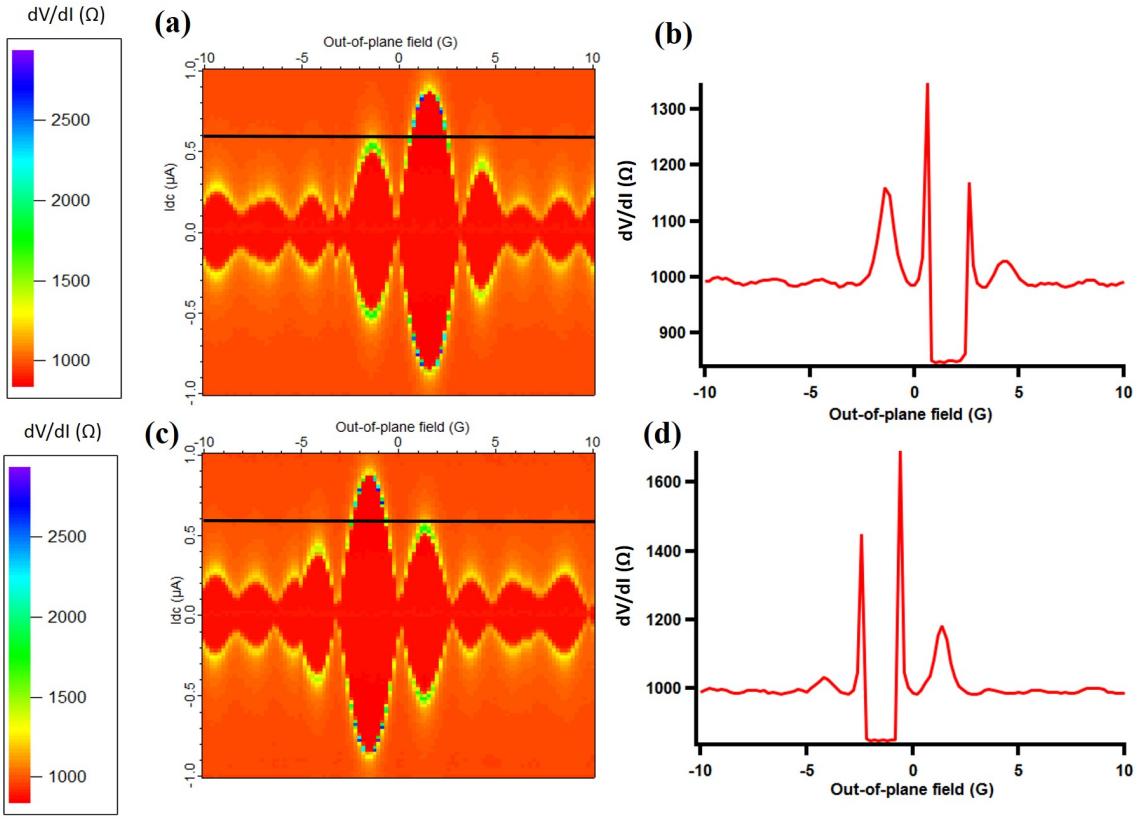


Fig. 6.5.7 The main lobe shift between up-sweep and down-sweep. The asymmetric interference pattern is seen in both measurements. (a) Color plot showing dV/dI as a function of Idc and B. (B) in down-sweep at fixed Idc=0.6uA. (b) dV/dI as a function of B at Idc=0.6uA, the clear asymmetric interference pattern. (c) The same measurement is in the up-sweep field. (d) the clear asymmetric interference pattern also shows in the up-sweep measurement.

## 6.6 Conclusion

The low-temperature magnetoresistance features typical universal conductance fluctuations (UCF) of a phase-coherent sample. Interestingly, these UCFs display a magnetic field-dependent noise highest at low temperatures and low fields. A noise spectrum with a 1/f dependence suggests the existence of magnetic two-level systems with a wide distribution of field-dependent relaxation times. Generally, a 1/f behavior is observed for all experimental spectra at different values of gate voltage, magnetic field, and temperature. However, the noise spectral density deviates from the 1/f behavior when increasing the magnetic field and charge doping. This result proposes that the magnetic barrier energy is reduced by the magnetic field and points to anisotropic Ising-like fluctuating magnetic moments whose characteristic energy barrier decreases with the out-of-plane magnetic field. In the supplementary measurements, we show the gate voltage-dependent hysteresis loops, but they seem to follow the temperature variation during the sweeping in-plane field. In addition, $TbPc_2$ grafted graphene/$WS_2$ Josephson Junction display hysteretic and asymmetric Fraunhofer patterns between up-sweep and down-sweep magnetic fields at very low values of the magnetic field, but further work is needed to confirm these novel findings in molecular layer grafted on graphene Josephson Junction.

# Chapter 7

# Conclusion & Outlook

I have developed the fabrication of heterostructures made from graphene-like 2D materials connected to normal or superconducting electrodes during this work. These samples were designed to investigate spin-dependent quantum transport both in the normal and proximity states in the electrodes are superconducting. In Graphene/$WS_2$ bilayers, we find that spin-orbit interactions induced in graphene by $WS_2$ are at the origin of the formation of edge states carrying the supercurrent, which are very robust in a magnetic field. New possibilities are opened with the recent success in the fabrication of Josephson junctions made of a graphene bilayer encapsulated between two $WS_2$ monolayers realizing the Kane-Mele model of quantum spin Hall in this system [96]. Topological edge states are expected in this system and should be revealed by SQUID interferometry experiments.

We have also investigated how the deposition of different magnetic molecules on graphene or $WS_2$/graphene affects quantum interferences in the normal states, that is, weak localization and mesoscopic conductance fluctuations. Field-dependent 1/f noise was detected, which depended on the spin-flip time compared to the time scale of the experiment. Even if asymmetries in the field could also be observed in the magnetoresistance of certain samples in the few thousand Gauss field region (TCNQ molecules) and attributed to the formation of magnetic domains, hysteresis loops ($TbPc_2$ on graphene/$WS_2$) were shown to have a thermal due to the transition of lead/tin solder. These results illustrate the difficulty of revealing unambiguously molecular magnetism at very low temperatures. However, the more promising result is the observation of hysteresis at a very low magnetic field on Fraunhofer patterns. These last experiments, potentially more sensitive than magnetoresistance measurements, need to be reproduced to eliminate a possible contribution of the superconducting electrodes.

# Appendix A

## Preparation of $TbPc_2$ source

TbPc 2 is synthesized according a slightly modified literature procedure [148]. Briefly, a mixture of 1,2-dicyanobenzene (1 g, 7.80 mmol), $Tb(acac)_3$ , $3H_2O$ (510 mg, 0.97 mmol), and 1,8-diazabicyclo[5.4.0]undec-7-ene (DBU) (290 µL) in 5 mL of dry 1-hexanol was refluxed for 20h. The solution was cooled down to room temperature, then acetic acid (10 mL) was added and mixture was heated at 100°C for one hour. The precipitate was collected by filtration and washed with pentane and $Et_2O$. The crude purple product was redissolved in 100 mL of $CHCl_3$/MeOH (1/1) and undissolved free- base phthalocyanine was filtered off. Both forms, blue (anionic $[TbPc_2]$ ) and green (neutral $[TbPc_2]$ 0), were obtained simultaneously. In order to convert the unstabilized anionic form to the neutral one, the reaction mixture was pre-adsorbed on active basic alumina and then purified by column chromatography on basic alumina (deactivated with 4.6% H2O, level IV) with chloroform/methanolmixture (95:5) as an eluent. 200 mg $TbPc_2$ was obtained (yield 17%).

## Phase coherence of $TbPc_2$ grafted graphene

In the section 5.4, we present a smaller increase of phase coherence length $L_\phi$ on TCNQ grafted graphene sample with temperature decreasing from 4K to 200mK. We refer to the result may suggest the presence of magnetic scattering. For the $TbPc_2$ grafted graphene system, we did a similar measurement as in section 5.4, but with lower molarity ($10^{-7}$M to $10^{-6}$M) of $TbPc_2$ than the measurement in chapter 6. In the meantime, this sample also has a back gate leaking problem. Therefore, we can just apply 30V gate voltage, which is a high doping regime, as seen in the Figure A.0.1. The Figure A.0.2 at applied 30V gate voltage shows the weak localization at a lower temperature (10mK, 250mK, 580mK, and 800mK)

are suppressed. The phase coherence length $L_\phi$ just slightly increased when we are cooling down the temperature from 3.7K to T $\leq$ 800mK. The result is similar to section 5.4, which suggests the presence of magnetic scattering.

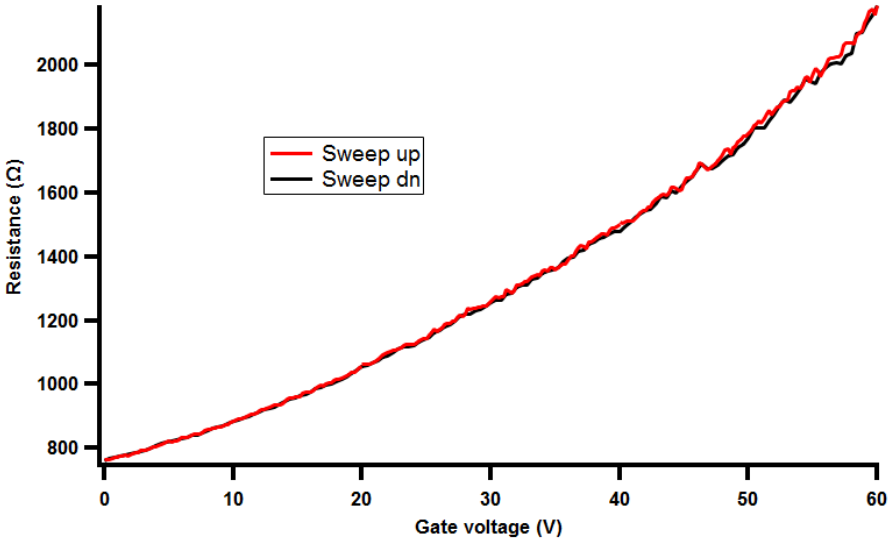


Fig. A.0.1 Gate dependence of $TbPc_2$ grafted graphene sample, the applied gate voltage is 30V, which is in the high doping regime.

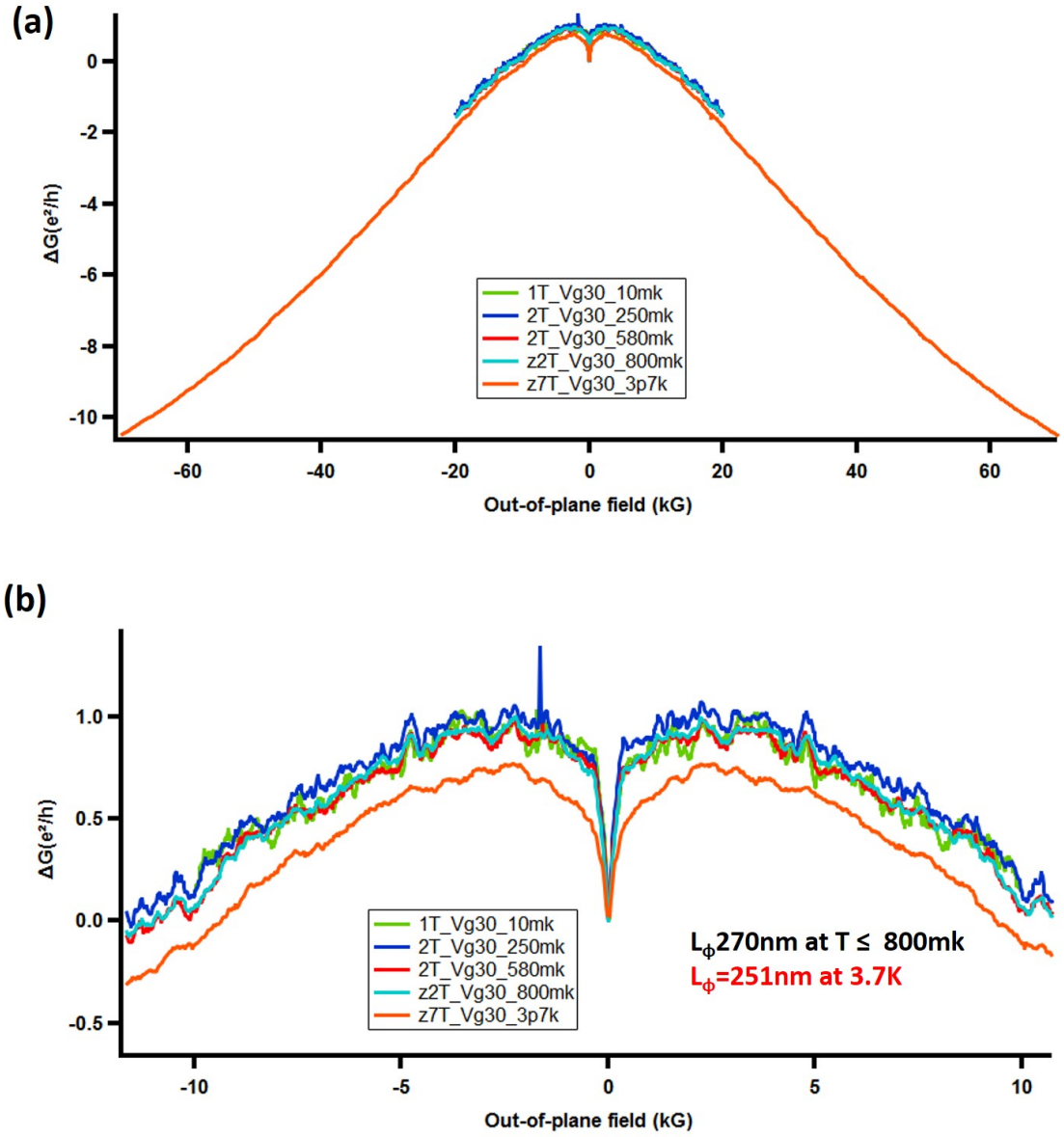


Fig. A.0.2 Magneto-conductance in out-of-plane field at 10mK, 250Mk, 580mK, 800mK and 3.7K with applied gate voltage 30V (a) Temperature dependence of magneto-conductance. In order to see the conductance fluctuation when temperature increases, the range of sweeping field is also increasing from 1T at 10mk, 2T at 250mk to 800mk, until 7T at 3.7K. (b) Zoom in the field range between $\pm$ 2T. The weak localization is clearly suppressed due to the induced magnetic moment on graphene by $TbPc_2$ molecules. The phase coherence length $L_\phi$ is slightly decreased with temperature increasing from 10mK temperature to 3.7K.

# References


[1] Kostya S Novoselov, Andre K Geim, Sergei Vladimirovich Morozov, Dingde Jiang, Michail I Katsnelson, IVa Grigorieva, SVb Dubonos, and andAA Firsov. Two-dimensional gas of massless dirac fermions in graphene. *nature*, 438(7065):197–200, 2005.

[2] Kostya S Novoselov, Edward McCann, SV Morozov, Vladimir I Fal'ko, MI Katsnelson, U Zeitler, D Jiang, F Schedin, and AK Geim. Unconventional quantum hall effect and berry's phase of $2\pi$ in bilayer graphene. *Nature physics*, 2(3):177–180, 2006.

[3] Konstantin S Novoselov, Z Jiang, Y Zhang, SV Morozov, Horst L Stormer, U Zeitler, JC Maan, GS Boebinger, Philip Kim, and Andre K Geim. Room-temperature quantum hall effect in graphene. *science*, 315(5817):1379–1379, 2007.

[4] Richard Van Noorden. The trials of new carbon. *Nature*, 469(7328):14, 2011.

[5] Vimlesh Chandra, Jaesung Park, Young Chun, Jung Woo Lee, In-Chul Hwang, and Kwang S Kim. Water-dispersible magnetite-reduced graphene oxide composites for arsenic removal. *ACS nano*, 4(7):3979–3986, 2010.

[6] Sung Huh, Jaesung Park, Kwang S Kim, Byung Hee Hong, and Seung Bin Kim. Selective n-type doping of graphene by photo-patterned gold nanoparticles. *ACS nano*, 5(5):3639–3644, 2011.

[7] Wi Hyoung Lee, Jaesung Park, Youngsoo Kim, Kwang S Kim, Byung Hee Hong, and Kilwon Cho. Control of graphene field-effect transistors by interfacial hydrophobic self-assembled monolayers. *Advanced Materials*, 23(30):3460–3464, 2011.

[8] Manuela Garnica, Daniele Stradi, Sara Barja, Fabian Calleja, Cristina Díaz, Manuel Alcamí, Nazario Martín, Amadeo L Vazquez de Parga, Fernando Martín, and Rodolfo Miranda. Long-range magnetic order in a purely organic 2d layer adsorbed on epitaxial graphene. *Nature Physics*, 9(6):368–374, 2013.

[9] Johann Coraux, Alpha T N'Diaye, Nicolas Rougemaille, Chi Vo-Van, Amina Kimouche, Hong-Xin Yang, Mairbek Chshiev, Nedjma Bendiab, Olivier Fruchart, and Andreas K Schmid. Air-protected epitaxial graphene/ferromagnet hybrids prepared by chemical vapor deposition and intercalation. *The Journal of Physical Chemistry Letters*, 3(15):2059–2063, 2012.

[10] Zhe Wang, Dong-Keun Ki, Hua Chen, Helmuth Berger, Allan H MacDonald, and Alberto F Morpurgo. Strong interface-induced spin–orbit interaction in graphene on ws2. *Nature communications*, 6(1):1–7, 2015.

[11] Taro Wakamura, Francesco Reale, Pawel Palczynski, Sophie Guéron, Cecilia Mattevi, and Hélène Bouchiat. Strong anisotropic spin-orbit interaction induced in graphene by monolayer ws 2. *Physical review letters*, 120(10):106802, 2018.

[12] Riccardo Frisenda, Efrén Navarro-Moratalla, Patricia Gant, David Pérez De Lara, Pablo Jarillo-Herrero, Roman V Gorbachev, and Andres Castellanos-Gomez. Recent progress in the assembly of nanodevices and van der waals heterostructures by deterministic placement of 2d materials. *Chemical Society Reviews*, 47(1):53–68, 2018.

[13] Lei Wang, I Meric, PY Huang, Q Gao, Y Gao, H Tran, T Taniguchi, Kenji Watanabe, LM Campos, DA Muller, et al. One-dimensional electrical contact to a two-dimensional material. *Science*, 342(6158):614–617, 2013.

[14] DG Purdie, NM Pugno, T Taniguchi, K Watanabe, AC Ferrari, and Antonio Lombardo. Cleaning interfaces in layered materials heterostructures. *Nature communications*, 9(1):1–12, 2018.

[15] Tsuneya Ando, Takeshi Nakanishi, and Riichiro Saito. Berry's phase and absence of back scattering in carbon nanotubes. *Journal of the Physical Society of Japan*, 67(8):2857–2862, 1998.

[16] Simon Zihlmann, Aron W Cummings, Jose H Garcia, Máté Kedves, Kenji Watanabe, Takashi Taniguchi, Christian Schönenberger, and Péter Makk. Large spin relaxation anisotropy and valley-zeeman spin-orbit coupling in wse 2/graphene/h-bn heterostructures. *Physical review B*, 97(7):075434, 2018.

[17] T Wakamura, F Reale, P Palczynski, MQ Zhao, ATC Johnson, S Guéron, C Mattevi, A Ouerghi, and H Bouchiat. Spin-orbit interaction induced in graphene by transition metal dichalcogenides. *Physical Review B*, 99(24):245402, 2019.

[18] Xiaojie Liu, Tianjiao Wang, Li Niu, Yin Wang, Qiang Zhang, and Haitao Yin. Magnetic proximity, magnetoresistance and spin filtering effect in a binuclear ferric phthalocyanine from first principles. *Journal of Physics D: Applied Physics*, 53(3):035305, 2019.

[19] Bo Zhang, Bairui Tao, Xiaojie Liu, Weiqi Li, and Haitao Yin. Perfect dual spin filtering effect and large magnetoresistance in all-carbon devices based on c18 cyclo molecule from first principles. *Physics Letters A*, 441:128166, 2022.

[20] Greg Szulczewski, Stefano Sanvito, and Michael Coey. A spin of their own. *Nature materials*, 8(9):693–695, 2009.

[21] Stefano Sanvito. Molecular spintronics. *Chemical Society Reviews*, 40(6):3336–3355, 2011.

[22] Sang Uck Lee, Rodion V Belosludov, Hiroshi Mizuseki, and Yoshiyuki Kawazoe. The role of aromaticity and the $\pi$-conjugated framework in multiporphyrinic systems as single-molecule switches. *Small*, 4(7):962–969, 2008.

[23] Jing Huang, Weiyi Wang, Shangfeng Yang, Haibin Su, Qunxiang Li, and Jinlong Yang. A theoretical study of spin-polarized transport properties of planar four-coordinate fe complexes. *Chemical Physics Letters*, 539:102–106, 2012.

[24] Jing Huang, Weiyi Wang, Shangfeng Yang, Qunxiang Li, and Jinlong Yang. Efficient spin filter based on fen4 complexes between carbon nanotube electrodes. *Nanotechnology*, 23(25):255202, 2012.

[25] Kenji Toyoda. Theoretical investigation of chemical spin doping into single porphyrin junctions toward ultrahigh-sensitive nitric oxide sensor. *Japanese Journal of Applied Physics*, 51(4R):045202, 2012.

[26] Davide Maccariello, Manuela Garnica, Miguel A Nino, Cristina Navio, Paolo Perna, Sara Barja, Amadeo L Vazquez de Parga, and Rodolfo Miranda. Spatially resolved, site-dependent charge transfer and induced magnetic moment in tcnq adsorbed on graphene. *Chemistry of Materials*, 26(9):2883–2890, 2014.

[27] Chuan Li, Katsuyoshi Komatsu, S Bertrand, G Clavé, S Campidelli, A Filoramo, S Guéron, and H Bouchiat. Signature of gate-tunable magnetism in graphene grafted with pt-porphyrins. *Physical Review B*, 93(4):045403, 2016.

[28] Andrea Candini, Svetlana Klyatskaya, Mario Ruben, Wolfgang Wernsdorfer, and Marco Affronte. Graphene spintronic devices with molecular nanomagnets. *Nano letters*, 11(7):2634–2639, 2011.

[29] Matias Urdampilleta, Svetlana Klyatskaya, Jean-Pierre Cleuziou, Mario Ruben, and Wolfgang Wernsdorfer. Supramolecular spin valves. *Nature materials*, 10(7):502–506, 2011.

[30] Stefan Thiele, Franck Balestro, Rafik Ballou, Svetlana Klyatskaya, Mario Ruben, and Wolfgang Wernsdorfer. Electrically driven nuclear spin resonance in single-molecule magnets. *Science*, 344(6188):1135–1138, 2014.

[31] C Godfrin, Stefano Lumetti, H Biard, E Bonet, S Klyatskaya, Mario Ruben, A Candini, M Affronte, W Wernsdorfer, and F Balestro. Microwave-assisted reversal of a single electron spin. *Journal of Applied Physics*, 125(14):142801, 2019.

[32] Romain Vincent, Svetlana Klyatskaya, Mario Ruben, Wolfgang Wernsdorfer, and Franck Balestro. Electronic read-out of a single nuclear spin using a molecular spin transistor. *Nature*, 488(7411):357–360, 2012.

[33] Gita Sedghi, Víctor M García-Suárez, Louisa J Esdaile, Harry L Anderson, Colin J Lambert, Santiago Martín, Donald Bethell, Simon J Higgins, Martin Elliott, Neil Bennett, et al. Long-range electron tunnelling in oligo-porphyrin molecular wires. *Nature nanotechnology*, 6(8):517–523, 2011.

[34] P Checcoli, G Conte, S Salvatori, R Paolesse, A Bolognesi, M Berliocchi, F Brunetti, A D'Amico, A Di Carlo, and P t Lugli. Tetra-phenyl porphyrin based thin film transistors. *Synthetic metals*, 138(1-2):261–266, 2003.

[35] Pulak Dutta and PM Horn. Low-frequency fluctuations in solids: 1 f noise. *Reviews of Modern physics*, 53(3):497, 1981.

[36] Philip Richard Wallace. The band theory of graphite. *Physical review*, 71(9):622, 1947.

[37] Andre K Geim and Konstantin S Novoselov. The rise of graphene. In *Nanoscience and technology: a collection of reviews from nature journals*, pages 11–19. World Scientific, 2010.

[38] AH Castro Neto, Francisco Guinea, Nuno MR Peres, Kostya S Novoselov, and Andre K Geim. The electronic properties of graphene. *Reviews of modern physics*, 81(1):109, 2009.

[39] C Riedl, C Coletti, and U Starke. Structural and electronic properties of epitaxial graphene on sic (0 0 0 1): a review of growth, characterization, transfer doping and hydrogen intercalation. *Journal of Physics D: Applied Physics*, 43(37):374009, 2010.

[40] MI Katsnelson, KS Novoselov, and AK Geim. Chiral tunnelling and the klein paradox in graphene. *Nature physics*, 2(9):620–625, 2006.

[41] Yuanbo Zhang, Yan-Wen Tan, Horst L Stormer, and Philip Kim. Experimental observation of the quantum hall effect and berry's phase in graphene. *nature*, 438(7065):201–204, 2005.

[42] F Duncan M Haldane. Model for a quantum hall effect without landau levels: Condensed-matter realization of the" parity anomaly". *Physical review letters*, 61(18):2015, 1988.

[43] Martin Gmitra, Sergej Konschuh, Christian Ertler, C Ambrosch-Draxl, and Jaroslav Fabian. Band-structure topologies of graphene: Spin-orbit coupling effects from first principles. *Physical Review B*, 80(23):235431, 2009.

[44] Igor Žutić, Jaroslav Fabian, and S Das Sarma. Spintronics: Fundamentals and applications. *Reviews of modern physics*, 76(2):323, 2004.

[45] MZ Hasa and CL Kane. Topological insulators. *Rev. Mod. Phys*, 82:3045, 2010.

[46] Zhiyong Wang, Chi Tang, Raymond Sachs, Yafis Barlas, and Jing Shi. Proximity-induced ferromagnetism in graphene revealed by the anomalous hall effect. *Physical review letters*, 114(1):016603, 2015.

[47] Di Xiao, Gui-Bin Liu, Wanxiang Feng, Xiaodong Xu, and Wang Yao. Coupled spin and valley physics in monolayers of mos 2 and other group-vi dichalcogenides. *Physical review letters*, 108(19):196802, 2012.

[48] Alberto Morpurgo. "designer"spin-orbit interaction in graphene on semiconducting transition metal dichalcogenides. In *APS March Meeting Abstracts*, volume 2017, pages F31–001, 2017.

[49] Bowen Yang, Min-Feng Tu, Jeongwoo Kim, Yong Wu, Hui Wang, Jason Alicea, Ruqian Wu, Marc Bockrath, and Jing Shi. Tunable spin–orbit coupling and symmetry-protected edge states in graphene/ws2. *2D Materials*, 3(3):031012, 2016.

[50] Charles Kittel, Paul McEuen, and Paul McEuen. *Introduction to solid state physics*, volume 8. Wiley New York, 1996.

[51] M Tinkham. Introduction to superconductivity, volume second edition, 2004.

[52] H Van Houten and CWJ Beenakker. Andreev reflection and the josephson effect in a quantum point contact: An analogy with phase-conjugating resonators. *Physica B: Condensed Matter*, 175(1-3):187–197, 1991.

[53] JD Pillet, CHL Quay, P Morfin, C Bena, A Levy Yeyati, and P Joyez. Andreev bound states in supercurrent-carrying carbon nanotubes revealed. *Nature Physics*, 6(12):965–969, 2010.

[54] Akira Furusaki, Hideaki Takayanagi, and Masaru Tsukada. Theory of quantum conduction of supercurrent through a constriction. *Physical review letters*, 67(1):132, 1991.

[55] CWJ Beenakker. Colloquium: Andreev reflection and klein tunneling in graphene. *Reviews of Modern Physics*, 80(4):1337, 2008.

[56] M Titov and Carlo WJ Beenakker. Josephson effect in ballistic graphene. *Physical Review B*, 74(4):041401, 2006.

[57] S Washburn and RA Webb. Quantum transport in small disordered samples from the diffusive to the ballistic regime. *Reports on Progress in Physics*, 55(8):1311, 1992.

[58] PM Echternach, ME Gershenson, HM Bozler, AL Bogdanov, and B Nilsson. Nyquist phase relaxation in one-dimensional metal films. *Physical Review B*, 48(15):11516, 1993.

[59] Pritiraj Mohanty, EMQ Jariwala, and Richard A Webb. Intrinsic decoherence in mesoscopic systems. *Physical Review Letters*, 78(17):3366, 1997.

[60] Supriyo Datta. *Electronic transport in mesoscopic systems*. Cambridge university press, 1997.

[61] CWJ Beenakker and Henk van Houten. Quantum transport in semiconductor nanostructures. In *Solid state physics*, volume 44, pages 1–228. Elsevier, 1991.

[62] Shinobu Hikami, Anatoly I Larkin, and Yosuke Nagaoka. Spin-orbit interaction and magnetoresistance in the two dimensional random system. *Progress of Theoretical Physics*, 63(2):707–710, 1980.

[63] Hidekatsu Suzuura and Tsuneya Ando. Crossover from symplectic to orthogonal class in a two-dimensional honeycomb lattice. *Physical review letters*, 89(26):266603, 2002.

[64] Edward McCann and Vladimir I Fal'ko. z→- z symmetry of spin-orbit coupling and weak localization in graphene. *Physical review letters*, 108(16):166606, 2012.

[65] FV Tikhonenko, AA Kozikov, AK Savchenko, and RV Gorbachev. Transition between electron localization and antilocalization in graphene. *Physical Review Letters*, 103(22):226801, 2009.

[66] Y Yafet. g factors and spin-lattice relaxation of conduction electrons. In *Solid state physics*, volume 14, pages 1–98. Elsevier, 1963.

[67] MI Dyakonov and VI Perel. Spin relaxation of conduction electrons in noncentrosymmetric semiconductors. *Soviet Physics Solid State, Ussr*, 13(12):3023–3026, 1972.

[68] Patrick A Lee and A Douglas Stone. Universal conductance fluctuations in metals. *Physical review letters*, 55(15):1622, 1985.

[69] Yoseph Imry. Active transmission channels and universal conductance fluctuations. *EPL (Europhysics Letters)*, 1(5):249, 1986.

[70] PA Lee, A Douglas Stone, and Hidetoshi Fukuyama. Universal conductance fluctuations in metals: Effects of finite temperature, interactions, and magnetic field. *Physical Review B*, 35(3):1039, 1987.

[71] DJ Thouless. Maximum metallic resistance in thin wires. *Physical Review Letters*, 39(18):1167, 1977.

[72] A Rycerz, J Tworzydło, and CWJ Beenakker. Anomalously large conductance fluctuations in weakly disordered graphene. *EPL (Europhysics Letters)*, 79(5):57003, 2007.

[73] J Tworzydło, CW Groth, and CWJ Beenakker. Finite difference method for transport properties of massless dirac fermions. *Physical Review B*, 78(23):235438, 2008.

[74] Kazi Rafsanjani Amin, Samriddhi Sankar Ray, Nairita Pal, Rahul Pandit, and Aveek Bid. Exotic multifractal conductance fluctuations in graphene. *Communications Physics*, 1(1):1–7, 2018.

[75] MB Weissman. Low-frequency noise as a tool to study disordered materials. *Annual Review of Materials Science*, 26(1):395–429, 1996.

[76] J Bernamont. Fluctuations de potentiel aux bornes d'un conducteur metallique de faible volume parcouru par un courant. In *Annales de Physique*, volume 11, pages 71–140. EDP Sciences, 1937.

[77] FN Hooge. 1/f noise. *Physica B+ c*, 83(1):14–23, 1976.

[78] Sh Kogan. Electronic noise and fluctuations in solids cambridge univ, 1996.

[79] Min Yi and Zhigang Shen. A review on mechanical exfoliation for the scalable production of graphene. *Journal of Materials Chemistry A*, 3(22):11700–11715, 2015.

[80] Yuan Huang, Eli Sutter, Norman N Shi, Jiabao Zheng, Tianzhong Yang, Dirk Englund, Hong-Jun Gao, and Peter Sutter. Reliable exfoliation of large-area high-quality flakes of graphene and other two-dimensional materials. *ACS nano*, 9(11):10612–10620, 2015.

[81] Yuan Huang, Yu-Hao Pan, Rong Yang, Li-Hong Bao, Lei Meng, Hai-Lan Luo, Yong-Qing Cai, Guo-Dong Liu, Wen-Juan Zhao, Zhang Zhou, et al. Universal mechanical exfoliation of large-area 2d crystals. *Nature communications*, 11(1):1–9, 2020.

[82] Sujay B Desai, Surabhi R Madhvapathy, Matin Amani, Daisuke Kiriya, Mark Hettick, Mahmut Tosun, Yuzhi Zhou, Madan Dubey, Joel W Ager III, Daryl Chrzan, et al. Gold-mediated exfoliation of ultralarge optoelectronically-perfect monolayers. *Advanced Materials*, 28(21):4053–4058, 2016.

[83] Andres Castellanos-Gomez, Michele Buscema, Rianda Molenaar, Vibhor Singh, Laurens Janssen, Herre SJ Van Der Zant, and Gary A Steele. Deterministic transfer of two-dimensional materials by all-dry viscoelastic stamping. *2D Materials*, 1(1):011002, 2014.

[84] Xu Cui, Gwan-Hyoung Lee, Young Duck Kim, Ghidewon Arefe, Pinshane Y Huang, Chul-Ho Lee, Daniel A Chenet, Xian Zhang, Lei Wang, Fan Ye, et al. Multi-terminal transport measurements of mos2 using a van der waals heterostructure device platform. *Nature nanotechnology*, 10(6):534–540, 2015.

[85] AV Kretinin, Y Cao, JS Tu, GL Yu, R Jalil, KS Novoselov, SJ Haigh, A Gholinia, A Mishchenko, M Lozada, et al. Electronic properties of graphene encapsulated with different two-dimensional atomic crystals. *Nano letters*, 14(6):3270–3276, 2014.

[86] Filippo Pizzocchero, Lene Gammelgaard, Bjarke S Jessen, José M Caridad, Lei Wang, James Hone, Peter Bøggild, and Timothy J Booth. The hot pick-up technique for batch assembly of van der waals heterostructures. *Nature communications*, 7(1):1–10, 2016.

[87] Cun Feng Fan, Tahir Cagin, Wen Shi, and Kennith A Smith. Local chain dynamics of a model polycarbonate near glass transition temperature: A molecular dynamics simulation. *Macromolecular theory and simulations*, 6(1):83–102, 1997.

[88] Suhan Son, Young Jae Shin, Kaixuan Zhang, Jeacheol Shin, Sungmin Lee, Hiroshi Idzuchi, Matthew J Coak, Hwangsun Kim, Jangwon Kim, Jae Hoon Kim, et al. Strongly adhesive dry transfer technique for van der waals heterostructure. *2D Materials*, 7(4):041005, 2020.

[89] Marian A Herman and Helmut Sitter. *Molecular beam epitaxy: fundamentals and current status*, volume 7. Springer Science & Business Media, 2012.

[90] Robin FC Farrow. *Molecular beam epitaxy: applications to key materials*. Elsevier, 1995.

[91] Nikhil P. Concept drawing of a molecular beam epitaxy growth chamber., July 2015.

[92] Zhichun Yang, Shasha Zhang, Lingbo Li, and Wei Chen. Research progress on large-area perovskite thin films and solar modules. *Journal of Materiomics*, 3(4):231–244, 2017.

[93] Fuhui Shao, Steffi Y Woo, Nianjheng Wu, Robert Schneider, Andrew J Mayne, Steffen Michaelis de Vasconcellos, Ashish Arora, Benjamin J Carey, Johann A Preuß, Noémie Bonnet, et al. Substrate influence on transition metal dichalcogenide monolayer exciton absorption linewidth broadening. *Physical Review Materials*, 6(7):074005, 2022.

[94] J Vallejo Bustamante, NJ Wu, C Fermon, M Pannetier-Lecoeur, T Wakamura, K Watanabe, T Taniguchi, T Pellegrin, A Bernard, S Daddinounou, et al. Detection of graphene's divergent orbital diamagnetism at the dirac point. *Science*, 374(6573):1399–1402, 2021.

[95] Ziwei Dou, Taro Wakamura, Pauli Virtanen, Nian-Jheng Wu, Richard Deblock, Sandrine Autier-Laurent, Kenji Watanabe, Takashi Taniguchi, Sophie Guéron, Hélène Bouchiat, et al. Phase-dependent dissipation and supercurrent of a graphene-superconductor ring under microwave irradiation. *arXiv preprint arXiv:2011.07308*, 2020.

[96] JO Island, X Cui, C Lewandowski, JY Khoo, EM Spanton, H Zhou, D Rhodes, JC Hone, T Taniguchi, K Watanabe, et al. Spin–orbit-driven band inversion in bilayer graphene by the van der waals proximity effect. *Nature*, 571(7763):85–89, 2019.

[97] Alexandre Avraamovitch Golubov, M Yu Kupriyanov, and E Il'Ichev. The current-phase relation in josephson junctions. *Reviews of modern physics*, 76(2):411, 2004.

[98] T Wakamura, NJ Wu, AD Chepelianskii, S Guéron, M Och, M Ferrier, T Taniguchi, K Watanabe, C Mattevi, and H Bouchiat. Spin-orbit-enhanced robustness of supercurrent in graphene/ws 2 josephson junctions. *Physical Review Letters*, 125(26):266801, 2020.

[99] JC Cuevas and FS Bergeret. Magnetic interference patterns and vortices in diffusive sns junctions. *Physical review letters*, 99(21):217002, 2007.

[100] Benoît Crouzy and Dmitri A Ivanov. Magnetic interference patterns in long disordered josephson junctions. *Physical Review B*, 87(2):024514, 2013.

[101] JM Lu, O Zheliuk, Inge Leermakers, Noah FQ Yuan, Uli Zeitler, Kam Tuen Law, and JT3445699 Ye. Evidence for two-dimensional ising superconductivity in gated mos2. *Science*, 350(6266):1353–1357, 2015.

[102] Xiaoxiang Xi, Zefang Wang, Weiwei Zhao, Ju-Hyun Park, Kam Tuen Law, Helmuth Berger, László Forró, Jie Shan, and Kin Fai Mak. Ising pairing in superconducting nbse2 atomic layers. *Nature Physics*, 12(2):139–143, 2016.

[103] Kun Zuo, Vincent Mourik, Daniel B Szombati, Bas Nijholt, David J Van Woerkom, Attila Geresdi, Jun Chen, Viacheslav P Ostroukh, Anton R Akhmerov, Sebastién R Plissard, et al. Supercurrent interference in few-mode nanowire josephson junctions. *Physical review letters*, 119(18):187704, 2017.

[104] Bas Nijholt and Anton R Akhmerov. Orbital effect of magnetic field on the majorana phase diagram. *Physical Review B*, 93(23):235434, 2016.

[105] M Ben Shalom, MJ Zhu, VI Fal'Ko, A Mishchenko, AV Kretinin, KS Novoselov, CR Woods, K Watanabe, T Taniguchi, AK Geim, et al. Quantum oscillations of the critical current and high-field superconducting proximity in ballistic graphene. *Nature Physics*, 12(4):318–322, 2016.

[106] Victor E Calado, Srijit Goswami, Gaurav Nanda, Mathias Diez, Anton R Akhmerov, Kenji Watanabe, Takashi Taniguchi, Teun M Klapwijk, and Lieven MK Vandersypen. Ballistic josephson junctions in edge-contacted graphene. *Nature nanotechnology*, 10(9):761–764, 2015.

[107] IV Borzenets, F Amet, CT Ke, AW Draelos, MT Wei, A Seredinski, K Watanabe, T Taniguchi, Y Bomze, M Yamamoto, et al. Ballistic graphene josephson junctions from the short to the long junction regimes. *Physical review letters*, 117(23):237002, 2016.

[108] Francois Amet, Chung Ting Ke, Ivan V Borzenets, J Wang, Keji Watanabe, Takashi Taniguchi, Russell S Deacon, Michihisa Yamamoto, Yuriy Bomze, Seigo Tarucha, et al. Supercurrent in the quantum hall regime. *Science*, 352(6288):966–969, 2016.

[109] Francesco Reale, Pawel Palczynski, Iddo Amit, Gareth F Jones, Jake D Mehew, Agnes Bacon, Na Ni, Peter C Sherrell, Stefano Agnoli, Monica F Craciun, et al. High-mobility and high-optical quality atomically thin ws 2. *Scientific reports*, 7(1):1–10, 2017.

[110] Anil Murani, Alexei Chepelianskii, Sophie Guéron, and Hélène Bouchiat. Andreev spectrum with high spin-orbit interactions: revealing spin splitting and topologically protected crossings. *Physical Review B*, 96(16):165415, 2017.

[111] HJ Suominen, J Danon, M Kjaergaard, K Flensberg, J Shabani, CJ Palmstrøm, F Nichele, and CM Marcus. Anomalous fraunhofer interference in epitaxial superconductor-semiconductor josephson junctions. *Physical Review B*, 95(3):035307, 2017.

[112] Jyongsil Gu, Wongoon Cha, Kenji Gamo, and Susumu Namba. Properties of niobium superconducting bridges prepared by electron-beam lithography and ion implantation. *Journal of Applied Physics*, 50(10):6437–6442, 1979.

[113] BL Altshuler and BZ Spivak. Mesoscopic fluctations in a superconductor–normal metal–superconductor junction. *Zh. Eksp. Teor. Fiz.*, 92(2):607–615, 1987.

[114] CWJ Beenakker. Universal limit of critical-current fluctuations in mesoscopic josephson junctions. *Physical review letters*, 67(27):3836, 1991.

[115] Manuel Houzet and Mikhail A Skvortsov. Mesoscopic fluctuations of the supercurrent in diffusive josephson junctions. *Physical Review B*, 77(2):024525, 2008.

[116] Hideaki Takayanagi, Jørn Bindslev Hansen, and Junsaku Nitta. Mesoscopic fluctuations of the critical current in a superconductor—normal-conductor—superconductor. *Physical review letters*, 74(1):166, 1995.

[117] Yong-Joo Doh, Jorden A van Dam, Aarnoud L Roest, Erik PAM Bakkers, Leo P Kouwenhoven, and Silvano De Franceschi. Tunable supercurrent through semiconductor nanowires. *science*, 309(5732):272–275, 2005.

[118] Hendrik Meier, Vladimir I Fal'ko, and Leonid I Glazman. Edge effects in the magnetic interference pattern of a ballistic sns junction. *Physical Review B*, 93(18):184506, 2016.

[119] Aron W Cummings, Jose H Garcia, Jaroslav Fabian, and Stephan Roche. Giant spin lifetime anisotropy in graphene induced by proximity effects. *Physical review letters*, 119(20):206601, 2017.

[120] Alessandro David, Péter Rakyta, Andor Kormányos, and Guido Burkard. Induced spin-orbit coupling in twisted graphene–transition metal dichalcogenide heterobilayers: Twistronics meets spintronics. *Physical Review B*, 100(8):085412, 2019.

[121] Tobias Frank, Petra Högl, Martin Gmitra, Denis Kochan, and Jaroslav Fabian. Protected pseudohelical edge states in z 2-trivial proximitized graphene. *Physical Review Letters*, 120(15):156402, 2018.

[122] AG Mal'shukov, Severin Sadjina, and Arne Brataas. Inverse spin hall effect in superconductor/normal-metal/superconductor josephson junctions. *Physical Review B*, 81(6):060502, 2010.

[123] FS Bergeret and IV Tokatly. Spin-orbit coupling as a source of long-range triplet proximity effect in superconductor-ferromagnet hybrid structures. *Physical Review B*, 89(13):134517, 2014.

[124] François Konschelle, Ilya V Tokatly, and F Sebastián Bergeret. Theory of the spin-galvanic effect and the anomalous phase shift $\varphi$ 0 in superconductors and josephson junctions with intrinsic spin-orbit coupling. *Physical Review B*, 92(12):125443, 2015.

[125] F Sebastián Bergeret and Ilya V Tokatly. Theory of the magnetic response in finite two-dimensional superconductors. *Physical Review B*, 102(6):060506, 2020.

[126] VP Ostroukh, B Baxevanis, AR Akhmerov, and CWJ Beenakker. Two-dimensional josephson vortex lattice and anomalously slow decay of the fraunhofer oscillations in a ballistic sns junction with a warped fermi surface. *Physical Review B*, 94(9):094514, 2016.

[127] Hugo Henck, Zeineb Ben Aziza, Debora Pierucci, Feriel Laourine, Francesco Reale, Pawel Palczynski, Julien Chaste, Mathieu G Silly, François Bertran, Patrick Le Fevre, et al. Electronic band structure of two-dimensional ws 2/graphene van der waals heterostructures. *Physical Review B*, 97(15):155421, 2018.

[128] Arieh Aviram and Mark A Ratner. Molecular rectifiers. *Chemical physics letters*, 29(2):277–283, 1974.

[129] NJ Tao. Probing potential-tuned resonant tunneling through redox molecules with scanning tunneling microscopy. *Physical Review Letters*, 76(21):4066, 1996.

[130] Yu Li, Chen Yang, and Xuefeng Guo. Single-molecule electrical detection: a promising route toward the fundamental limits of chemistry and life science. *Accounts of Chemical Research*, 53(1):159–169, 2019.

[131] Zhenpeng Hu, Bin Li, Aidi Zhao, Jinlong Yang, and JG Hou. Electronic and magnetic properties of metal phthalocyanines on au (111) surface: a first-principles study. *The Journal of Physical Chemistry C*, 112(35):13650–13655, 2008.

[132] Juan M Manriquez, Gordon T Yee, R Scott McLean, Arthur J Epstein, and Joel S Miller. A room-temperature molecular/organic-based magnet. *Science*, 252(5011):1415–1417, 1991.

[133] Joel S Miller and Arthur J Epstein. Organic and organometallic molecular magnetic materials—designer magnets. *Angewandte Chemie International Edition in English*, 33(4):385–415, 1994.

[134] Stephen J Blundell and Francis L Pratt. Organic and molecular magnets. *Journal of Physics: Condensed Matter*, 16(24):R771, 2004.

[135] Mark B Lundeberg and Joshua A Folk. Rippled graphene in an in-plane magnetic field: effects of a random vector potential. *Physical review letters*, 105(14):146804, 2010.

[136] FV Tikhonenko, DW Horsell, RV Gorbachev, and AK Savchenko. Weak localization in graphene flakes. *Physical review letters*, 100(5):056802, 2008.

[137] Naoto Ishikawa, Miki Sugita, Tadahiko Ishikawa, Shin-ya Koshihara, and Youkoh Kaizu. Lanthanide double-decker complexes functioning as magnets at the single-molecular level. *Journal of the American Chemical Society*, 125(29):8694–8695, 2003.

[138] Sheila MJ Aubin, Michael W Wemple, David M Adams, Hui-Lien Tsai, George Christou, and David N Hendrickson. Distorted mnivmniii3 cubane complexes as single-molecule magnets. *Journal of the American Chemical Society*, 118(33):7746–7754, 1996.

[139] Richard A Layfield. Organometallic single-molecule magnets. *Organometallics*, 33(5):1084–1099, 2014.

[140] W Wernsdorfer and R Sessoli. Quantum phase interference and parity effects in magnetic molecular clusters. *science*, 284(5411):133–135, 1999.

[141] George Christou, Dante Gatteschi, David N Hendrickson, and Roberta Sessoli. Single-molecule magnets. *Mrs Bulletin*, 25(11):66–71, 2000.

[142] ZH Xiong, Di Wu, Z Valy Vardeny, and Jing Shi. Giant magnetoresistance in organic spin-valves. *Nature*, 427(6977):821–824, 2004.

[143] Clément Barraud, Pierre Seneor, Richard Mattana, Stéphane Fusil, Karim Bouzehouane, Cyrile Deranlot, Patrizio Graziosi, Luis Hueso, Ilaria Bergenti, Valentin Dediu, et al. Unravelling the role of the interface for spin injection into organic semiconductors. *Nature Physics*, 6(8):615–620, 2010.

[144] Marc Ganzhorn, Svetlana Klyatskaya, Mario Ruben, and Wolfgang Wernsdorfer. Strong spin–phonon coupling between a single-molecule magnet and a carbon nanotube nanoelectromechanical system. *Nature nanotechnology*, 8(3):165–169, 2013.

[145] Dorsa Komijani, Alberto Ghirri, Claudio Bonizzoni, Svetlana Klyatskaya, Eufemio Moreno-Pineda, Mario Ruben, Alessandro Soncini, Marco Affronte, and Stephen Hill. Radical-lanthanide ferromagnetic interaction in a t b iii bis-phthalocyaninato complex. *Physical Review Materials*, 2(2):024405, 2018.

[146] Haibei Huang, Willem Van den Heuvel, and Alessandro Soncini. Lanthanide-radical magnetic coupling in [lnpc _2]⊖: Competing exchange mechanisms captured via ab initio multi-reference calculations. *arXiv preprint arXiv:2001.09420*, 2020.

[147] G Serrano, E Velez-Fort, I Cimatti, B Cortigiani, L Malavolti, D Betto, A Ouerghi, NB Brookes, M Mannini, and R Sessoli. Magnetic bistability of a tbpc 2 submonolayer on a graphene/sic (0001) conductive electrode. *Nanoscale*, 10(6):2715–2720, 2018.

[148] Sebastian Stepanow, Jan Honolka, Pietro Gambardella, Lucia Vitali, Nasiba Abdurakhmanova, Tzu-Chun Tseng, Stephan Rauschenbach, Steven L Tait, Violetta Sessi, Svetlana Klyatskaya, et al. Spin and orbital magnetic moment anisotropies of monodispersed bis (phthalocyaninato) terbium on a copper surface. *Journal of the American Chemical Society*, 132(34):11900–11901, 2010.

[149] Roberto Biagi, J Fernandez-Rodriguez, M Gonidec, A Mirone, V Corradini, Fabrizio Moro, Valentina De Renzi, Umberto Del Pennino, JC Cezar, DB Amabilino, et al. X-ray absorption and magnetic circular dichroism investigation of bis (phthalocyaninato) terbium single-molecule magnets deposited on graphite. *Physical Review B*, 82(22):224406, 2010.

[150] Ludovica Margheriti, Daniele Chiappe, Matteo Mannini, Pierre-E Car, Philippe Sainctavit, Marie-Anne Arrio, Francesco Buatier de Mongeot, Julio C Cezar, Federica M Piras, Agnese Magnani, et al. X-ray detected magnetic hysteresis of thermally evaporated terbium double-decker oriented films. *Advanced Materials*, 22(48):5488–5493, 2010.

[151] Matias Urdampilleta, Ngoc-Viet Nguyen, Jean-Pierre Cleuziou, Svetlana Klyatskaya, Mario Ruben, and Wolfgang Wernsdorfer. Molecular quantum spintronics: Supramolecular spin valves based on single-molecule magnets and carbon nanotubes. *International journal of molecular sciences*, 12(10):6656–6667, 2011.

[152] Linfeng Ai, Enze Zhang, Jinshan Yang, Xiaoyi Xie, Yunkun Yang, Zehao Jia, Yuda Zhang, Shanshan Liu, Zihan Li, Pengliang Leng, et al. Van der waals ferromagnetic josephson junctions. *Nature communications*, 12(1):1–9, 2021.

[153] I Petkovic, M Aprili, SE Barnes, F Beuneu, and S Maekawa. Coupled superconducting phase and ferromagnetic order parameter dynamics. *arXiv preprint arXiv:0904.1780*, 2009.